Cooling Strategies for PEM FC Stacks

Konzepte zur Kühlung von PEM-Brennstoffzellen

von

M. Sc. Syed Mushahid Hussain Hashmi

aus Karachi-Pakistan

Hamburg 2010

1. Gutachter: Professor Dr.-Ing. habil. Stephan Kabelac
   Helmut-Schmidt-Universität Hamburg
2. Gutachter: Professor Dr.-Ing. Bernd Niemeyer
   Helmut-Schmidt-Universität Hamburg

Tag der Promotion: 15.03.2010

_____

Acknowledgements

Syed Mushahid Hussain Hashmi,

Hamburg, March 2010

_____

Abstract

Fuel cell technology, even though not as advanced as predicted, is still one of the promising candidates for future efficient and sustainable energy conversion. Out of several types of fuel cells the proton exchange membrane fuel cell (PEMFC) is regarded as the future power source for transportation and portable electronic devices, because of its low operating temperature between 80-180ºC. PEMFC, like other types of fuel cells, converts the chemical energy of the hydrogen rich fuel into electrical energy, and as a by-product it generates water and heat. Part of this heat is a result of the thermodynamic reaction entropy, the bigger part is due to irreversible transport mechanisms. A removal of this low grade heat requires an efficient cooling system.

 This thesis provides a variety of cooling strategies for the efficient removal of heat, so that the temperature of the PEMFC stack remains under a tolerable limit and as much as possible spatially homogeneous. In first place it is important to know the magnitude and location of heat sources in PEMFC, then one can hunt for the cooling strategies. A systematic study of the heat sources in PEMFC is made in this thesis, and it is concluded that the irreversible sources of heat generation are amenable by using the toolbox of thermodynamics of irreversible processes. The reversible part of heat generation due to the entropy change taking place on behalf of the electrochemical reaction at the electrodes of the cell is uncertain. This brings a major limitation on the vast number of non-isothermal PEM fuel models developed in last two decades.

A complete computational modeling of the commercial size PEMFC stack is still far away from reality, this necessitates to decrease the complexity of the model which can allow us to simulate a large size stack. In this regard a sophisticated computational fluid dynamics (CFD) model of one single fuel cell is developed as a first step, which is capable of calculating the non-uniform heat flux distribution at the electrodes based upon the concentration changes occurring at the electrode due to the electrochemical reaction. Local current density distribution is predicted for two possible reactant flow arrangements in a stack. This single cell model gives rise to a simplified model for the stack simulation as a second step.

Larger PEMFC stacks are always cooled by liquid cooling. In this work different liquid cooling channel designs with single and multiple channels are analyzed numerically and the temperature distribution of the cooling plate is shown. The criterion for optimization of the design is made by calculating the total entropy generation. All different designs show stratification of temperature. Better uniformity of temperature can be achieved through off-setting and intelligent zoning of the temperature in the stack as proposed in the thesis. Two known benchmark problems are solved in this study to validate the calculation methods.

A four cell stack is modeled using CFD and the temperature distribution is experimentally validated by a four cell stack which is designed and manufactured in-house. An important result of this experimental work is the existence of temperature variation within a small active area of 25 cm^2. In the end a commercial size stack having 30 cells is simulated with cooling plates at a space of every cell, every third cell and every fifth cell. The resulting temperature distribution shows that the difference in maximum and minimum temperature of the stack decreases as the number of cooling plates increases. In a PEM-FC stack, just as in other types, the spatial temperature distribution is pivotal for its stability and for its lifetime expectation. The results of this thesis give important design criteria for an optimum thermal management of PEMFC.

_____

Zusammenfassung

Die Brennstoffzelle ist nach wie vor ein zukunftsträchtiger Baustein in einer effizienten und nachhaltigen Energiewandlungskette. Unter den verschiednen Brenstoffzellen-Varianten ist der Polymerelektrolyt-Membran Brennstoffzelle (PEM FC) der Kandidat für Fahrzeuge und mobile Anwendungen, da deren Betriebstemperaturen im Bereich 80°C – 180°C liegen. Wie alle Brennstoffzellen wandeln PEMFCs die innere chemische Energie eines wasserstoffreichen Brenngases in elektrische Energie um, wobei als Neben-bzw. Reaktionsprodukt Wärmeenergie und Wasser anfallen. Die anfallende Wärme ist zum einen der reversiblen thermodynamischen Reaktionsentropie zu zuordnen, zum anderen größeren Teil den irreversiblen Transportmechanismen in der Brennstoffzelle. Zur Abfuhr dieser Wärme ist eine effiziente Kühlstrategie erforderlich.

Diese Dissertation untersucht unterschiedliche Kühlstrategien zur effizienten Wärmeabfuhr einer PEM-Brennstoffzelle, um die innere Temperatur zuverlässig unterhalb zulässiger Grenztemperaturen und örtlich möglichst gleichverteilt zu halten. Hierzu werden zunächst die Größe und die Verteilung der Wärmequellen und Verlustmechanismen in der Brennstoffzelle dargestellt. Die Wärmeerzeugung durch die Transportmechanismen ist durch die Thermodynamik der irreversiblen Prozesse zugänglich. Ein bisher ungelöstes Problem ist aber die Zuordnung der Reaktionsentropie der elektrochemischen Reaktionen auf die Anode und die Kathode. Diese Unsicherheit limitiert die Belastbarkeit bisher bekannter Berechnungsmodelle zur Temperaturverteilung in PEM-Brennstoffzellen.

Eine detaillierte ganzheitliche dreidimensionale numerische Simulation einer PEMFC in kommerzieller Größe ist noch nicht möglich, so dass das Temperaturfeld in zwei Stufen berechnet werden muss. In der ersten Stufe wird eine einzelne Zelle in größtmöglicher dreidimensionaler Modellierung betrachtet und die hier auftretenden Wärmequellen und Temperaturfelder berechnet. Für die hierzu notwednige Kenntnis der lokalen Stromdichte werden zwei unterschiedliche Verteilung zugrunde gelegt. In einer zweiten Stufe wird aus diesem detailliertem Modell ein vereinfachtes Modell der Einzelzelle erstellt, welches die lokalen Wärmequellen richtig wieder gibt aber eine Simulation mit bis zu 100 Zellen erlaubt.

Gößere PEM-Brennstoffzellen sind in aller Regel flüssigkeitsgekühlt. In dieser Arbeit werden unterschiedliche Kanalgeometrien für die Führung der Kühlflüssigkeit untersucht und die daraus resultierenden Temperaturfelder mit einem Ansatz zum konjugiertem Wärmeübergang berechnet. Zur Optimierung der Kanalkonfiguration in Bezug auf Wärmeübertragung und minimalem Druckverlust wird die Entropieerzeugungsrate herangezogen. Die Temperaturverteilung kann, wie in der Arbeit gezeigt wird, durch eine optimierte Stromführung homogenisiert werden. Die numerischen Berechnungsmethoden werden anhand zweier literaturbekannter Benchmark-Probleme validiert. Zusätzlich werden die Berechnungsansätze mit experimentellen Daten aus einer aus vier Zellen bestehenden PEM-Laborbrennstoffzelle verglichen. Durch eine Vielzahl an Temperaturmessstellen kann schon bei der kleinen aktiven Elektrodenfläche von 25 cm^2 eine deutlich örtliche Temperaturverteilung nachgewiesen werden, wie sie auch in dem numerischen Modell dieser Zelle berechnet wird.

Insgesamt werden Berechnungen für PEMFC kommerzieller Größe mit Kühleinschüben nach jeder, nach drei und nach fünf Einzelzellen numerisch untersucht und diskutiert. Die Homogenität des Temperaturfeldes in der Brennstoffzelle muss gegen den zusätzlichen Aufwand von Kühleinschüben abgewogen werden, da diese Homogenität für die Belastbarkeit und Lebensdauer der Brennstoffzelle von großer Bedeutung ist. Hierzu stellt die Arbeit die notwendigen Auslegungs- und Optimierungskriterien bereit.

Table of Contents

_____

Nomenclature

Latin Letters

Symbol	Unit	Meaning
a	-	activity
A	m^2	area
A_r	J/mol	reaction affinity
C	mol/m^3	concentration
D	m^2/s	diffusivity
E	J	energy
E	V/m	electric field
E	V	the reversible cell potential
F	C/mol	Farady constant 96485 C/mol
G	J	Gibbs free energy
H	J	enthalpy
i	A/m^2	current density
J	$mol/m^2 s$	molar flux
J_q	W/m^2	flux of measurable heat
L_{ij}	-	phenomenological coefficient
M_i	kg/mol	molecular mass of species i
n	-	number of electrons transferred per mole of species
p	bar	partial pressure
p^0	bar	standard pressure
p_s	bar	saturation pressure
q	W/m^2	heat flux
Q	J	heat energy
$q*$	J	heat of transfer
R	J/mol K	universal gas constant 8.314 J/mol K
S	J/K	entropy
S_i	-	source term for species i
T	K	temperature
t	s	time
T^0	K	standard temperature

Symbol	Unit	Meaning
t_w	-	transport number of water
$\vec{v}$	m/s	Velocity vector (u,v,w)
V	m^3	volume
W	J	work
X	-	mole fraction
x,y,z	m	coordinates
Y	-	mass fraction

Greek Letters

Symbol	Unit	Meaning
$\varnothing$	V	electric potential
α	-	charge transfer coefficient
β	-	symmetry factor
ε	-	porosity
η	V	polarisation or overvoltage
κ	S/m	electrical conductivity
λ	W/mK	thermal conductivity
λ_w	-	water content
μ	J, J/mol	chemical potential
ν	-	stoichiometric coefficient
ξ_r	mol	extent of reaction
π	J	Peltier coefficient,
ρ	kg/m^3	density
σ	W/m^{3}K	entropy poroduction rate

Indices, mathematical symbols and abbreviations

Symbol	Meaning
$\otimes$	tensor product
Δ	change in a variable
a	anode
Be	Bejan number

c	cathode
eff	effective
g	gas
i	species i
IUT	index of uniform temperature
l	liquid
MEA	Membrane Electrode Assembly
Nu	Nusselt number
Pr	Prandtl number
Re	Reynolds number
RH	relative humidity
rxn	reaction
w	water
$\prod$	product
$\sum$	summation
∇	gradient operator

1   Introduction

1.1   Motivation

Energy and its transformation are essential to our lives and our well-being from an individual level to a nation level. In every human activity from breathing to transportation, energy is consumed or rather converted from one form to another as per the utility. Economic well-being of the nation is also correlated with the per capita energy consumption. Over 85% of our planet current energy needs are met through the consumption of fossil fuels. These fossil fuels are primarily consumed through combustion process, which is responsible for obnoxious emissions, these emissions are undoubtedly detrimental for our environment.

In reference [57] the depletion times for oil, coal and gas is estimated 35, 107, and 37 years respectively. The concerns about the environmental pollution and fossil fuel depletion demands new solutions for alternate energy sources. Fuel cell technology is one of the promising candidates for future energy conversion processes in wide application areas like portable power, transportation, and stationary power etc. There are several types and classifications of fuel cells depending upon the type of electrolyte, fuel and operating temperature. This thesis will focus on Proton Exchange Membrane (PEM) fuel cell only. A PEM fuel cell is by no doubt the most focused of the fuel cell type studied in last two decades by researchers all over the world.

A fuel cell is an electrochemical energy conversion device which directly converts the chemical energy of the fuel (hydrogen rich fuel) into electrical energy without an intermediate step of heat energy as common in internal combustion engines. At the point of use at least this conversion process is emission free. A by-product of this conversion process is water and heat. A PEM fuel cell produces heat in an amount comparable to its electric power P^{el} so that the efficiency is around 50% [58]. This means that if a fuel cell stack is capable of producing 100 W electrical power it will also generate heat with the same rate, i.e $\bar{Q}$ =100 W. In order to run the fuel cell stack steadily at a constant temperature it is required to dissipate the heat at the same rate by which the heat is being produced, so the cooling system is inevitable.

A critical issue in the cooling of PEM fuel cell stack is its low operating temperature (commonly reported 80ºC as the optimum temperature) in contrast with the conventional internal combustion engines [74]. The driving force for the heat transfer is the temperature difference, which is low in the PEM fuel cell case. This brings a challenge to the cooling system and the design of heat exchanger. In heat exchanging systems, when the temperature difference is low, one must increase the heat transfer surface area to maintain a required heat transfer rate. The efficacy of the heat exchanger is also depending upon the ambient temperature, this aggravates the burden on the cooling system of the PEM fuel cell especially in summer time. Another factor in a PEM fuel cell stack is that the exhaust streams do not contribute much in the removal of heat. The information for the generation of heat in PEM fuel cell is also not crystal clear especially the asymmetric distribution of heat sources across the membrane electrode assembly (MEA). All these factors demand a careful study to be made for the cooling of the PEM fuel cell stack.

_____

1.2   Literature review

1.2.1 Affect of temperature on the performance of PEM fuel cells.

Temperature is a critically important parameter for PEM fuel cell performance which directly/indirectly affects the reaction kinetics, transport of water, humidity level, conductivity of membrane, catalyst tolerance, removal of heat, thermal stresses in the membrane etc. A good review for the role of temperature in PEM fuel cells is made by Zhang et al. [56], which leads to the development of high temperature PEM fuel cells.

Song et al. [53] experimentally investigated the performance of Nafion® 112 membrane based fuel cell. They have concluded that the performance of the fuel cell increases as the temperature increases from room temperature to 80 ℃, further increase in temperature results in a current density dependent performance. That is, at a low current density (less than 0.4 A/cm^2) an increase in temperature leads to decrease in performance while at high current densities (greater than 0.4 A/cm^2) the temperature increase lead to an increase in performance. The best performance was observed at around 80 ℃, with 3 bar absolute back pressure and 100% relative humidity.

1.2.2 Heat sources in PEM-FC

In an excellent review of PEM-FC modeling by Wang [58] pointed out that in most of the modeling work the reversible heat released due to entropy change has often been overlooked. There is huge number of fuel cell modeling studies made in last two decades ranging from a simple empirical model to complex CFD models, the existence of several reviews in the literature [59][60][61] clearly indicates the scale of research underway all over the world for PEM fuel cells. In section 2.3 of this thesis it is explained that in literature there is no consensus about the magnitude and location of reversible heat generation at individual electrodes. Several non-isothermal fuel cell modeling studies in literature [62][63][64] have relied on Lampinen [5] results for entropy change which predicts that all the reversible heat is produced at the cathode. Wöhr et al. [8] used different values for the entropy change at anode and cathode, but the total entropy change for the overall reaction does not match with the entropy changes of the half-cell reactions, consequently their results produces an asymmetric heat generation at the electrodes. Recently Ramousse et al. [6] suggested that the hydrogen oxidation reaction is highly exothermic whereas the oxidation reduction reaction is endothermic.

1.2.3 Cooling channel design

Not much literature is available for the analysis of cooling channels for PEM fuel cells, in contrast with the studies related with heat and water transport in a fuel cell sandwich, which comprises a bunch of electrode, catalyst layer and membrane as depicted in Figure 2-1.

Chen et al. [44] investigated numerically different types of cooling modes from parallel channel design to serpentine channel design. They have used a criteria for the uniformity of temperature named IUT (index of uniform temperature) defined by equation (6.2) to optimize their designs. Their studies concluded that the serpentine-type cooling modes are better than that of parallel-type cooling modes on the expense of higher pressure drop. In their simulation they have used the uniform heat flux to model the heat generated by the fuel cell. At the inlet of the channel they have specified the mass flow rate as well as the inlet flow velocity! This is an over defined boundary condition. The outlet condition is not mentioned in the paper. For the surrounding surface of the cooling plate they have assumed an adiabatic boundary

_____

condition with a reasoning that the surrounding surface along the edge of the flat plate is small. For the heat transfer from the solid plate to the fluid the convective heat transfer coefficient is estimated from the correlation rather than it should be the outcome of the conjugate heat transfer results.

Choi et al. [49] analyzed numerically the performance of cooling plates in a PEM fuel cell similar to the work of Chen et al. [44] and studied both parallel and serpentine-type designs. They have used the maximum surface temperature as their criteria for optimization. They also used the uniform heat flux for heat generation, but they analyzed at three different values of heat flux for one, three, and five unit cells. From their result they concluded that the maximum surface temperature increases linearly as they increase the heat flux for their two particular designs at two different Reynolds numbers. This seems very natural under the adiabatic boundary condition at the surrounding walls, because there is no place available for heat to dissipate, consequently the temperature of the surface will rise when heat source increases for the steady state run.

Recently Yu et al. [50] examine the four multi-pass serpentine flow-field (MPSFF) design along with conventional serpentine and spiral design for cooling plates of PEM fuel cell. They have used the same criteria IUT for comparing the design as defined by Chen et al. [44]. Additionally they have compared the designs by the maximum surface temperature and the difference of maximum and minimum surface temperatures. For geometry they have used the symmetry to reduce the number of nodes in their simulation. So this will restrict them to use identical values of heat flux on both sides of the cooling plate. Three different values of uniform heat flux are employed in the simulation to cover the normal operating range of the PEM fuel cell. At the inlet of the channel velocity boundary condition is used. Their results suggest that the IUT decreases and pressure drop increases as the Reynolds number increases in all six designs. The so called MPSFF design is motivated from the study of Xu et al. [51] for fuel cell reactant flow field structures which is based upon re-patterning of single serpentine flow field in such a way that the pressure difference among the adjacent flow channels enhanced the in-plane forced flow through porous electrode like an interdigitated flow field.

1.2.4 Cooling methods for PEM FC

There are varieties of ways by which PEM fuel cell stack can be cooled depending upon the size and application of the stack. Shah [78] classified stacks below 100 W can be cooled by the reactant air, while in the range of 200 W to 2 kW stack can be cooled by separate air channels along with reactant streams. The stacks larger than 10 kW require liquid coolant. Faghri [81] briefly described the heat transfer issues related to PEM fuel cell stacks. Faghri [85] gives the possibility of integrating the heat pipe technology into fuel cell for improved thermal control. In one of his design, a micro-heat pipe is proposed to be embedded in the land area of the bipolar-plate. In reference [82], a theoretical study for the enhancement of cooling is made for the fuel cell electric vehicle. Figure 1-1 shows schematically the different cooling methods used for PEM fuel cell stacks in general. These commonly used cooling methods for PEM fuel cell stacks are explained briefly as follows:

Cooling with cathode air flow

For small size stacks cooling can be achieved only with cathode air flow. In such stacks usually the exposed (external) stack area is much larger than the active area (e.g air breathing PEM fuel cell stacks) so that the stacks are capable to dissipate heat at a rate comparable to the rate of heat generation. A disadvantage here is that it requires relatively bigger channel

_____

size for cathode side of the stack compared with the anode side, which consequently increases the volume of the stack.
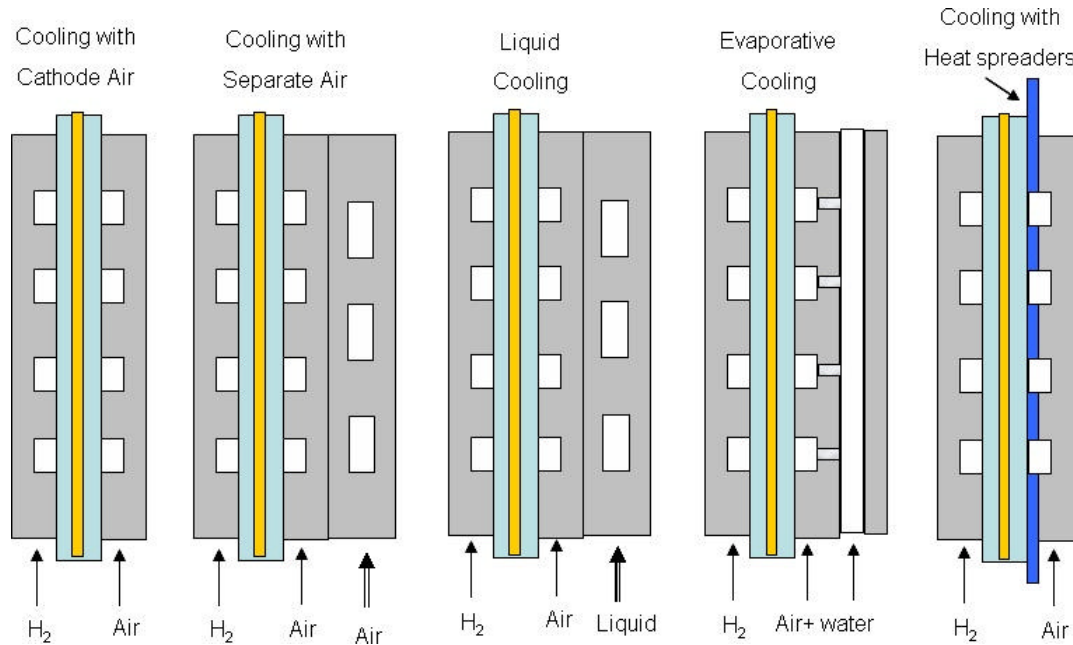
Figure 1-1 : Schematic of different cooling methods for unit PEM fuel cell

- **Cooling with separate air flow**

For stacks bigger than few hundreds watts require separate cooling channels in which air can be blown to carry out the heat generated by virtue of the exothermic reaction occur in the fuel cell.

- **Liquid cooling**

The thermal properties (specific heat capacity, thermal conductivity) of liquid are several orders higher than gas or air so for higher cooling load of the stack, liquid as a coolant is a natural choice instead of air. Liquid cooling via separate cooling channels is used in the PEM fuel cell stacks which are in the power range intended for automotive application.

- **Evaporative cooling (cooling with phase change)**

The enthalpy of vaporization of water is utilized in cooling by injecting additional water to the reactant streams of PEM fuel cell. The heat generated at the electrodes is taken by the water for its phase change while keeping the temperature constant. This method of cooling also helps in preventing the drying of the membrane. In reference [39] affect of operating parameters on water injection rate at the cathode side for evaporative stack cooling is investigated, and results are shown in Figure 1-2. At high load the requirement for injecting water increases to achieve the saturation conditions at the outlet, and to provide sufficient cooling. Several patents are available in the open literature regarding evaporative cooling for fuel cell general, some of the references for these patents can be found at [82].

_____
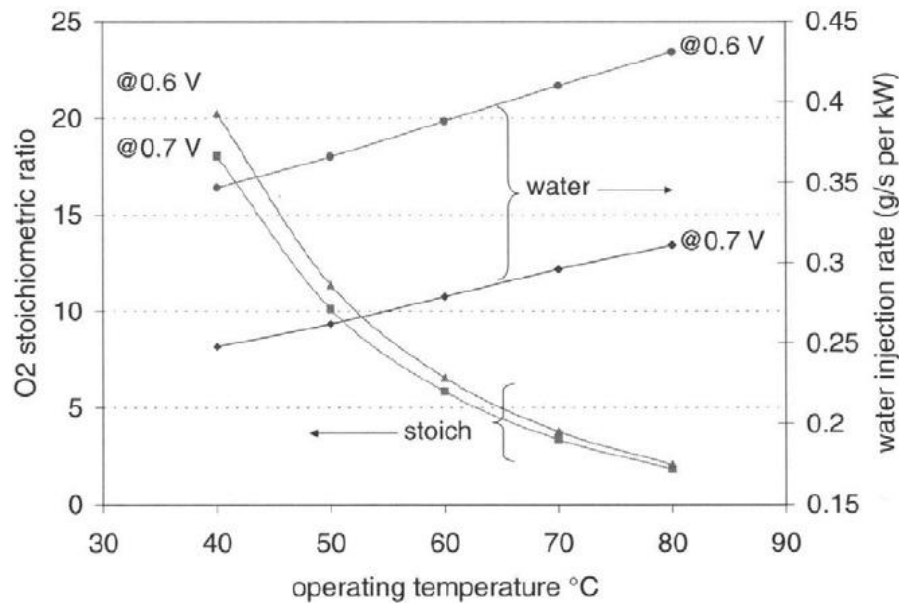
Figure 1-2 : Water injection rate required at different operating conditions for the evaporative cooling of the stack (Ref [39]).

- **Cooling with heat spreaders**

Heat spreaders are high conductivity materials employ adjacent to the flow channel plate as shown in Figure 1-3 for cooling purpose. In these so called heat spreaders first the transport of heat takes place through conduction then dissipates the heat to the surrounding air through natural or forced convection. Heat spreaders can act as a heat sink, part of the heat is carried through spreaders. In large size stacks use of spreaders can decrease the size of the cooling system.
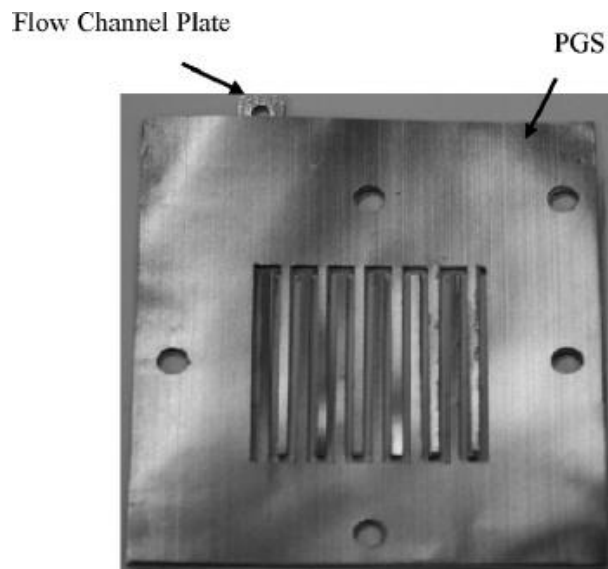
Figure 1-3 : Heat spreader made up of thermally conductive pyrolytic graphite sheet (PGS) aligned with the serpentine flow channel plate (Ref [79]).

Wen [79][80] demonstrated the use of thermally conductive pyrolytic graphite sheet (PGS) as heat spreader in a single cell and 10 cell stack experimentally. Their results showed that the maximum power of the 10 cell stack increased by 15 % after employing 5 PGS on the cathode side of the flow plate.

_____

2 Thermodynamics and Sources of heat in PEM FC stacks

PEM fuel cells are no exception in being energy conversion devices that also generate heat along with an electrical power like other power generation devices, but the nature of heat generation is a bit different from conventional devices. The polarization curve is a useful yardstick for PEM fuel cells in order to characterize the performance or efficiency as well as to compare different fuel cell designs. The heat generated in a PEM FC stack can be calculated from the polarization curve by comparing the real-time cell voltage to theoretical cell voltage at a given load, but the polarization curve does not provide any clue of heat or temperature distribution in the stack as a result of heat generation. This chapter will focus on where and how much heat is generated in PEM-FC stack. Sources of heat can be broadly classified into reversible and irreversible heat generation in PEM-FC stacks. In the end non-equilibrium thermodynamics principle is explained for the entropy generation in the membrane of the PEM fuel cell to show the coupled nature of the sources of irreversibilites.

2.1 Fuel cell principle

A fuel cell is an electrochemical device which converts the chemical energy of the fuel directly into electrical and heat energy. In contrast to a battery (also an electrochemical device) it does not consume stored chemical energy, but behaves like a continuous device which works as long as the fuel is supplied. There are several classifications of the fuel cell based upon the electrolyte, the fuel, the temperature and its applications etc. In the last two decades most of the research focused on PEM fuel cell largely because of its potential use in automotive applications. The schematic of a PEM fuel cell is shown in Figure 2-1.
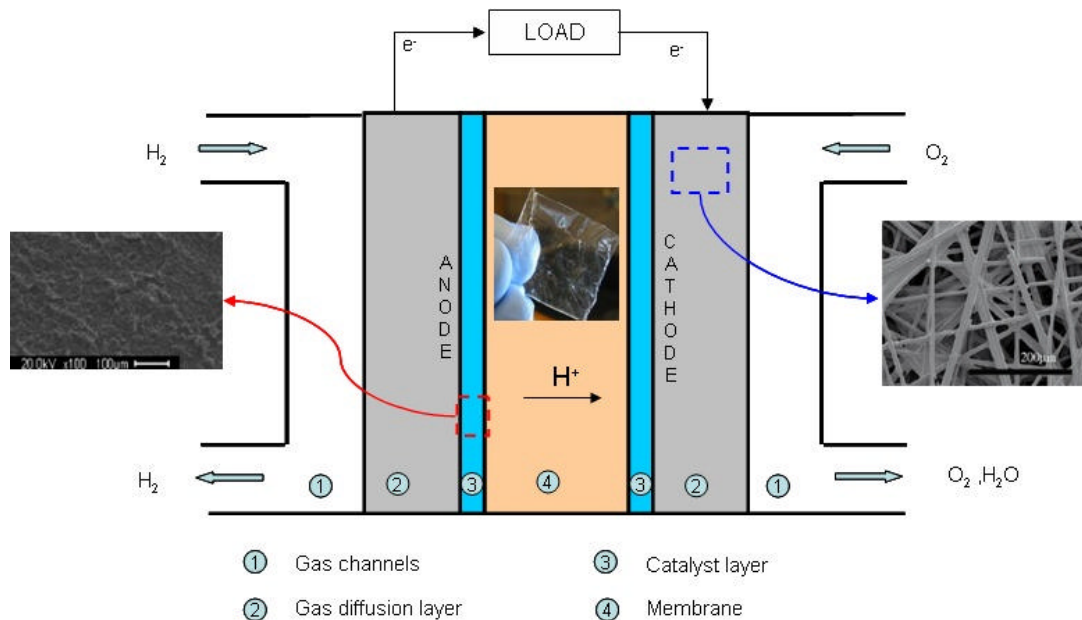
Figure 2-1 : Schematic of PEM fuel cell (not to scale)

Humidified fuel and oxidant are supplied in the gas channels, first these diffuse through gas diffusion layers and then reach the catalyst layers. At the interface of the membrane and the catalyst layer, the half-cell reaction takes place at both electrodes, one is named anode where oxidation is taking place, whereas reduction is taking place at the cathode. The half reactions at anode and cathode are shown in equation (2.1) and equation (2.2) respectively. At the

anode the hydrogen gas splits into protons and electrons, this specific membrane acting as an electrolyte only allows protons to pass through while the electrons go around the external circuit. At the cathode the electron and proton combines with oxygen to form water. The overall reaction is depicted in equation (2.3). This is the way by which we will be able to harness the chemical energy of hydrogen directly into electrical energy; we call this process to be the cold combustion of hydrogen, because this process can take place even at room temperatures. In contrast to this the direct combustion of hydrogen requires very high values of activation energy, as no catalyst is present there. This means very much higher temperatures, thus we will call this later process to be the hot combustion of hydrogen.

$$\text{anode reaction} \qquad\qquad H_{2(g)} \rightarrow 2H^+ + 2e^- \qquad\qquad (2.1)$$

$$\text{cathode reaction} \qquad\qquad \frac{1}{2}O_{2(g)} + 2H^+ + 2e^- \rightarrow H_2O_{(l)} \qquad\qquad (2.2)$$

$$\text{overall reaction} \qquad\qquad H_{2(g)} + \frac{1}{2}O_{2(g)} \rightarrow H_2O_{(l)} \qquad\qquad (2.3)$$
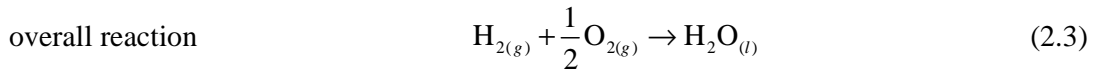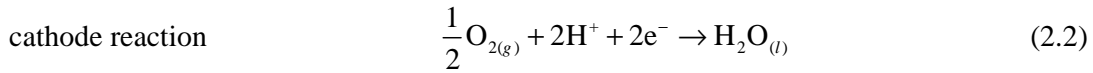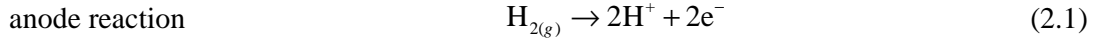
2.2 Heat released by reaction

Consider the direct combustion of hydrogen in a combustion chamber as shown in Figure 2-2, where a homogeneous redox reaction is taking place as by equation (2.4), assuming that the product water is in a gaseous state.
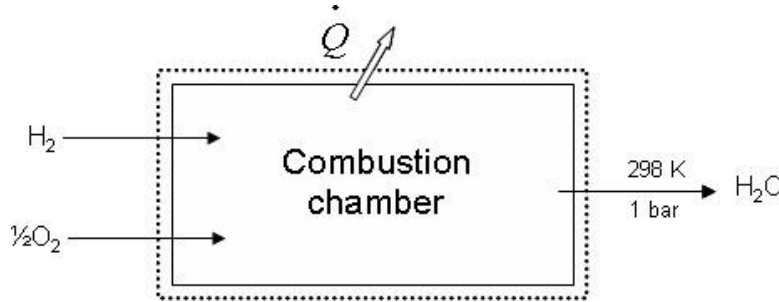
Figure 2-2 : Direct combustion of hydrogen

In order to get the quantity of heat released in this reaction, we calculate this heat released from mean bond enthalpies.

$$H_{2(g)} + \frac{1}{2}O_{2(g)} \rightarrow H_2O_{(g)} \qquad\qquad (2.4)$$

First consider the reactant side; the molecular reactants hydrogen and oxygen need to split first into single atoms, then the two hydrogen atoms will combined with one oxygen atom to form one water molecule, this split is shown in equation (2.5).

_____

$$H\text{-}H + \frac{1}{2}(O\text{-}O) \rightarrow H\text{-}O\text{-}H \tag{2.5}$$
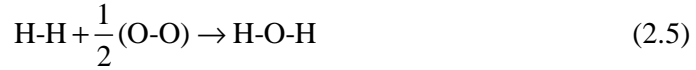
Now the reaction enthalpy is calculated from the fact that energy is required to break the bond, while energy is released when bonds are formed. Here H-H and O-O bonds are breaking and H-O bonds are formed, so the reaction enthalpy is calculated as follows:

$\Delta H_{rxn} = \Delta H$ (H-H) + ½ ΔH (O-O) – 2 ΔH (H-O)

$\Delta H_{rxn} = 436 + ½ (497) -2 (463) = -241.5$ kJ/mol

The values of the average bond enthalpies have been taken at 298K from reference [1], care should be taken for these mean bond enthalpies not to be confused with bond dissociation energies, which may differ considerably for example in a H-O bond, this bond dissociation energy is 429.9 kJ/mol as in reference [2].

This shows that for one mole of water formed in gaseous state 241.5 kJ of energy is released, this number is of course in good agreement with the value (-241.8 kJ/mol) reported for standard enthalpy of reaction for the formation of $H_2O_{(g)}$ in several literatures of thermo-chemical data [3][4].

$$H_{2(g)} + \frac{1}{2}O_{2(g)} \xrightarrow[\text{1 bar}]{\text{298 K}} H_2O_{(g)} + 241.5 \ \text{kJ} \tag{2.6}$$

So the equation for combustion of hydrogen can be precisely written as equation (2.6), the validity of this equation is subject to the standard conditions and the assumption that both reactants and products are in gaseous state as well as there is a complete combustion of 1 mole of hydrogen. In combustion literature the number -241.8 kJ/mol (the enthalpy of hydrogen combustion reaction) is known as the lowe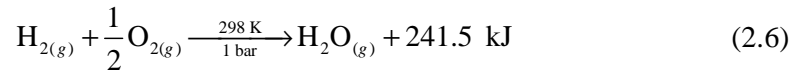r heating value (LHV) of hydrogen. When the combustion product is in liquid form the enthalpy of hydrogen combustion reaction is known as the higher heating value (HHV). The higher heating value of hydrogen is -285.8 kJ/mol at standard condition as reported in reference [4]. The difference between the HHV and LHV is the enthalpy of evaporation of water $\Delta h_{v,H_2O}$ at standard condition, which is $\Delta h_{v,H_2O} = 44$ kJ/mol.

2.3   Heat and work released – Fuel cell

The chemical energy that we have available in a fuel cannot be converted all into useful work (electrical energy) because of the entropy change occurring during a chemical reaction. Entropy can only be balanced by heat or by entropy production. The useful work can be described by the Gibbs free energy as in equation (2.7).

$$\Delta G = \Delta H - T\Delta S \tag{2.7}$$

The Gibbs free energy equation is an outcome of the first and second law of thermodynamics. Consider a fuel cell as an open thermodynamic system as shown in Figure 2-3, where heterogeneous redox reaction is taking place.

_____
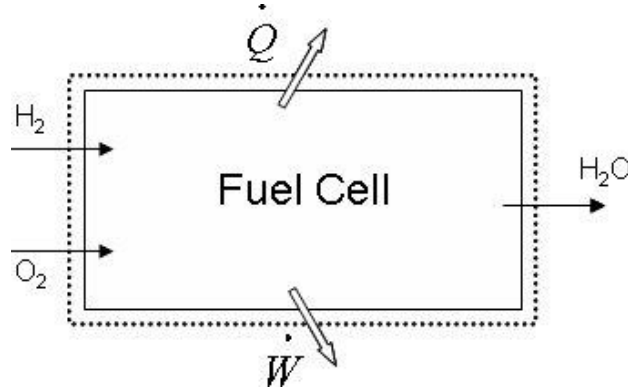
Figure 2-3 : Fuel cell as an open system

Applying the first law of thermodynamics, a balance equation for the energy E gives:

$$\dot{E}_{in} - \dot{E}_{out} = \frac{\partial E}{\partial t}$$

(2.8)

When the fuel cell is operating at a steady state, the rate of energy accumulation is zero, we have

$$\dot{E}_{in} - \dot{E}_{out} = 0$$
$$\dot{Q} - \dot{W} + \sum_{in} \dot{n}_{in} \bar{h}_{in} - \sum_{out} \dot{n}_{out} \bar{h}_{out} = 0$$

(2.9)

where $\dot{n}$ is the molar flow rate in [mol/s] and $\bar{h}$ is the molar enthalpy in [J/mol], $\dot{Q}$ and $\dot{W}$ are the rate of heat and work interactions respectively. If we denote H_{in} as enthalpy in and H_{out} as enthalpy out we can write equation (2.9) as

$$\dot{Q} - \dot{W} + H_{in} - H_{out} = 0 \quad \text{or} \quad \dot{Q} - \dot{W} - \Delta H = 0$$

(2.10)

Now the second law of thermodynamics, the balance equation for the entropy S, is applied to the fuel cell system

$$\frac{\dot{Q}}{T} + \sum_{in} \dot{n}_{in} \bar{s}_{in} - \sum_{out} \dot{n}_{out} \bar{s}_{out} + \dot{S}_{irr} = \frac{\partial S}{\partial t}$$

(2.11)

where $\bar{s}$ is the molar entropy and $\dot{S}_{irr}$ is the entropy generation because of the irreversibilities. For a reversible ($\dot{S}_{irr} = 0$) and steady state ($\frac{\partial S}{\partial t} = 0$) system we can write equation (2.11) as

$$\frac{\dot{Q}}{T} + \sum_{in} \dot{n}_{in}\overline{s}_{in} - \sum_{out} \dot{n}_{out}\overline{s}_{out} = 0 \tag{2.12}$$

If we denote S_{in} and S_{out} as the incoming and outgoing entropy streams we can write equation (2.12) as

$$\frac{\dot{Q}}{T} + S_{in} - S_{out} = 0 \quad \text{or} \quad \frac{\dot{Q}}{T} - \Delta S = 0 \tag{2.13}$$

By combining the equation (2.10) from the first law and equation (2.13) from the second law we get

$$\dot{W} = -(\Delta H - T\Delta S) \tag{2.14}$$

By definition the maximum work available through a reversible process is represented as negative change in Gibbs free energy,

$$\dot{W} = -\Delta G \tag{2.15}$$

By comparing equation (2.14) and equation (2.15) we get

$$\Delta G = \Delta H - T\Delta S \tag{2.16}$$

In the above analysis a convention used for energy interaction is that the heat coming into the system is taken positive, while the work coming into the system is taken negative. And change is taken from 'out' minus 'in' e.g $\Delta H = H_{out} - H_{in}$.

For reaction in equation (2.3), where product water is liquid, we can calculate the Gibbs free energy at standard conditions using the values given in Table 2-1. First the entropy change calculation is as follows:

$\Delta S = s_f(H_2O) - s_f(H_2) - ½ s_f(O_2)$
$\Delta S = 0.06995 - 0.13068 - ½ (0.20515) = -0.16331$ kJ/mol K

Now the Gibbs free energy is calculated using equation (2.7) as follows:

$\Delta G = -285.8 - 298 (-0.16331) = -237.1$ kJ/mol

This shows that 237.1 kJ/mol is the energy that can be converted into electrical energy at maximum, it means 48.6 kJ/mol is the energy which is inevitably converted into heat even when the fuel cell is working reversibly, when no current is drawn, in the so called open circuit condition. This calculation shows the magnitude of reversible heat generation for an

_____

overall reaction, it does not give any information how much is the contribution of heat generation at each individual electrode where the half-cell reactions are taking place.

Table 2-1: Enthalpies and Entropies of formation at standard condition for PEM fuel reactants and product, Reference [4].

	h_f (kJ/mol)	s_f (kJ/mol K)
H_2	0	0.13068
O_2	0	0.20515
H_2O (*l)*	-285.8	0.06995
H_2O (g*)*	-241.8	0.18896

The knowledge of heat generation at each individual electrode is crucial for the designers who are interested in the temperature distribution and gradients in the cell, the temperature is an important design variable in fuel cell engineering for many reasons like improved kinetics, membrane stability, water and thermal management, and cooling strategies etc. There is no doubt about the fact that PEM fuel cell generate heat or that the overall reaction is exothermic, but we don't know exactly how much heat is generated or absorbed at each electrode. This can be answered by investigating the entropy changes happening in the half-cell reactions of equation (2.1) and (2.2), the literature available in this regard shows no unique values for entropy changes occurring in half-cell reactions, a wide spread difference is evident in Table 2-2.

Table 2-2 : Entropy changes of half-cell reactions at anode and cathode

ΔS_a (J/mol K)	ΔS_c (J/mol K)	ΔS_{total} (J/mol K)	Reference
anode	cathode	overall	
+0.104	-163.2	-163.1	[5]
-133.2	-30.1	-163.3	[7]
-130.7	-65.0	-195.7	[8]
-226.3	+62.8	-163.5	[6]

Attention is required in quoting and comparing the numerical values for entropy changes given in the literature. First the stoichiometry and the phase description of the half-cell reactions have to be noted, second the temperature and pressure conditions of the reaction have to be given, and third is the unit involved (whether per mole or per kg basis).

The heat absorbed or released for a reversible reaction can be calculated from equation (2.17).

$$Q_{rel/abs} = T\Delta S \qquad (2.17)$$

In equation (2.17) the sign of entropy change decides whether the heat is released or absorbed, where T is the absolute temperature at which the entropy change is taking place. Negative values indicate heat being released, an exothermic reaction, while positive values indicate that heat is absorbed during the reaction. By closely looking at Table 2-2 it is difficult to decide

_____

whether the anodic reaction is slightly endothermic or highly exothermic. This difficulty barred us in defining exactly the magnitude and distribution of heat sources and/or sinks at individual electrodes of PEM fuel cell, consequently the prediction of temperature across the cell is not meaningful. The discrepancy is due to the difficulties involved in the calculation of entropy change occurring in half-cell reactions, which involves ionic species. One reason quoted in reference [6] is "actually it is impossible to make a solution of cations without anions, so that entropy of ions is not easy to estimate". Another reason is that the different scales of entropy have been used e.g. in reference [5] a semi-absolute entropy scale is introduced.

This reversible heat generation is a significant contributor in total heat generation of the PEM fuel cell, according to reference [9] about 35% of the total heat generation is due to entropic heat of reaction, so by no way it can be neglected in thermal modeling of the PEM fuel cells.

2.4   Reversible cell potential- Nernst potential

Consider an arbitrary chemical reaction with species A, B on the reactant side and C, D on the product side.

$$\nu_A A + \nu_B B \rightleftharpoons \nu_C C + \nu_D D \qquad (2.18)$$

here ν_i is the stoichiometric coefficient for species i. According to fundamental Gibbs equation the differential for Gibbs free energy can be written as [76] :

$$dG = -SdT + Vdp + \sum_i \mu_i dn_i \quad , \qquad (2.19)$$

here μ_i is the chemical potential of species i and n_i is the number of moles of species i. Using the relation $dn_i = \nu_i d\xi$, the fundamental Gibbs equation can be written as

$$dG = -SdT + Vdp + \sum_i \nu_i \mu_i d\xi \quad , \qquad (2.20)$$

here $d\xi$ is the differential extent of reaction. At constant temperature and pressure the above equation can be written as:

$$\left(\frac{dG}{d\xi} \right)_{T,p} = \sum_i \nu_i \mu_i \quad . \qquad (2.21)$$

Now the change in Gibbs free energy is

$$\Delta G = \sum_{product} \nu_i \mu_i - \sum_{reactant} \nu_i \mu_i$$
$$= (\nu_C \mu_C + \nu_D \mu_D) - (\nu_A \mu_A + \nu_B \mu_B) \qquad (2.22)$$

_____

The chemical potential is related to concentration through activity [67] as follows:

$$\mu_i = \mu_i^0 + RT \ln a_i \ ,$$

(2.23)

where μ_i^0 is the reference chemical potential of species i at standard state conditions (T^0=298 K, p^0=1 bar) and a_i is the activity of species i. The activity of species depends on its chemical nature. For an ideal gas $a_i = p_i / p^0$, were p_i is the partial pressure of the gas and p^0 is the standard state pressure [67].

By substituting equation (2.23) in change in Gibbs free energy equation (2.22), and after simplification we get

$$\Delta G = \Delta G^\circ + RT \ln \frac{a_C^{v_C} a_D^{v_D}}{a_A^{v_A} a_B^{v_B}}$$

(2.24)

here ΔG° is the Gibbs free energy change at the standard state. Equation (2.24) is known as Van't Hoff isotherm. This equation tells us how the Gibbs free energy changes when the activities of species changes. The reversible cell voltage E of the cell is related to the Gibbs free energy by

$$\Delta G = -nFE$$

(2.25)

here n is the number of moles of electrons transferred in the cell reaction, F is Faradays constant (F=96485 C/mol), In the same way at standard condition the reversible cell voltage E^o is related with standard Gibbs free energy by

$$\Delta G^\circ = -nFE^\circ$$

(2.26)

By substituting equation (2.25) and (2.26) in (2.24) we get the important Nernst equation

$$E = E^\circ - \frac{RT}{nF} \ln \frac{a_C^{v_C} a_D^{v_D}}{a_A^{v_A} a_B^{v_B}} \ .$$

(2.27)

For an arbitrary number of reactants and products the Nernst equation can be written in a general form as follows:

$$E = E^\circ - \frac{RT}{nF} \ln \frac{\prod_i a_{i(products)}^{v_i}}{\prod_i a_{i(reactants)}^{v_i}}$$

(2.28)

For the H_2-O_2 fuel cell where one mole of hydrogen combines with half mole of oxygen to form one mole of water and where two electrons are transferred per mole of H_2 as shown in equation (2.3), the reversible voltage using the Nernst equation can be written as

$$E = E° - \frac{RT}{2F} \ln \frac{a_{H_2O}}{a_{H_2} a_{O_2}^{1/2}} \qquad (2.29)$$

So the above Nernst equation can predict the effect of changes in concentration, temperature or pressure of the reactants and products on a reversible voltage. The effect of pressure on the reversible voltage for a PEM fuel cell under practical operating conditions is typically not more than few milivolts [14].

In the Nernst equation (2.28) there is a presence of temperature T, but it does not fully account how the reversible voltage varies with temperature. Using equation (2.26) and (2.7) at standard state condition, the reversible voltage can be written as

$$E° = -\frac{\Delta H°}{nF} + T \frac{\Delta S°}{nF} \qquad (2.30)$$

Now when differentiating equation (2.30) with respect to temperature T at constant pressure, we get

$$\frac{dE°}{dT} = \frac{\Delta S°}{nF} \qquad (2.31)$$

It is assumed here that the molar heat capacity and entropy change is independent of temperature, which is quite a reasonable assumption for the temperature range of PEM fuel cell operation [39]. Now using equation (2.31) the reversible voltage can be written as a linear function of temperature

$$E°(T) = E° + \frac{\Delta S°}{nF}(T - T^0) \quad . \qquad (2.32)$$

Here T^0 is the standard temperature. So a complete expression for the reversible voltage can be written as

$$E = E° + \frac{\Delta S°}{nF}(T - T^0) - \frac{RT}{nF} \ln \frac{\prod_i a_{i(products)}^{v_i}}{\prod_i a_{i(reactants)}^{v_i}} \quad . \qquad (2.33)$$

2.5   Irreversible heat generation

Irreversible heat generation is evidence of the destruction of available energy for the sake of electric current drawn from the cell as well because of the irreversibilities inherent in the PEM fuel cell system like fuel cross over, poisoning of the catalyst etc. Unlike entropic reversible heat generation the irreversible heat generation is very much amenable thanks to the characterization techniques available. These techniques have shown that the activation polarization at the cathode is far more severe than at the anode reaction site. For an operating

_____

PEM fuel cell irreversible heat generation can be quantified by combining the polarization or voltage drop due to activation at the anode and cathode as well as because of the resistance of the membrane, which is dominantly the ionic resistance. We have not deliberately included the polarization due to mass transport limitation, because we do not operate PEM fuel cell in this region of the polarization curve. A simplified approach is given in equation (2.34), where η_a, η_c represent activation polarization at anode and cathode respectively, R is the membrane resistance and i is the electric current drawn from the cell.

$$Q_{irr} = \eta_a i + \eta_c i + i^2 R \tag{2.34}$$

A simplified visual description of reversible and irreversible heat generation is shown in Figure 2-4.
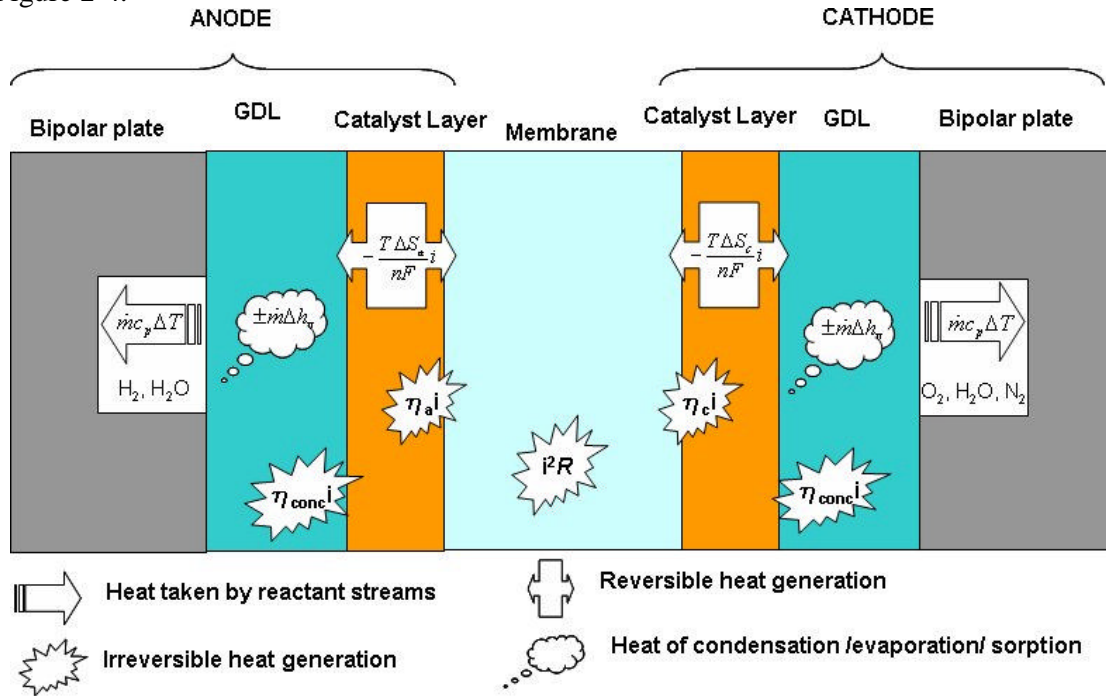

Figure 2-4 : Schematic of heat sources and sinks in a PEM fuel cell sandwich

An overall performance of a PEM fuel is commonly shown by V-i curve known as the polarization curve. A typical voltage-current relationship scaled with the geometric electrode area for H_2-O_2 PEM fuel cell is depicted in Figure 2-5. In this figure the zones labeled I, II, III are the activation, ohmic, and mass transfer dominated regions respectively. It is important to understand that these three regions are not discrete, when current is drawn from the cell voltage decreases. At a given current there is a corresponding voltage, if the cell is operating at a particular current the resulting voltage includes all three polarizations (activation, ohmic and mass transport), but if a cell is operating at low current density it is realized that in this over-voltage the activation over-voltage is dominant compared with ohmic and mass transport contribution. The same is true if the current drawn from the cell is high, one can say that in resulting over-voltage, the contribution of mass transport is dominant compared with activation and ohmic share. All modes of over-voltages contribute throughout the entire operating current range. The zone IV represents a departure of actual voltage from the Nernst potential. This voltage loss is quite a significant loss by virtue of the undesired species cross-over through electrolyte and due to the internal currents from electron leakage through

_____

electrolyte. The zone V signifies a loss of voltage as a result of entropy change during an electrochemical reaction. The following sub sections describe these over-voltages separately.
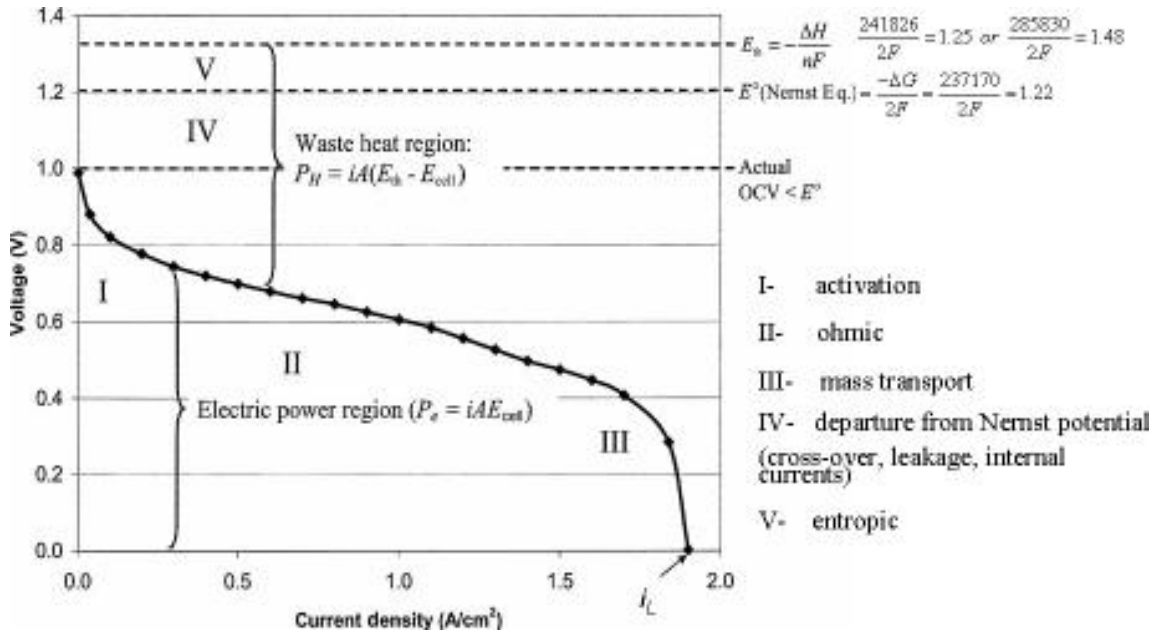

Figure 2-5 : A typical polarization curve adopted from reference [14].

2.5.1 Activation polarization

Activation polarization is the voltage loss or over-potential required to overcome the activation energy barrier of the rate determining step of the electrochemical reaction on the catalytic surface. It can be imagined as a sacrifice of the available voltage to initiate the electrochemical reaction roughly analogous to the ignition energy input for gasoline combustion. Electrochemical reaction rates are finite even though thermodynamically favorable (energetically downhill) because of activation barrier $\Delta G^{\ddagger}$, which impedes the conversion of reactants into products. It is pictorially shown in Figure 2-6.
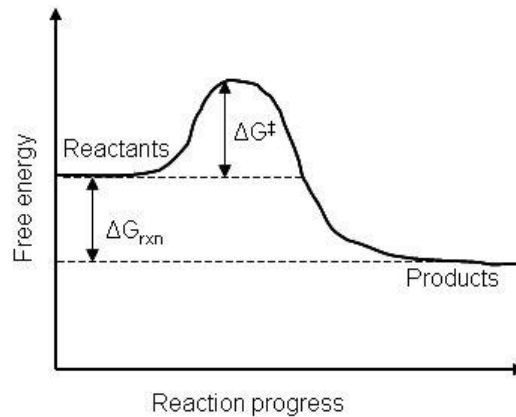

Figure 2-6 : Activation barrier ($\Delta G^{\ddagger}$) impedes the conversion of reactants to products (image adopted from reference [67])

As already said in section 2.1 of this thesis, a fuel cell is an electrochemical energy converter. Electrochemical reactions are occurring simultaneously at the electrode/electrolyte interfaces.

_____

For H_2-O_2 fuel the half-cell reactions occurring at the electrodes are given in equation (2.1) and (2.2). Actually these half-cell reactions are not one-way reactions but two-way (reversible) reactions. In general these half-cell oxidation-reduction reactions can be shown as in equation (2.35).

$$Ox + ne^- \underset{k_b}{\overset{k_f}{\rightleftharpoons}} Re \tag{2.35}$$

where Ox stands for oxidized species and Re for reduced species. For a H_2-O_2 fuel cell, hydrogen loses an electron (it is oxidized) while oxygen gains an electron (it is reduced). At equilibrium there is no net oxidation at the anode and no net reduction at the cathode so there is zero net current. In literature this equilibrium condition is known as open-circuit condition and the resulting voltage is called open-circuit voltage E_0. At open-circuit condition, no net current is flowing through the electrodes, but it does not mean that there is no electrochemical activity going on at the electrodes, both oxidation and reduction are underway with equal rates. That is why fuel cell manufacturers do not recommend operating the fuel cell at open-circuit condition for a long duration. Electrochemical reactions involve both the transfer of electrical charge and a change in Gibbs free energy, so the kinetics or the rate of electrochemical reaction depends upon the speed at which the electrons are released or consumed.

The activation polarization is commonly described by the Butler-Volmer equation [39] as follows:

$$i = i_0 \left(e^{\frac{\beta nF}{RT}\eta} - e^{\frac{-(1-\beta)nF}{RT}\eta} \right), \quad \text{where} \quad i_0 = i_{0ref} a_c L_c \left(\frac{p}{p_{ref}} \right)^\gamma e^{\left[\frac{E_c}{RT}\left(1 - \frac{T}{T_{ref}} \right) \right]} \tag{2.36}$$

All the parameters involved in the above equation are explained in the section 3.3 of this thesis. This Butler-Volmer formulation assumes that the electrochemical reaction rate is limited by a charge transfer process through an activation barrier of rate determining step. For small activation potentials (fast kinetics) the Butler-Volmer equation is linearized as follows:

$$\eta_{act} = \frac{RT}{nF} \frac{i}{i_0} \tag{2.37}$$

For high polarization (slow kinetics)

$$\eta_{act} = \frac{RT}{\alpha F} \ln \left(\frac{i}{i_0} \right), \tag{2.38}$$

where α is the charge transfer coefficient and i_0 is the exchange current density. There are several factors which can influenced the activation polarization like the reaction mechanism, catalyst type, loading and its morphology, operating parameters, species concentrations, impurities and poisoning elements etc. Interested readers may consult several good texts [14] [17][18][39][67] which are available for details.

2.5.2 Mass transport or concentration polarization

This loss of voltage or polarization which is called mass transport or concentration polarization is because of the reduction of the reactants surface concentration at electrode/electrolyte interface. This situation arises when the rate of transport of reactants towards the electrodes goes below the stoichiometric rate at a given operating condition, basically the fuel cell is starving of reactants, and consequently there is a sharp decline in performance as shown in Figure 2-5. This usually happens at high current densities. The multitude of reasons quoted for this reactant transport limitation is as follows:

1. Gas diffusion limitations- As the reactants flow in the gas channel the flow is dominated by convection, but within the gas diffusion layer the flow is dominated by diffusion. The rate of diffusion is finite and affected by the porosity, permeability, tortuosity of the porous media and the operating conditions. The effective path length for diffusing gasses can be far stretched from the physical thickness of the gas diffusion layer. Figure 2-7 shows one of the possible diffusion paths from the gas channel to the reaction site [14].

2. Liquid-phase accumulation- PEM fuel cell commonly operate below 100ºC, so the liquid water accumulates in gas channels and blocks the pores of the diffusion matrix media. The presence of water at the cathode side of the fuel cell is obviously due to the overall reaction, but water can also be present from the condensation of the humidified reactant streams as well. A voltage dropped by this liquid-phase accumulation is commonly termed as flooding. In reference [68] flooding on the cathode side is visualized through a transparent cell, and a voltage drop of 80 mV under low stoichiometry and two to five-fold increase in pressure drop is observed as a result of flooding. This pressure drop is a significant burden on parasitic power loss. A good review on liquid water visualization is found in reference [69].

3. Build-up of inert gases- Air is normally used as the oxygen supply in PEM fuel cells which contains nitrogen as an inert non-reacting specie. As the reaction progresses the oxygen concentration diminishes and the nitrogen mass fraction increases within the diffusion layer, so there is a build-up of nitrogen which may affect the transport of reactant mass.
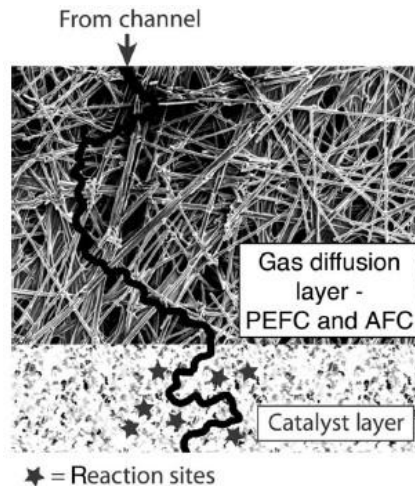

Figure 2-7 : Schematic of one of the possible diffusion path (Ref [14])

The rapid consumption of reactants due to the electrochemical reaction is responsible for the gradient of concentration developed between the bulk reactant concentration of reactants and the surface reactant concentration at the catalyst layer. The concentration polarization is

_____

quantified using the fact that the effect of concentration changes is present in both Nernst and Butler-Volmer equations. By combining these two loss effects and using Fick's law of diffusion results in an expression for concentration polarization [67], which is as follows:

$$\eta_{conc} = \frac{RT}{nF}\left(1+\frac{1}{\alpha}\right)\ln\left(\frac{i_L}{i_L-i}\right) \quad . \tag{2.39}$$

Here i_L is the limiting current density. In Figure 2-5 the limiting current density is shown. It is the maximum limit of electric current, a fuel cell cannot produce more electric current than this because there are no reactants available at the catalyst surface anymore. The operating current density of the fuel cell should always be reasonably below this limiting value.

2.5.3 Ohmic polarization

Ohmic polarization is due to the resistances offered by the fuel cell components (electrolyte membrane, bipolar-plate, electrodes, interconnects) against the mobility of the charged species (ions and electrons). On a polarization curve, if one disregards the other polarization effects, one can estimate the overall resistance from the slope of the linear part of the V-i curve. Ionic conductivity is several orders-of-magnitude lower than the electronic conductivity as it is evident from the Table 2-3. The difference of conductivity of electron and ion is depending upon the size of the charged species as well as the mechanism and the medium of the mobility involved. The movement of ions in a hydrated PEMFC membrane is thought to be achieved through the so called Grotthuss mechanism (protons hop from one H_3O^+ to another along a connected pathway in the ionomer structure) while the electro-osmotic flow is described by the Vehicle mechanism [70]. Ohm's law is used for ohmic conductors where there is a linear relationship between voltage and current. This linear relationship does work well for good electrical conductors such as metals but this can be an issue for solid polymers, as we know that this linearity does not exist in semi-conductors [72]. So there is no question about the validity of Ohm's law for free-electron flow in the conductors, but a non-linear behavior may exist for ionic flow in the hydrated polymer membrane whose conductivity has already been correlated non-linearly with the water content. To the authors knowledge there is no literature available for the validity or invalidity of Ohm's law for ionic flows in the polymer membrane. One point is important to mention here as described by Mench [14] that the presence of a strong electric field across the so called electric double layer at the interface of electrode and electrolyte. To get the feeling of the magnitude of this electric field, assume a typical activation over-voltage of 0.2 V across the double layer of thickness 10 nm. The electric field strength (E=V/d) is 2×10^8 V/cm. How does the transport of charges take place under such a strong electric field? The coupling effect of water and electrical conductivity in the PEM fuel cell membrane is explained through non-equilibrium thermodynamics in section 2.8.4 of this dissertation.

Table 2-3 : Typical conductivities for PEMFC components (Ref [14])

	Conductivity (S/m)
Electrolyte (hydrated)	10
Bipolar-plate (graphite)	5000 - 20,000
GDL (through plane)	10,000
Catalyst layer	1 - 5

_____

Another important issue related with the Ohmic polarization is on the contact resistance between any two mating parts (bipolar-plate and GDL, GDL and catalyst layer, catalyst layer and membrane) of the PEM fuel cell sandwich. This contact resistance can seriously hamper the performance of fuel cell as noted by the author himself during experiments with the single cell and four cell stack described in section 6.2.2 of this thesis. From the laboratory level experience a minute less compression of the tightening bolt of the cell results in a sharp drop in voltage even at small current loads. This decline of voltage is not observed at the open circuit condition, it is only observed when current is drawn from the cell. Factors which contribute in contact resistance include compression pressure, surface oxidation, manufacturing tolerance level for flatness and land to gas channel ratio.

Nitta et al. [71] has measured the contact resistance between the gas diffusion layer (GDL) and catalyst layer (CL) of the PEM fuel cell under compression pressure, their interesting results are shown in Figure 2-8. According to their results the contact resistance between GDL and CL decreases non-linearly from 0.044 to 0.0078 Ωcm^2 as the GDL was compressed from 300 to 140 μm thickness under the compression pressure.
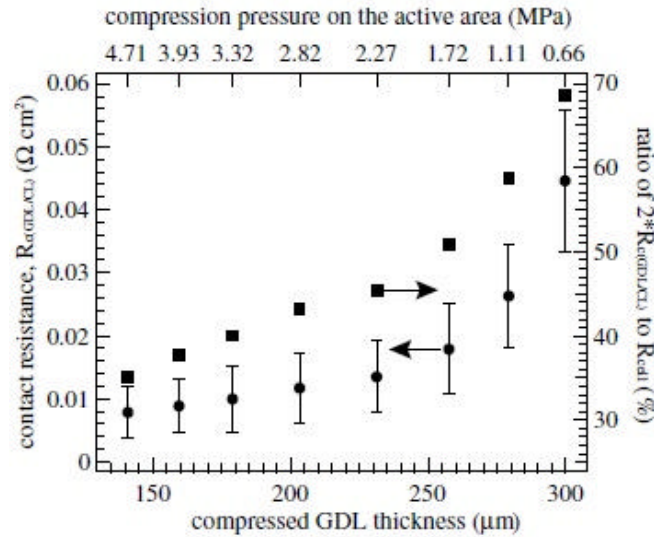

Figure 2-8: Contact resistance between the GDL and CL, and ratio of two of the contact resistance to total cell resistance (Reproduced from Nitta et al. [71])

In our simplified approach when not applying the thermodynamics of irreversible processes (TIP) the Ohmic polarization is one of the easiest to calculate thanks to Ohm's law when all resistances are known. It is expressed as follows:
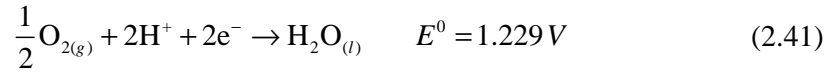
$$\eta_{Ohm} = iA\sum R \ , \tag{2.40}$$

where A is the area and R is the resistance. For PEM fuel cell the conductivity (reciprocal of resistivity) of the membrane is a function of the water content and the temperature. The detail of this coupled nature is discussed in section 2.8.4 and section 3.4 of this thesis.

2.5.4 Departure from Nernst potential

A considerable loss of potential (from theoretical 1.22 V to measured 1 ~ 0.9 V) in a PEM fuel cell at an open circuit condition (when no current is drawn from the cell) is thought to be because of H_2 cross-over and because of mixed cathode potential [52].

H_2 cross-over is actually due to the inability of the reaction sites to capture H_2 gas for the required oxidation at the anode catalyst layer. The un-oxidized H_2 gas then crosses the membrane and reaches the cathode side, where it reacts with oxygen. In this way the cell looses some hydrogen without converting it into protons and electrons. More importantly this cross over reduces the oxygen surface concentration at the cathode side where the unwanted reaction due to cross-over of H_2 takes place.

A mixed cathode potential is proposed as one of the reasons for the voltage drop at the open circuit condition [52]. It is thought to be because of the side reaction which occurs between the Pt surface and O_2 at cathode catalyst layer, forming PtO. These half-cell side reactions are shown in equations (2.41) and (2.42).

$$\frac{1}{2}O_{2(g)} + 2H^+ + 2e^- \rightarrow H_2O_{(l)} \qquad E^0 = 1.229\,V \qquad (2.41)$$

$$(2.42)$$
$$Pt + H_2O_{(l)} \rightarrow PtO + 2H^+ + 2e^- \qquad E^0 = 0.88\,V$$

This PtO formation reduces the pure Pt surface for the main oxidation-reduction reaction at the cathode catalyst layer. A similar reaction can occur at the anode as well, when O_2 permeates (in the so called O_2 cross-over) from the cathode to the anode. The gas cross-over is investigated by Inaba et al. [54], they conclude that the gas cross-over increases with increase in cell temperature, humidity and gas pressure. In addition hydrogen peroxide was detected in the drain water during open circuit voltage tests which suggests the formation of hydrogen peroxide due to the H_2 gas cross-over [54].

More recently Vilekar et al. [55] tried to explain the mechanism involved in the loss of voltage at open circuit conditions. They concluded that the hydrogen cross-over is more significant as compared with oxygen permeation, furthermore suggesting that the open circuit voltage (OCV) is an important diagnostic tool to determine the physical well-being of the membrane during prolonged operation. At open circuit condition there is no external current but there are internal short circuiting currents because of the minor un-wanted electron conductivity of the membrane and secondly because of the fuel cross-over at the anode and the cathode. Figure 2-9 clearly shows both internal short circuiting currents across the membrane along with their respective half-cell reactions, where the dotted line is indicating the electron movement.
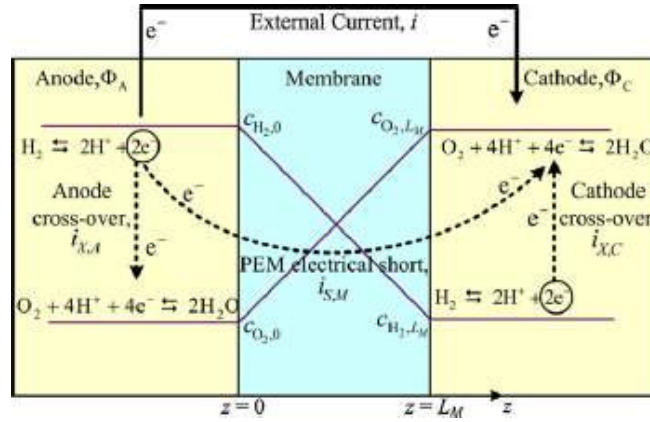
_____

Figure 2-9 : Schematic representation of internal currents and short circuiting (Ref [55]).

2.6 Heat released or absorbed by virtue of condensation or evaporation

Water has to be present in the PEM fuel cell sandwich for the purpose of the hydration of the membrane which is required for the proper conductivity of the membrane. Water is supplied through the gas channels by humidifying the reactant streams, and it is also produced at the cathode electrode as per equation (2.2). In the presence of water the PEM fuel cell is prone to have condensation sites where ever it finds cold spots and conversely to have evaporation sites at hot spots. There is a heat source or sink associated with evaporation or condensation process; thermodynamically it can be written as in equation (2.43).

$$Q_{rel/abs} = m_w \Delta h_v \qquad (2.43)$$

Where m_w represent quantity of water condensed or evaporated, Δh_v is the enthalpy of evaporation for water at a given temperature. As Δh_v is a very high value for example 2308.0 kJ/kg at 80°C for water [76], even traces of phase changing water are important.

2.7 Heat released or absorbed by virtue of sorption or desorption

Sorption refers to both absorption and adsorption processes taking place simultaneously. As water is present at the anode from humidification and formed at the cathode in the PEM fuel cell electrodes under an operating range of 60-80°C, there is a possibility of sorption and desorption phenomena to occur at the electrode interfaces. Water sorption, desorption, and permeation in Nafion based membranes were measured as functions of temperature between 30 and 90°C in reference [13]. Sorption processes are connected to the changes in enthalpy similar as phase changes, known as enthalpy of sorption. When the water molecules stick to the solid surface, loosing their kinetic energy, this kinetic energy is then converted into heat. This sorption and desorption phenomena depend upon the balance between the liquid and vapor phase of water present in the PEM fuel cell. The heat released or absorbed during sorption/desorption can be quantified through water flux at electrodes and sorption enthalpy as shown in equation (2.44).

$$Q_{rel/abs} = m_w^{a,c} \Delta h_{sorp} \tag{2.44}$$

Where $m_w^{a,c}$ representing the mass of water present in liquid phase at anode and cathode, Δh_{sorp} is the sorption enthalpy of water. By mass balance, taking into account the water produced during reaction and the net amount of water dragged by protons from the anode across the membrane to the cathode we can calculate the amount of water at the cathode $m_w^c = m_w^a + \dfrac{iM_w}{2F}$.

As pointed by Ramousse et al. [6] in certain cases the water sorption and desorption can generate important heat source and sink at electrodes for instance when one side of the membrane is in contact with dry hydrogen while the other is in contact with humidified air. Range of values of sorption enthalpy have been reported under different level of hydration for Nafion based membranes in the literature [10][11][12]. Most of the values are in the vicinity of enthalpy of evaporation of water i.e. 41.3 kJ/mol at 353 K. At a steady state operation the number of adsorbed molecules becomes constant, thus the energetic influence is considered only for the transitory period. Therefore, the energetic of sorption/desorption can be important when load change is made in the operation of the fuel cell stack or for the startup and shut down process.

2.8 Basics of Thermodynamic of irreversible processes (TIP)

TIP describes coupled transport processes within systems in a unifying manner on the basis of second law of thermodynamics. The systems under consideration are globally out of equilibrium but are locally in equilibrium. The idea behind TIP is to quantify the departure from equilibrium by means of entropic consideration using the assumption of continuum and local equilibrium. So TIP is utilizing the relations described by phenomenological (empirical) laws and the equilibrium thermodynamics, both are well developed branches of sciences. In classical thermodynamics, a system's entropy is not directly measurable but can be calculated by devising a reversible path from a reference state to the system's state and integrating $dS=\delta q_{rev}/T$ along the path [15]. For a non-equilibrium system, a reversible path is not available so scientists have devised an elegant way we know as TIP to calculate the entropy production for irreversible processes.

2.8.1 Local equilibrium

A system evolves into thermodynamic equilibrium by itself when it is left for long time with no external disturbances as depicted in [16]. The equilibrium is reached when there are no gradients of any driving potentials T, p and μ and thus no resulting fluxes (J) or reactions within the system.
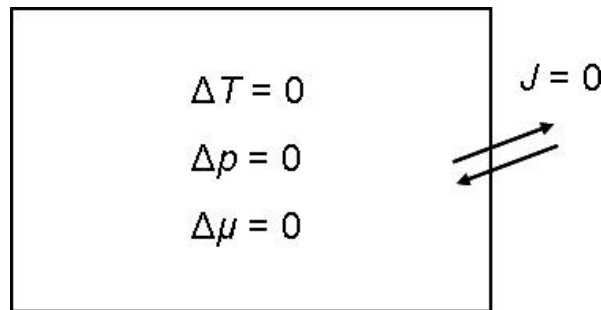
_____

Figure 2-10 : Equilibrium system

A condition for local equilibrium is based upon two characteristic times. The time required to reach equilibrium in a volume called local volume (which is fairly smaller than the volume of the global system) should be much shorter than the time required reaching equilibrium in the global system [16]. The local volume should be as small as possible, but still big enough to be treated as homogeneous and contains sufficient number of molecules. This is how we can think of a system which is not in global equilibrium but locally in equilibrium. A schematic of such a situation is shown in Figure 2-11, the assumption of local equilibrium is very central for the theory of the thermodynamics of irreversible processes.
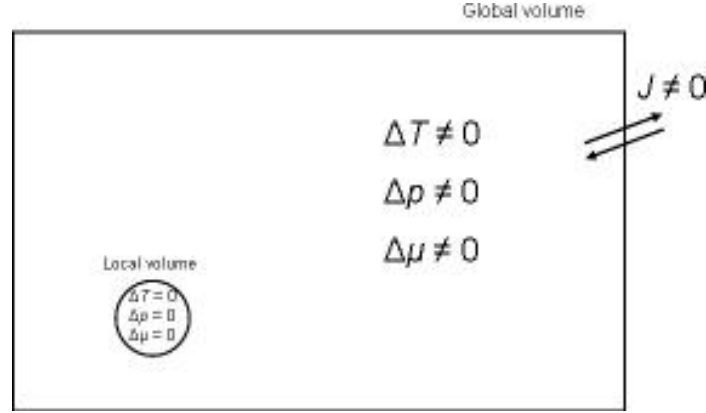
Figure 2-11 : Schematic of a non-equilibrium system with local equilibrium in elemental volume

2.8.2 Entropy production- fluxes and forces

Different irreversible transport and reaction processes are contributing to the entropy production in a system. A systematic way of describing all the contributions in terms of generalized fluxes and forces is shown in equation (2.45) where subscript k represent a process, J_k and X_k are so-called conjugate fluxes and forces of transport process k, and σ is the rate of entropy production per unit volume. A product between the forces and fluxes can be a normal product in case of scalar fluxes and forces (e.g chemical reaction) or dot product when fluxes and forces are vectors (e.g heat conduction), while double dot product when fluxes and forces are of second order tensors. (e.g viscous dissipation). The product of the flux and the force should be scalar, because entropy production rate is a scalar quantity.

$$\sigma = \sum_k J_k X_k \geq 0 \qquad\qquad (2.45)$$

The equation (2.45) embodies the second law of thermodynamics in a way that for non-equilibrium system the product of fluxes and forces is always positive, at equilibrium all the forces and their corresponding fluxes will vanish. As we see in the Table 2-4 the force (X) involves the gradient of intensive thermodynamic quantities while flux (J) involves the fluxes of heat, mass, charge and other extensive quantities. In order to calculate the entropy production using flux-force pairs we should have the information of field variables like temperature, chemical potential etc.

Table 2-4 : Pair of conjugate fluxes and forces with their units

	Flux (J)	Unit	Force (X)	Unit	Force(X) in 1D
Heat conduction	J_q	W/m^2	$\nabla \dfrac{1}{T}$	1/m K	$-\dfrac{1}{T^2}\dfrac{dT}{dz}$
Diffusion	J_i	mol/m^2 s	$-\nabla \dfrac{\mu_{i,T}}{T}$	J/mol m K	$-\dfrac{1}{T}\dfrac{d\mu_{i,T}}{dz}$
Electrical conduction	i	A/m^2	$\dfrac{-\nabla \phi}{T}$	V/m K	$-\dfrac{1}{T}\dfrac{d\phi}{dz}$
Chemical reactions	$\dfrac{\dot{\xi}_r}{V}$	mol/m^3 s	$\dfrac{A_r}{T}$	J/mol K	-
Viscous dissipation	τ	J/m^3	$-\dfrac{1}{T}\nabla \vec{v}$	1/s K	-

2.8.3 Phenomenological equations

In general fluxes and forces are complicated non linear functions of one another; which means that the flow of the flux is caused by several forces. At first place consider one of the flux J_1 which is due to n different forces, mathematically we can express as $J_1 = J_1(X_1, X_2, X_3, \dots X_n)$. Now we expand this function using a Taylor series about all equilibrium points, i.e at X_1, $X_2, \dots X_n = 0$ as given in equation (2.46) .

$$
\begin{aligned}
J_1(X_1, X_2, \dots X_n) = & \left(J_1(X_1 = 0) + \frac{\partial J_1}{\partial X_1}\bigg|_{X_1=0} X_1 + \frac{1}{2!}\frac{\partial^2 J_1}{\partial X_1^2}\bigg|_{X_1=0} X_1^2 + \dots \right) \\
& + \left(J_1(X_2 = 0) + \frac{\partial J_1}{\partial X_2}\bigg|_{X_2=0} X_2 + \frac{1}{2!}\frac{\partial^2 J_1}{\partial X_2^2}\bigg|_{X_2=0} X_2^2 + \dots \right) + \dots \quad (2.46) \\
& + \left(J_1(X_n = 0) + \frac{\partial J_1}{\partial X_n}\bigg|_{X_n=0} X_1 + \frac{1}{2!}\frac{\partial^2 J_1}{\partial X_n^2}\bigg|_{X_n=0} X_n^2 + \dots \right)
\end{aligned}
$$

If we disregard the higher order terms in equation (2.46), and apply the equilibrium condition $J_1(X_i=0)=0$ we get equation (2.47).

$$
J_1(X_1, X_2, \dots X_n) = \left(\frac{\partial J_1}{\partial X_1}\bigg|_{X_1=0} X_1 + \frac{\partial J_1}{\partial X_2}\bigg|_{X_2=0} X_2 + \dots + \frac{\partial J_1}{\partial X_n}\bigg|_{X_n=0} X_n \right) \quad (2.47)
$$

Similarly we can write equations for other fluxes $J_2, J_3, \dots J_n$ as shown in equation (2.48).

_____

$$J_2(X_1, X_2, \ldots X_n) = \left(\frac{\partial J_2}{\partial X_1}\bigg|_{X_1=0} X_1 + \frac{\partial J_2}{\partial X_2}\bigg|_{X_2=0} X_2 + \ldots + \frac{\partial J_2}{\partial X_n}\bigg|_{X_n=0} X_n \right)$$

$$J_3(X_1, X_2, \ldots X_n) = \left(\frac{\partial J_3}{\partial X_1}\bigg|_{X_1=0} X_1 + \frac{\partial J_3}{\partial X_2}\bigg|_{X_2=0} X_2 + \ldots + \frac{\partial J_3}{\partial X_n}\bigg|_{X_n=0} X_n \right) \qquad (2.48)$$

$$\vdots$$

$$J_n(X_1, X_2, \ldots X_n) = \left(\frac{\partial J_n}{\partial X_1}\bigg|_{X_1=0} X_1 + \frac{\partial J_n}{\partial X_2}\bigg|_{X_2=0} X_2 + \ldots + \frac{\partial J_n}{\partial X_n}\bigg|_{X_n=0} X_n \right)$$

In a compact form, the set of equations in (2.47) and (2.48) can be written as shown in equation (2.49).

$$J_i = \sum_j \frac{\partial J_i}{\partial X_j}\bigg|_{eq} X_j \qquad \text{where } (i,j = 1,2,3,\ldots n) \ . \qquad (2.49)$$

Another popular form in which we can write equation (2.49) is shown in equation (2.50), which is known as the linear phenomenological equation.

$$J_i = \sum_j L_{ij} X_j \qquad \text{where } (i,j = 1,2,3,\ldots n) \ . \qquad (2.50)$$

In equation (2.50), the coefficient L_{ij} is known as the phenomenological coefficient. The coefficients with same indices ($i=j$) relate conjugated fluxes and forces are known as direct coefficients (diagonal terms), whereas the coefficients with $i{\neq}j$ are the cross coefficients representing the coupling effects (off diagonal terms). This equation signifies that the flux depends linearly on all the driving forces.

Onsagers's principle states that when the forces and fluxes are chosen so that they are conjugate, the coupling coefficients are symmetric and written as shown in equation (2.51).

$$\frac{\partial J_i}{\partial X_j} = \frac{\partial J_j}{\partial X_i} \qquad \text{or} \qquad L_{ij} = L_{ji} \qquad (2.51)$$

The equation (2.51) shows that the change in flux of some quantity caused by changing the driving force for another is equal to the change in flux of the second quantity caused by changing the driving force for the first. A justification (experimental and statistical) of Onsager's principle can be found in several advanced texts [46] [83], which is based on microscopic reversibility for systems near equilibrium.

2.8.4 TIP in a PEM fuel cell membrane

Consider the transport of fluxes of heat, water and the current in the stationary state of the membrane in one dimension as depicted in Figure 2-12. We can easily put forward an equation for calculating the rate of entropy generation in the membrane using the fluxes and forces given in Table 2-4 and equation (2.45) as shown in equation (2.52). In this equation the subscript w represents water, q represents heat and the superscript m is signifying the membrane.
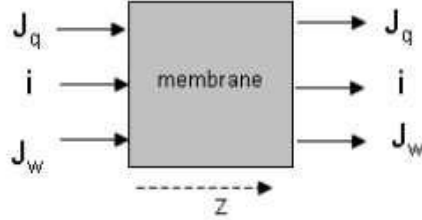
Figure 2-12 : Schematic of membrane with fluxes of water, electric current and heat

$$\sigma^m = -\frac{J_q}{T^2}\frac{dT}{dz} - \frac{J_w}{T}\frac{d\mu_{w,T}}{dz} - \frac{i}{T}\frac{d\phi}{dz}$$
(2.52)

Similarly equations of entropy production for the anode and cathode backing can be written as well. More elaborate description of the thermodynamics of irreversible process in a PEM fuel cell can be found in [46][47]. It is clear from equation (2.52) that the evaluation of the entropy production in the membrane is possible when we have the information of the field variables temperature, chemical potential and electric potential. Another important aspect of this equation is the comparison of the relative magnitude of the entropy production. For example at a high current density the effect of electrical conduction can surpass the effect of heat conduction. By using the linear flux-force relation given in the phenomenological equation (2.50) we can write this equation for the membrane as well.

$$J_q = -\frac{L_{qq}}{T^2}\frac{dT}{dz} - \frac{L_{qw}}{T}\frac{d\mu_{w,T}}{dz} - \frac{L_{q\phi}}{T}\frac{d\phi}{dz}$$
(2.53)

$$J_w = -\frac{L_{wq}}{T^2}\frac{dT}{dz} - \frac{L_{ww}}{T}\frac{d\mu_{w,T}}{dz} - \frac{L_{w\phi}}{T}\frac{d\phi}{dz}$$
(2.54)

$$i = -\frac{L_{\phi q}}{T^2}\frac{dT}{dz} - \frac{L_{\phi w}}{T}\frac{d\mu_{w,T}}{dz} - \frac{L_{\phi\phi}}{T}\frac{d\phi}{dz}$$
(2.55)

Here L_{ij} are representing the phenomenological coefficients, the indices q, w, and ϕ are available for heat, water and current transport respectively. The diagonal coefficients with the same indices can be related to the well known transport coefficients like thermal conductivity, diffusion coefficient, and electrical conductivity. The off diagonal coefficients with different indices are showing the coupling effect of different fluxes like thermo-diffusion or thermo-electric effect. The use of Onsager's reciprocal relations in the set of flux-force equations (2.53) to (2.55) can reduce the number of independent coefficients L_{ij} from nine to six. The

_____

magnitude of coupling terms can be crucial in some cases, for example in the membrane the electro osmotic effect (the coupling between water and electric current) plays an important role. It is important to understand the role of coupling terms. For example if we measure the electric current in the stationary state when there is no transport of heat and water, i.e $J_q=J_w=0$ there is a coupling effect leading to a temperature and chemical potential gradient, which also effect the electric current. This is clear from equation (2.56), which has come from the force-flux equation (2.53) to (2.55) by taking the condition $J_q=J_w=0$ and assuming $E = -\dfrac{d\phi}{dz}$. The derivation is given in Appendix-A.

$$ i = \frac{E}{T}\left[L_{\phi\phi} - L_{\phi q}\frac{L_{q\phi}L_{ww} - L_{qw}L_{w\phi}}{L_{qq}L_{ww} - L_{qw}^{2}} - L_{\phi w}\frac{L_{qq}L_{w\phi} - L_{wq}L_{q\phi}}{L_{qq}L_{ww} - L_{qw}^{2}} \right] \tag{2.56} $$

The electric current measured for a homogenous conductor using Ohm's law can be viewed from equation (2.55) after substituting $dT/dz = d\mu_{w,T}/dz = 0$ resulting in equation (2.57).

$$ i = -\frac{L_{\phi\phi}}{T}\frac{d\phi}{dz} \tag{2.57} $$

Ohm's law is expressed as in equation (2.58).

$$ i = -\kappa\frac{d\phi}{dz} \tag{2.58} $$

By comparing equation (2.57) and (2.58) the electrical conductivity comes out to be $\kappa = L_{\phi\phi}/T$ in the case of vanishing temperature and chemical potential gradients. The electrical conductivity judged from equation (2.56) will be different from equation (2.57) because of the coupling terms. The force-flux relations can be simplified by eliminating the electric potential gradient term from equation (2.53) and (2.54) resulting in equation (2.59) and (2.60).

$$ J_q = -\frac{l_{qq}}{T^2}\frac{dT}{dz} - \frac{l_{qw}}{T}\frac{d\mu_{w,T}}{dz} + \frac{L_{q\phi}}{L_{\phi\phi}}i \tag{2.59} $$

$$ J_w = -\frac{l_{wq}}{T^2}\frac{dT}{dz} - \frac{l_{ww}}{T}\frac{d\mu_{w,T}}{dz} + \frac{L_{w\phi}}{L_{\phi\phi}}i \tag{2.60} $$

Here l_{ij} coefficients are related by

$$ l_{ij} = L_{ij} - \frac{L_{\phi i}L_{j\phi}}{L_{\phi\phi}} \tag{2.61} $$

For further simplification we need to define some appropriate coefficients taking into account the coupling effects:

The water transfer number t_w is defined for the electro-osmotic coupling of water and electricity. It is the ratio of water flux to proton flux in a condition when temperature and chemical potential gradients are vanishing. Mathematically this can be expressed as equation (2.62).

$$t_w = \left(\frac{J_w}{i/F} \right)_{d\mu_{w,T}=dT=0} = F \frac{L_{w\phi}}{L_{\phi\phi}} \tag{2.62}$$

The Peltier coefficient is defined as

$$\pi = \left(\frac{J_q}{i/F} \right)_{d\mu_{w,T}=dT=0} = F \frac{L_{q\phi}}{L_{\phi\phi}} \tag{2.63}$$

The measurable heat of transfer is

$$q^* = \left(\frac{J_q}{J_w} \right)_{i=dT=0} = \frac{l_{qw}}{l_{ww}} \tag{2.64}$$

The coefficients defined in equation (2.62) to (2.64) can be easily verified by substituting the respective conditions in equation (2.53) to (2.55). From equation (2.60) we solve for the chemical potential gradient term for water and substitute the water transfer number and measurable heat of transfer to get equation (2.65). The Onsager reciprocal relation $l_{wq}=l_{qw}$ has been used as well.

$$\frac{d\mu_{w,T}}{dz} = -\frac{q^*}{T}\frac{dT}{dz} - \frac{T}{l_{ww}}\left(J_w - t_w \frac{i}{F} \right) \tag{2.65}$$

By substituting the value of the chemical potential gradient and the Peltier coefficient in equation (2.59) results in a equation for the temperature gradient as equation (2.66).

$$\frac{dT}{dz} = -\frac{1}{\lambda}\left[J_q - q^*\left(J_w - t_w \frac{i}{F} \right) - \pi \frac{i}{F} \right] \quad \text{where} \quad \lambda = \frac{l_{qq}}{T^2} - (q^*)^2 \frac{l_{ww}}{T^2} \tag{2.66}$$

Substituting t_w, π and the electrical conductivity κ into equation (2.55) results in a equation for potential gradient.

$$\frac{d\phi}{dz} = -\frac{\pi}{TF}\frac{dT}{dz} - \frac{t_w}{F}\frac{d\mu}{dz} - \frac{i}{\kappa} \tag{2.67}$$

_____

The conductivity of proton exchange membranes is highly dependent on the water content λ_w of the membrane, because of the water assisted mechanism of proton transport. In reference [40] the empirical relation between water activity a_w and membrane water content is presented for a Nafion membrane at 80ºC when the activity is less than 1 as given in equation (2.68), here the water activity is calculated from the definition $a_w = \dfrac{p_w}{p_s(T)}$. Here the saturation pressure can be calculated from equation (3.11), coming later in chapter 3.

$$\lambda_w = 0.3 + 10.8\, a_w - 16.0\, a_w^{\,2} + 14.1\, a_w^{\,3} \tag{2.68}$$

The molar water concentration C_w can be calculated from equation (2.69) from reference [46], here ρ_m is the membrane dry density and M is the molar mass of the polymer in the membrane.

$$C_w = \frac{\lambda_w \rho_m}{M} \tag{2.69}$$

The phenomenological diffusion coefficient is defined in terms of molar concentrations as:

$$\frac{l_{ww}}{T} = D_w \frac{C_w}{RT} \quad . \tag{2.70}$$

The derivation is available in Appendix-B.

 The chemical potential of water is defined as

$$\mu_w = \mu_w^{\,0} + RT \ln a_w \tag{2.71}$$

By using the chain rule $\dfrac{d\mu}{dz} = \dfrac{d\mu}{da_w}\dfrac{da_w}{dz}$ and definitions given in equation (2.68) to (2.71), after substitution in (2.65) and (2.67), this results in equation (2.72) and (2.73) respectively.

$$\frac{da_w}{dz} = -\frac{a_w q^*}{RT^2}\frac{dT}{dz} - \frac{a_w M}{\lambda_w \rho_m D_w}\left(J_w - t_w \frac{i}{F}\right) \tag{2.72}$$

$$\frac{d\phi}{dz} = -\frac{\pi}{TF}\frac{dT}{dz} - \frac{t_w RT}{a_w F}\frac{da_w}{dz} - \frac{i}{\kappa} \quad . \tag{2.73}$$

The Peltier coefficient π and heat of transfer for the membrane is calculated as given in reference [46].

$$\frac{\pi}{T} = S^*_{H^+} - t_w S_w \quad \text{and} \quad q^* = -T S_w \ . \tag{2.74}$$

Here $S^*_{H^+}$ is the transported entropy of proton per mole basis, S_w is the entropy of water. In reference [46] the value of $S^*_{H^+} - t_w S_w$ is taken from the work of [48] which is an experimental result for Nafion®-117 with Ag-AgCl electrodes. For solid electrodes the value of the Peltier coefficient is to the knowledge of the author, not available in the open literature.

From the energy balance across the membrane at a stationary state we get that

$$\frac{d}{dz}\left(J_q + i\phi + J_w h_w\right) = 0 \ . \tag{2.75}$$

Here h_w is the enthalpy of water. In order to solve the set of equations (2.66),(2.72) and (2.73) for gradients of temperature, water activity and electric potential respectively in the membrane it is required to know the transport parameters λ, D_w, t_w, and κ.

The diffusion coefficient and the electrical conductivity are dependent on the water content and on the temperature. There are differences in the values used by different authors for these important transport parameters. For the diffusion coefficient D_w in (cm^2/s) the equation (2.76) is used in the work of [47]. The Figure 2-13 shows the strong dependence with temperature.

$$D_w = \frac{5\times10^{-6}}{1+\left(\dfrac{4.47}{\lambda_w}\right)^{2.85}} e^{2416\left(\frac{1}{303}-\frac{1}{T}\right)} \tag{2.76}$$
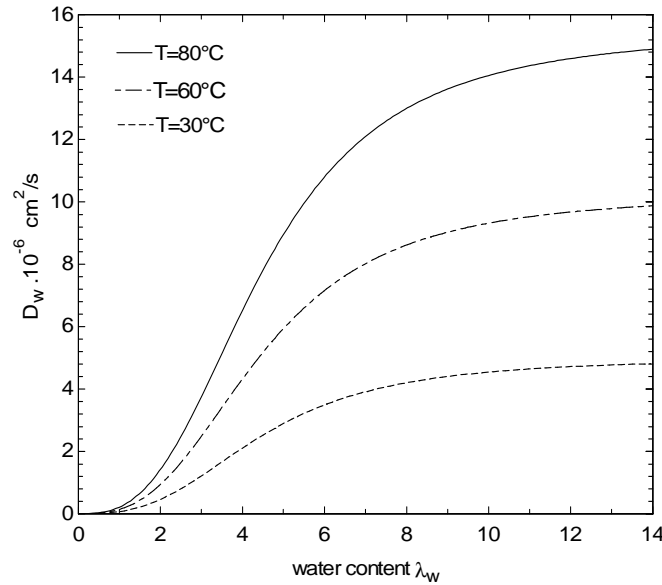

Figure 2-13 : Diffusion coefficient for water at different temperatures by equation (2.76)

For the membrane electrical conductivity as proposed by Springer et al. [37] we have

$$\kappa = (0.5193\lambda_w - 0.326)\, e^{1268\left(\frac{1}{303}-\frac{1}{T}\right)}\,. \tag{2.77}$$

For the water transfer number a linear relation is given in [37] as

$$t_w = 2.5\frac{\lambda_w}{22} \tag{2.78}$$

The thermal conductivity λ for the water saturated membrane is assumed to be a constant value by several authors, taken to be 0.43 W/mK [47], whereas a lower value 0.2 W/mK is used in the work of [46]. The molar mass M and the membrane density ρ_m can be assumed to be a constant value depending upon the type of the membrane.

This one dimensional analysis of homogeneous membrane using irreversible thermodynamics concluded from the set of equations (2.66),(2.72) and (2.73) clearly indicates the coupling of heat , water and electric potential across the membrane. A water content dictated by the operating conditions (p, T, i) affects the whole set of equations.

Entropy production rate for membrane calculated at different current densities calculated by Siemer [47] using TIP is shown in Figure 2-14. This one dimensional result shows that the rate of entropy production in a PEM fuel cell membrane increases substantially at higher current densities.
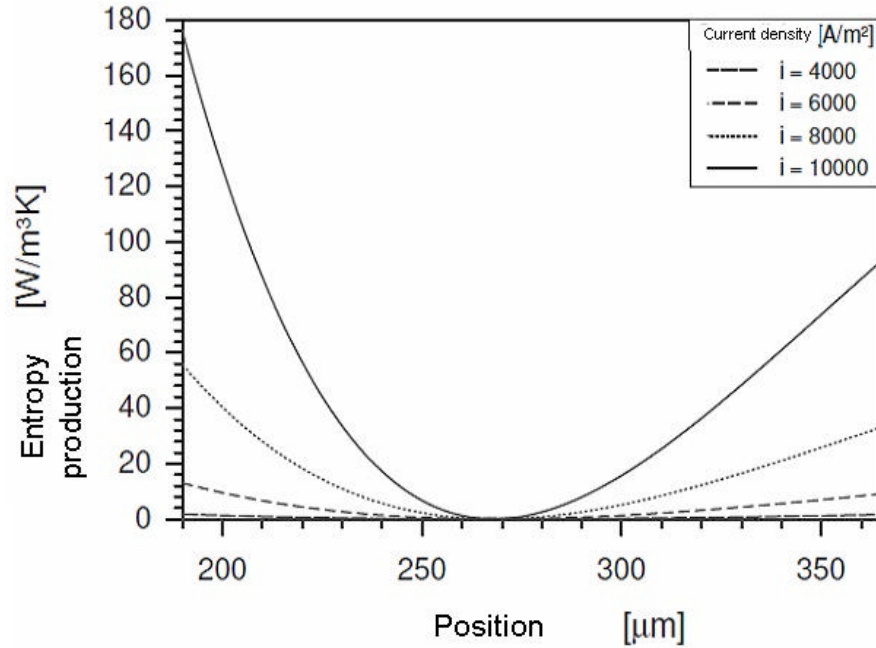

Figure 2-14 : Entropy production rate for PEM fuel cell membrane at different current densities (Ref [47]).

A similar analysis like membrane can be employed for electrodes as well. Kjelstrup [46] and Siemer [47] have analyzed the PEM fuel cell in one dimension using the principle of irreversible thermodynamics, and have shown the temperature distribution as a function of current density.

_____

Figure 2-15 shows the temperature distribution in a PEM fuel as a function of current density from the work of Siemer [47]. His results report slightly higher temperatures at higher value of current density and the center of the membrane supposed to be at the maximum temperature. One must keep in mind the boundary condition and the values of the parameters used in the model before making any conclusion from the results.
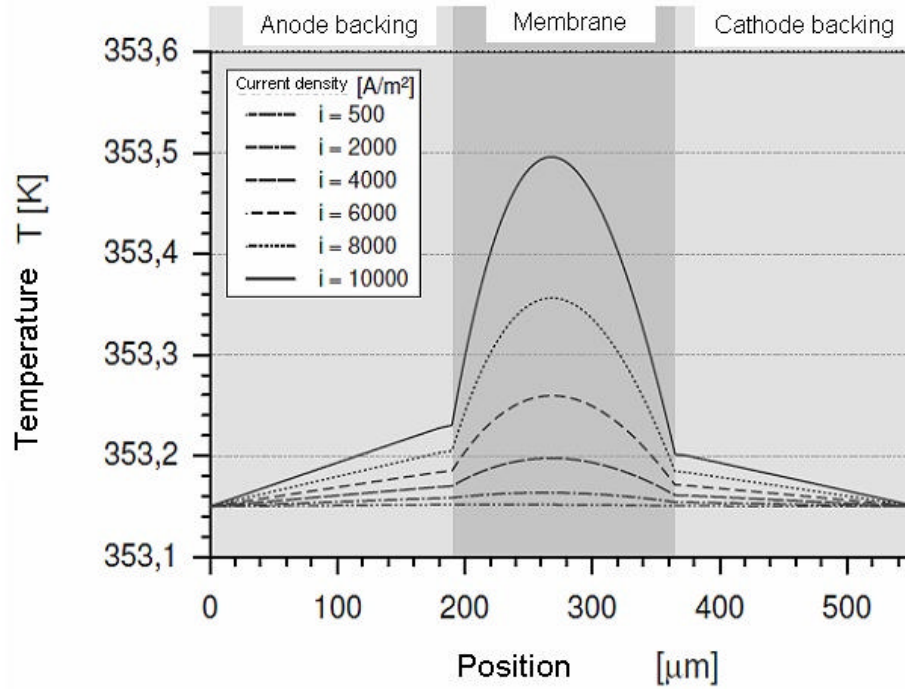

Figure 2-15 : Temperature distribution at different current densities using TIP (Ref [47]).

_____

3 Detailed heat source analysis of one single cell

In the previous chapter we have outlined the sources of heat in general; this chapter focuses on detailed single cell analysis resulting in a heat flux distribution at both electrodes. At first we will define the local current density for a single cell which is based upon the local concentration profiles of the reactants, second the description of the CFD model is presented which was used to calculate the concentration profiles. The next section describes the procedure to calculate the activation over-potentials and Ohmic losses. In the end the heat flux distribution is shown which is based upon the reversible and the irreversible part of the heat generation. A strategy to get the feeling of heat distribution in a stack is perceived first by analyzing the single fuel cell closely and digging out the major contributors of heat generation, this will result in a simplified heat flux distribution; then later this heat flux is employed to analyze a commercial size stack. The following sections describe the procedure adopted in this study.

3.1 Modeling local current density

In a fuel cell the concentration of the reactants decreases as the reactants move along the flow field of the bipolar plate something like shown in Figure 3-1 and Figure 3-2. The local current density will be a function of both reactant concentrations, among other variables, as depicted mathematically in equation (3.1). Here i is the local current density, i_{cell} is the average current density at which the fuel cell is intended to operate, C_{H_2} and C_{O_2} are the hydrogen and oxygen concentrations, these concentrations are normalized by the area average reactant concentrations represented by $C_{H_2,avg}$ and $C_{O_2,avg}$. The exponent 0.5 for the oxygen concentration term and unity for the hydrogen concentration term in equation (3.1) is by virtue of the mole components involved in the overall reaction of the fuel cell shown in equation (2.3).

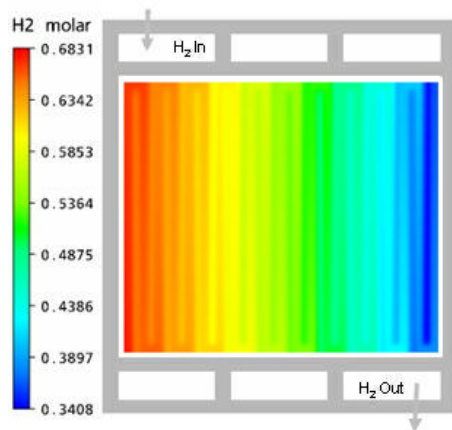$$i = i_{cell}\left[\frac{C_{H_2}}{C_{H_2,avg}}\left(\frac{C_{O_2}}{C_{O_2,avg}}\right)^{0.5}\right] \qquad (3.1)$$

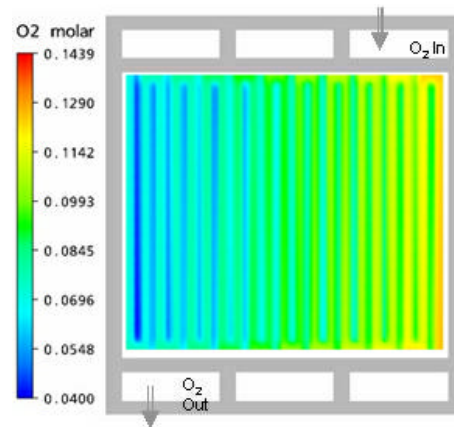**Figure 3-1 : H₂ molar concentration in serpentine flow field**

Figure 3-2 : O₂ molar concentration in serpentine flow field

44

_____

The formulation depicted in equation (3.1) for calculating the local current density is different from the literature in a way that the local current density is a function of both concentrations of the reactants, and practically we also measure one current from the cell, not two different current densities at each electrode. Actually the activation polarization at each electrode is different depending upon the local concentration of the respective reactants. This point is emphasized in the later section regarding activation polarization. The way we proceed here to find the local distribution of current density is of course still somewhat artificial and simplified. The real current density is gained in a full simulation including all mechanisms. This is not known.

3.2 Modeling local concentration profile

The concentrations profiles as shown in Figure 3-1 and Figure 3-2 for the reactants are produced using a CFD model. The following sub-sections give the detail of the model.

3.2.1 Model assumptions

A single phase multi-component CFD model is used. It consists of two different domains, reactants are supplied at entrance conditions at the anode and cathode gas channels inlets with a serpentine flow field as the fluid domains, whereas the gas diffusion layer (GDL) is taken as a porous media by incorporating the Darcy model. The sources and sinks for reactants are employed in the species transport equations. The following assumptions are made in the model:

1. Reactant gases are ideal gases.

2. Flow in the gas channel is laminar (because gas velocities are low).

3. The calculation is based on a multi-component mixture and single phase analysis. This means that each component (H_2, O_2, H_2O, N_2) has the same velocity and temperature field.

4. Steady state analysis.

5. Isothermal model (of course the local heat source distribution will give rise to a non-homogeneous temperature field across the cell, but for a first iteration a constant temperature is assumed).

It is assumed that other factors of influence, as for example the local concentration of platinum catalyst, the local porosity and tortuosity, the flow channel cross sections etc are homogeneous.

3.2.2 Model equations

The following conservation balance equations have been used in this model.

For mass conservation:

$$\nabla . (\rho U) = 0 \qquad\qquad (3.2)$$

For momentum conservation:

$$\nabla.(\rho U \otimes U) = -\nabla p + \nabla.(\mu \nabla U) + S_m \tag{3.3}$$

For species transport:

$$\nabla.(\bar{\rho}_i \bar{U}_j Y_i) = \nabla.(D_{i,eff} \nabla Y_i) + S_i \tag{3.4}$$

In the species transport equation $\bar{\rho}_i$ is the mass-average density of fluid component i in the mixture, $\bar{U}_j$ is the mass-average velocity field, j is representing the x,y,z components of the velocity U=U(x,y,z). $D_{i,eff}$ is the effective diffusivity and Y_i is the mass fraction of component i. In the above governing CFD equations S_m, S_i are the source terms for momentum, and species transport equations respectively which are given in equation (3.5). Because of the chemical reaction at the interface of the GDL and membrane the sources for the species transport are employed as follows:

$$S_{H_2} = -\frac{M_{H_2} iA}{2F}, \quad S_{O_2} = -\frac{M_{O_2} iA}{4F}, \quad S_{H_2O} = \frac{M_{H_2O} iA}{2F} \tag{3.5}$$

The negative sign shows the consumption of the species whereas the positive sign is the generation of species in above species source terms. M is the molecular weight of the species. The porous domain of the GDL is modeled using Darcy law by incorporating the source term in the momentum equation which is as follows:

$$\nabla p = \frac{\mu}{k_p} U \quad, \tag{3.6}$$

where k_p is the permeability, and μ is the dynamic viscosity of the mixture. Porosity is required in the porous domain like the GDL. Multi-component flow assumes that components of the fluid are mixed at the molecular level and that they have a common velocity, pressure and temperature field. Properties of the mixture are based upon the proportion of the components along with their thermodynamic state which are then calculated in a simplified manner as:

$$\phi = \sum_{i=A,B,...}^{N} \phi_i Y_i \tag{3.7}$$

where A,B,C are components, Y is the mass fraction of the component and ϕ is an arbitrary property. It can be the specific volume, specific heat capacity, viscosity, thermal conductivity etc. For example to calculate the multi-component mixture density using above relation is as follows:

$$v = \frac{1}{\rho} = \sum_{i=A,B,...}^{N} \frac{Y_i}{\rho_i} \tag{3.8}$$

Here ρ_i is the thermodynamic density of the component.

3.2.3 Boundary conditions

At the inlet of the gas channels the mass flow rates are given based on the stoichiometry and the mass fractions of the reactant components.

$$\dot{m}_i = \frac{\lambda S_i}{Y_i} \quad \text{where} \quad Y_i = \frac{M_i}{\overline{M}} X_i \quad \text{and} \quad \overline{M} = \sum_i X_i M_i \tag{3.9}$$

here $\dot{m}_i$ is the mass flow rate of specie i, λ is the stoichiometric ratio, S_i is the source term of specie i as given in equation (3.5) and X_i is the molar fraction of species. The mole fraction of water vapor is calculated using the definition of relative humidity.

$$RH = \frac{X_{wv} P}{P_s(T)} \quad \text{where} \quad X_{wv} = 1 - \sum_i X_i \tag{3.10}$$

Here RH is the relative humidity and X_{wv} is the mole fraction of water vapors which can be calculated from the definition that the sum of the mole fraction is unity in a multi-component mixture. The saturation pressure of water at a given temperature is evaluated using equation (3.11) developed by Wagner, taken from Baehr and Kabelac [76].

$$\ln\left(\frac{P_s(T)}{P_c}\right) = \frac{1}{T_r}\left[a_1(1-T_r)^{n_1} + a_2(1-T_r)^{n_2} + ... + a_6(1-T_r)^{n_6}\right], \tag{3.11}$$

where $T_r = T/T_c$ and P_c, T_c are the critical pressure and temperature respectively. The coefficients and exponents used in equation (3.11) are given in Table 3-1.

Table 3-1 : Parameters for the calculation of saturation pressure in equation (3.11), Ref [76]

For water: $T_c = 647.096 \, \text{K}$, $P_c = 22.064 \, \text{MPa}$			
$a_1 = -7.85951783$	$a_2 = 1.84408259$	$n_1 = 1.0$	$n_2 = 1.5$
$a_3 = -11.7866497$	$a_4 = 22.6807411$	$n_3 = 3.0$	$n_4 = 3.5$
$a_5 = -15.9618719$	$a_6 = 1.80122502$	$n_5 = 4.0$	$n_6 = 7.5$

At the outlet of the gas channels the static pressure boundary conditions are employed.

3.3 Modeling the activation polarization

The PEM fuel cell performance is very much depending upon the polarization due to the activation at the electrodes. As shown in Figure 3-3, the activation polarization for the anode is much smaller than the cathode at a given operating condition [39].
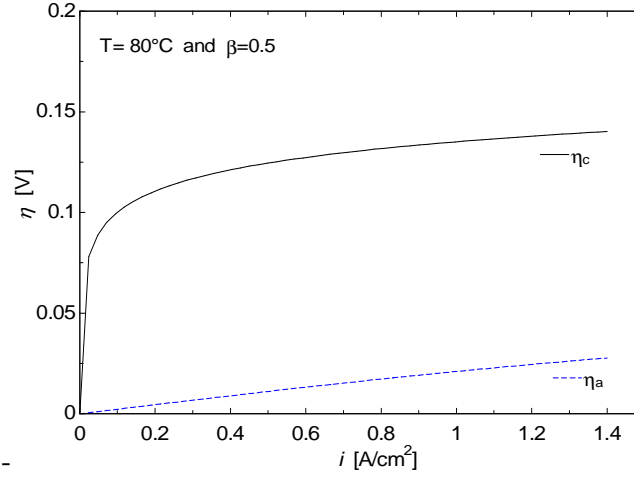
Figure 3-3 : Activation polarization for cathode and anode

Since the activation is an electrode/electrolyte phenomenon, the activation polarization at each electrode is a function of the respective reactant concentration, mathematically this can be expressed as follows:

$$\eta^a = f(C_{H_2}) \quad and \quad \eta^c = f(C_{O_2}) \tag{3.12}$$

Here the superscript a and c represent anode and cathode respectively. At a given operating current density the activation over-potentials are calculated for both electrodes using the Butler Volmer [39] formulation as follows:

$$i = i_0\left(e^{\frac{\beta n F}{RT}\eta} - e^{\frac{-(1-\beta)nF}{RT}\eta}\right), \quad where \quad i_0 = i_{0ref} a_c L_c \left(\frac{p}{p_{ref}}\right)^\gamma e^{\left[\frac{E_c}{RT}\left(1-\frac{T}{T_{ref}}\right)\right]} \tag{3.13}$$

The above equation comprises a plethora of parameters like the reference exchange current density i_{0ref}, catalyst specific area a_c, catalyst loading L_c, symmetry factor β, number of electron transferred per mole of the reacting species $n,$ and activation energy E_c. The numerical values of these parameters for the specific example case used in this thesis are given in Table 3-2 taken from Ref [39]. The reference condition is 1 bar and 298.15 K.

Table 3-2: Operating and kinetic parameters

	anode	cathode
Reference exchange current density i_{0ref} (A/cm²)	4.5×10^{-4}	3×10^{-9}
Platinum catalyst loading L_c (mg/cm²)	0.4	0.6
Activation energy E_c (kJ/mol)	18	66
Catalyst specific area a_c (cm²/mg)	1000	1000
No of electron transferred n	2	4
Concentration parameter γ	1	0.5

This Buttler-Volmer formulation is very sensitive to the parameters used. As shown in Figure 3-4 and Figure 3-5, the activation polarization at the cathode depends non-linearly upon the local temperature and the symmetry factor β.
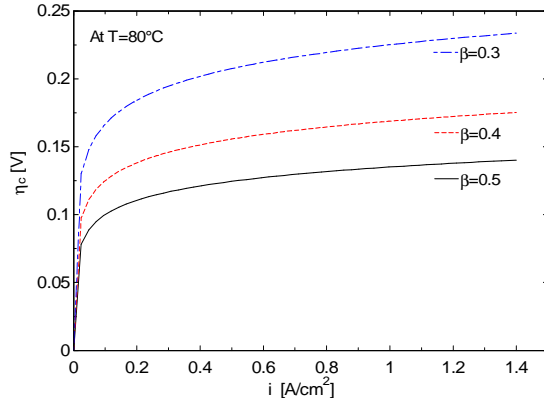

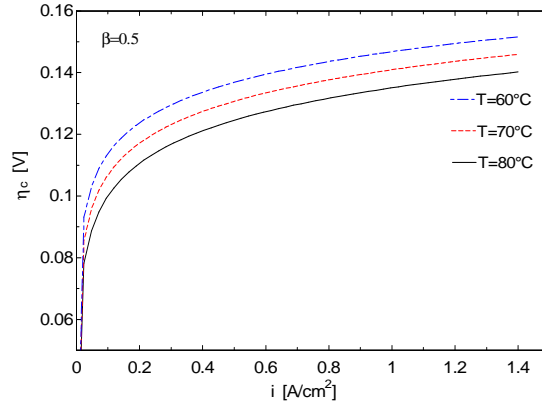**Figure 3-4 : Cathode over potential at different values of symmetric factor, β**

Figure 3-5 : Cathode over potential for different temperatures, T

The formulation given in equation (3.13) is good for a single step reaction mechanism within single cells. For complex multistep reactions, where the number of electrons transferred varies before and after the rate determining step, a more involved version of the Butler-Volmer equation is required as given in advanced texts like reference [17] or [18]. Attention is required in using the family of Butler-Volmer equations about their limitations, accuracy and applicability [19].

3.4   Modeling the Ohmic losses

The Ohmic losses are dominant in the membrane because of the high ionic resistance. From Ohm's law and the definition of the conductivity (reciprocal of resitivity) we can calculate the Ohmic loss from equation (3.14) where t_m is the membrane thickness and κ is the conductivity.

$$\eta_{ohm} = iR \quad \text{where} \quad R = \frac{t_m}{\kappa} \tag{3.14}$$

As it is known from several studies that the ionic conductivity of the polymer membrane is a function of water content λ_w, which is commonly written in terms of water activity. This is basically the ratio of actual water vapor pressure to the saturation pressure at a given temperature. A typical water content relationship for Nafion® based membrane at a given temperature is drawn in Figure 3-6 from the fitted empirical relations given in the references [37] and [40]. The water uptake of persulfonic acid membrane depends upon the immersion temperature, thickness of the membrane, ion exchange capacity (equivalent weights) of the membrane, and the pretreatment of the membrane [40].
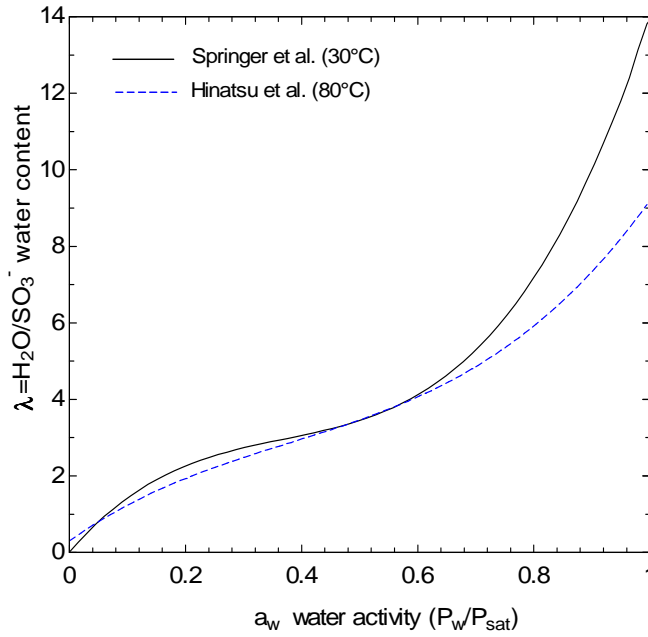
Figure 3-6 : Water content versus water activity

The water content in the Nafion® based membrane is lower when equilibrated in a vapor phase as compared with a liquid phase. In literature [41] this effect is known as Schroeder's paradox.

The conductivity of the membrane is also a strong function of temperature, which is usually correlated by equation (3.15), where κ is the conductivity in S/m and T is the temperature in K, reference [37].

$$\kappa = (0.5193\lambda_w - 0.326)\, e^{1268\left(\frac{1}{303} - \frac{1}{T}\right)} \tag{3.15}$$

In this study we have assumed that the membrane is fully humidified, so the water activity is about unity, so the value of water content $\lambda_w = 14$ and $T = 353.15$ K is taken for the calculation of the conductivity using equation (3.15) resulting in a conductivity of $\kappa = 12.58$ S/m. The heat flux contribution due to ohmic resistance is equally divided to happen at both electrodes; schematically it is shown in Figure 3-7.
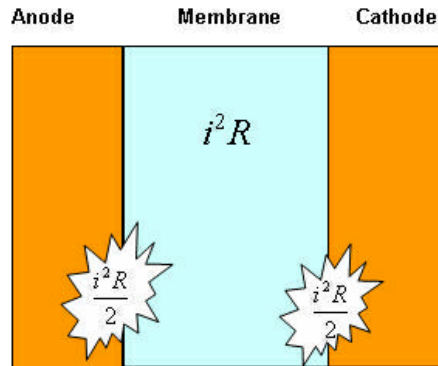
Figure 3-7 : Ohmic loses are equally distributed at each electrode

_____

3.5 Calculating local heat fluxes

The heat source within a cell is divided into two major parts; reversible and irreversible heat generation as discussed in the previous chapter. The local value of heat flux is calculated from equation (3.16), the first term is representing the reversible part and the second term is the irreversible part comprising the over-potentials.

$$q = \frac{T\Delta S}{nF}i + i\sum\eta \tag{3.16}$$

At each individual electrode the heat flux is calculated from equation (3.17) and (3.18).

$$q^a = \frac{T\Delta S^a}{2F}i + (\eta_{act}^a + \eta_{ohm}^a)i \tag{3.17}$$

$$q^c = \frac{T\Delta S^c}{4F}i + (\eta_{act}^c + \eta_{ohm}^c)i \tag{3.18}$$

Heat source due to evaporation/condensation is not included in above equations because our CFD model is based on single phase, we don't have the local distribution of water in the liquid phase. As we know from the previous chapter that the entropy change due to reaction at an individual electrode is differently presented by several different authors which results in a different heat flux distribution at anode and cathode. In most of the non-isothermal CFD models of the PEM fuel cell the result of Lampinen [5] for the entropy change is quoted. In Figure 3-8 and Figure 3-9 a heat flux distribution is shown using the entropy change given by Lampinen et al., which shows higher values of heat flux at the cathode as compared with the anode. These calculations are performed on the configuration as shown in Figure 3-1 and Figure 3-2, where hydrogen is coming from one corner and oxygen is supplied from the other corner.
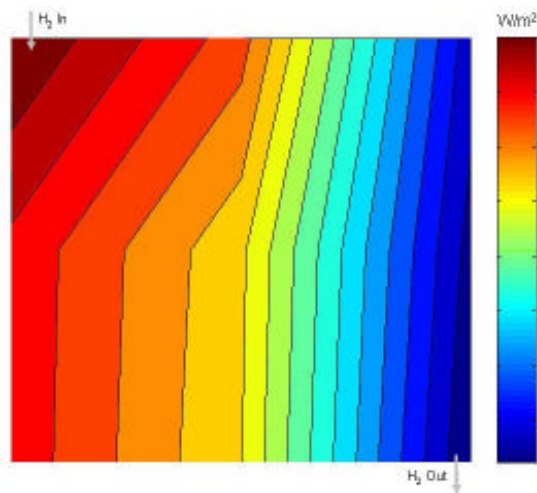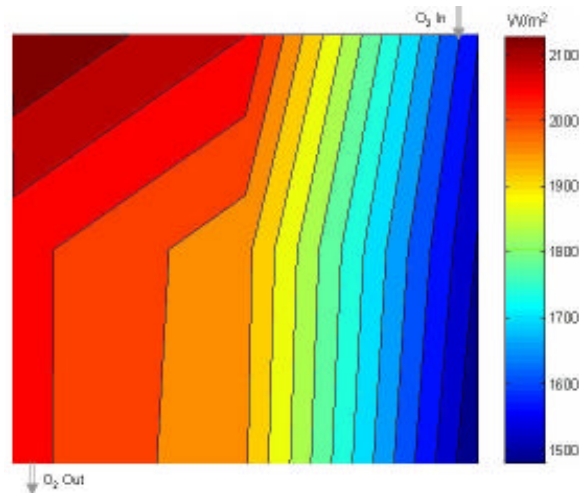

Figure 3-8 : Heat flux distribution at anode **Figure 3-9 : Heat flux distribution at cathode**

_____

The overall procedure used in this study is summarized in the flow chart as shown in Figure 3-10. A rough check is that we take the sum of the average heat fluxes at both electrodes which comes to be $\bar{q} = 1860$ W/m^2, this value has the same order as if we assume that the fuel cell has an overall energy efficiency of $P^{el}/\dot{m}\Delta H = 0.5$ using air as an oxidant. The power density typically is 2000 W/m^2.
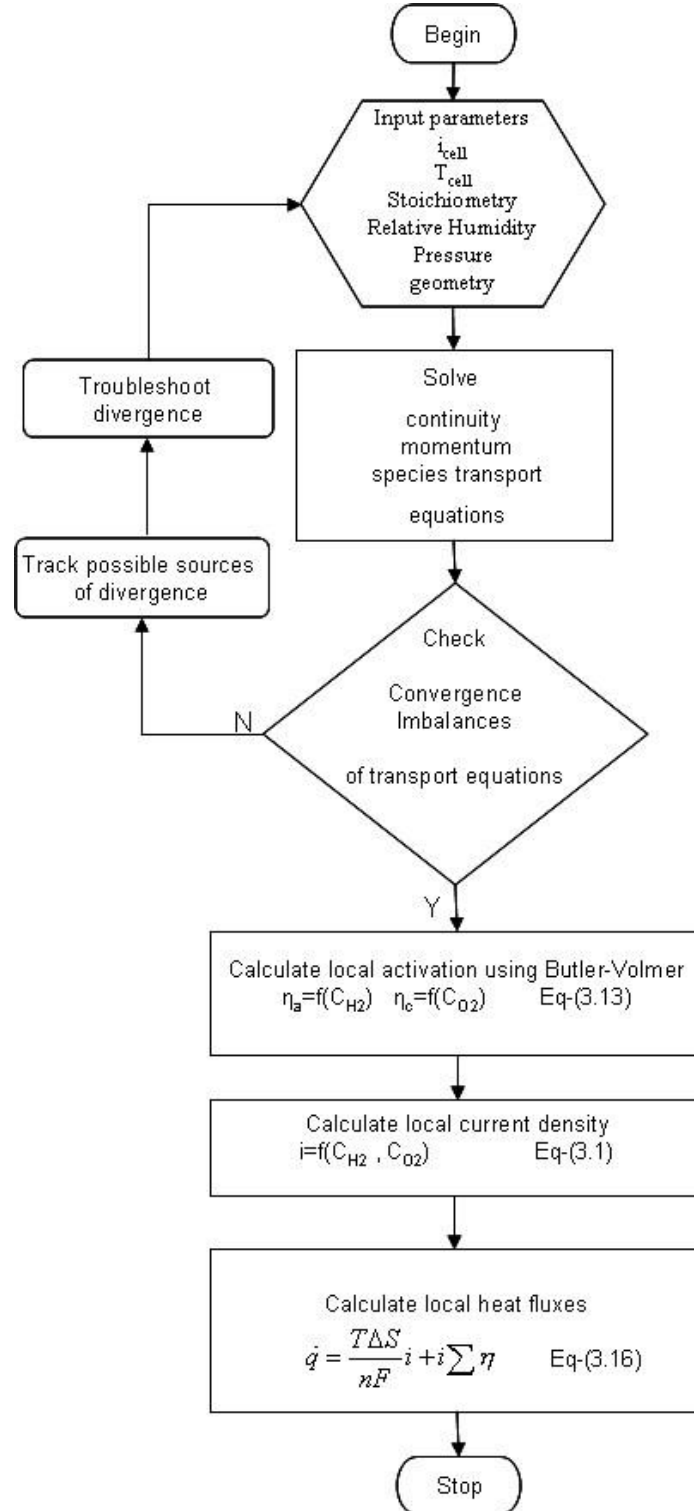

Figure 3-10 : Flow chart for the calculation of heat fluxes

_____

4 Parameter variation for examining heat sources

The heat source distribution depends upon several factors like stack configurations and a variation of properties for the material used in PEM fuel cell stack as the porosity of gas diffusion layer, the thermal conductivity of the membrane etc. In the first section of this chapter the local current density distribution is shown for two possible flow reactant arrangements in a stack. The second section shows the variation in local current density distribution when the porosity of the GDL changes from $\varepsilon = 0.4$ to 0.6, keeping a fixed value of permeability. These local current density distributions finally are responsible for the heat flux distribution as described in the previous chapter. The last section shows the sensitivity of the heat flux on the temperature distribution of a 50 cell stack.

4.1 Variation of stack-flow configurations

The stack configuration dictates the distribution of reactant concentration in the flow field which consequently determines the possibility of higher and lower reaction rates and the hot and cold spots. A variety of stack configurations are employed in practice depending upon the flow direction of reactants and coolant, two of the possible configurations are shown in Figure 4-1 and Figure 4-2. The Z-type is one in which reactants and also the coolant are sent from one of the side of the stack and leave from the other side of the stack, whereas in U-type configurations flows come in and go out from the same side of the stack. The use of the particular type of the configuration is depending upon the space and design requirement for a particular installation. In automotive applications, because of the intended compactness and flexibility, both space and direction of flow are important aspects for the stack design. Another aspect is the plurality of stack construction, for a given power requirement one can use a different number of stacks in series. In this way the orientation of each stack and the required piping system for all different streams is crucial for the designer. The stack manifold shown in Figure 4-1 have been proposed in several patents like references [30][31].
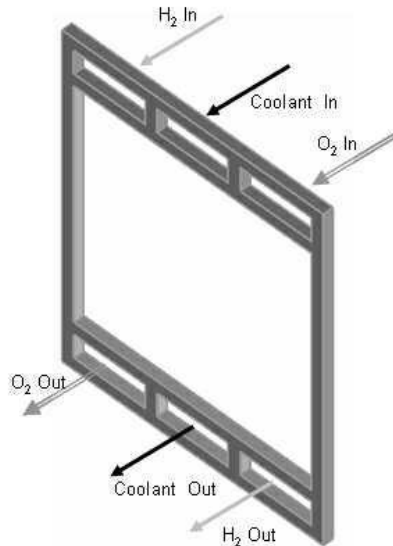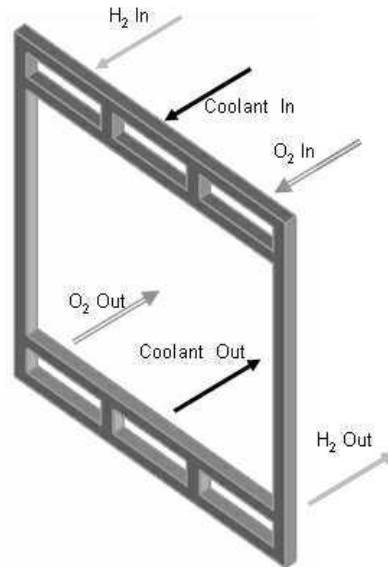

Figure 4-1 : Z-type stack configuration

Figure 4-2: U-type stack configuration

Depending upon the design of the manifold in a stack various possibilities exist for the positioning of the inlet and the outlet ports of the reactants and coolant streams. Affect of two

particular stack-flow configurations named case-A and case-B on the local current density distribution, which is based upon the analysis of the previous chapter is shown as follows:

Stack-flow configuration case-A

In this so called case-A the direction of the reactant streams are as shown in Figure 4-3 and Figure 4-4, both reactants are provided from two opposing ends.
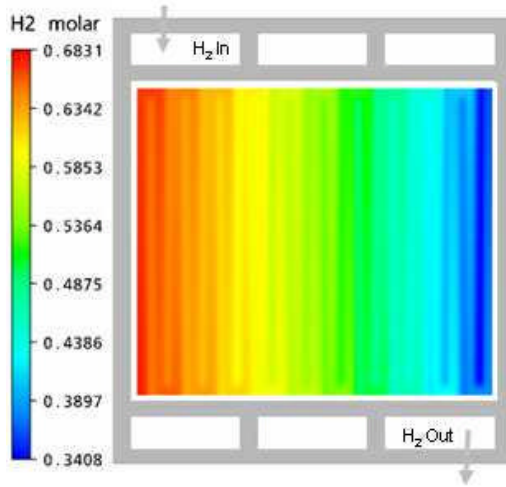

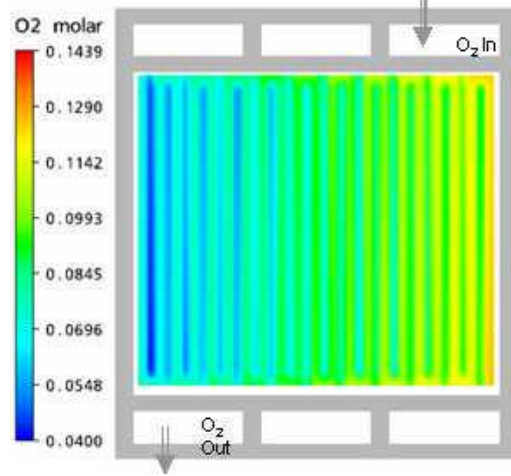**Figure 4-3 : H₂ molar concentration profile case-A**   **Figure 4-4 : O₂ molar concentration profile case-A**

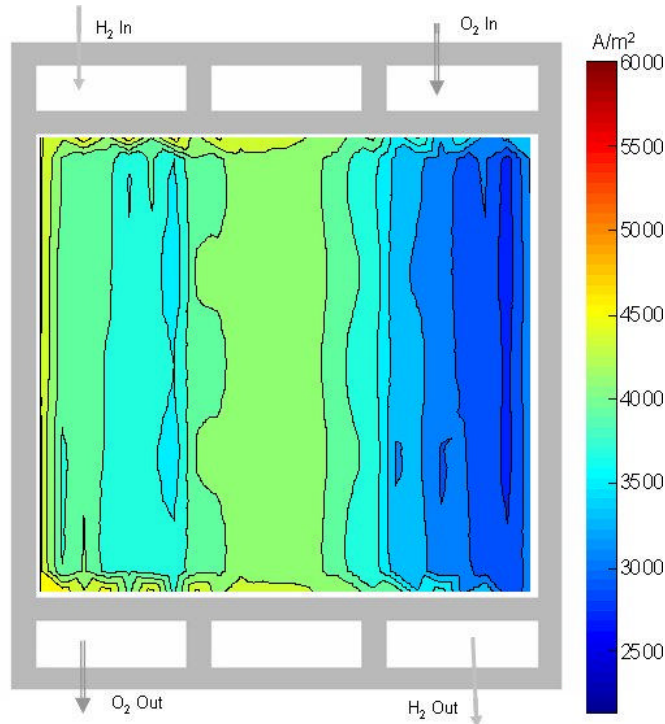The resulting distribution of local current density is shown in the Figure 4-5.

Figure 4-5: local current distribution case-A

Stack-flow configuration case-B

In the case-B, the direction of only oxygen supply is switched from the case-A inlet to outlet, i.e the inlet port becomes the outlet port and vice versa. The concentration profiles of reactants for case-B are depicted in Figure 4-6 and Figure 4-7.
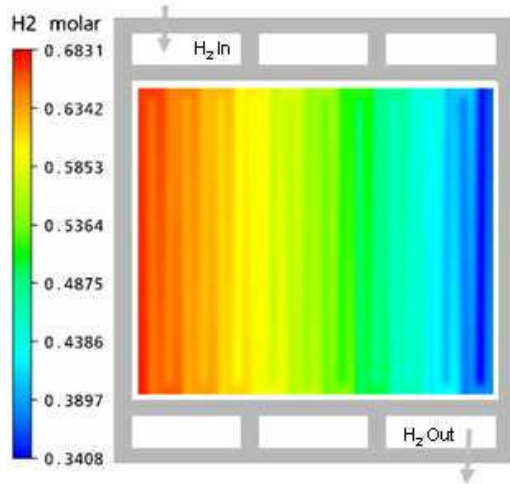

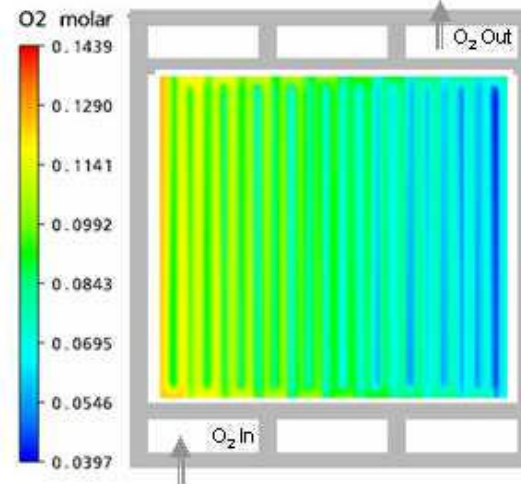**Figure 4-6: H₂ concentration profile case- B**　　　**Figure 4-7: O₂ concentration profile case-B**

In case-B, both reactants meet with higher concentrations at the inlet side, so this case should bring higher local current density as compared with case-A. This is very much evident in Figure 4-8.
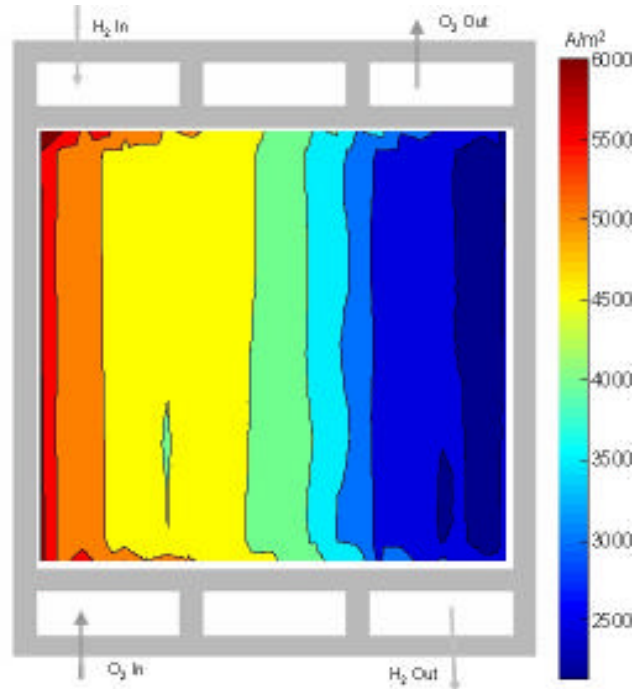

Figure 4-8 : local current distribution case-B

The local current density distribution varies as per stack-flow configuration as it is shown in the comparison of these two cases. This will then result in a variation of the heat source distribution and thus in the overall temperature distribution.

_____

4.2   Variation of properties

From the study of the detailed heat source analysis in the previous chapter we have learned that plenty of parameters are involved in the PEM fuel cell heat source distribution ranging from operating conditions to the material properties.

A gas diffusion layer (GDL) on both sides of the membrane of a PEM the fuel cell has several jobs to do. As the name suggest the first task is to provide the (humid) reactants at the reaction sites, second it gives the electrons a conducting passage, third it has to carry the product water out from the reaction site at the cathode. The porosity and permeability of GDL are the important parameters in the operation of PEM fuel cell. A fair amount of research in GDL and the so called micro porous layer (MPL) is underway; the references [32][33][34] give some idea of the current research in this area. Figure 4-9 shows the effect of porosity on the local current density distribution at a fixed permeability of 1×10^{-12} m^2 when the porosity ε is changed from 0.4 to 0.6. This is the commonly used range in a fuel cell. The results do not show any marked difference in the distribution of the local current density for three different values of the porosity.
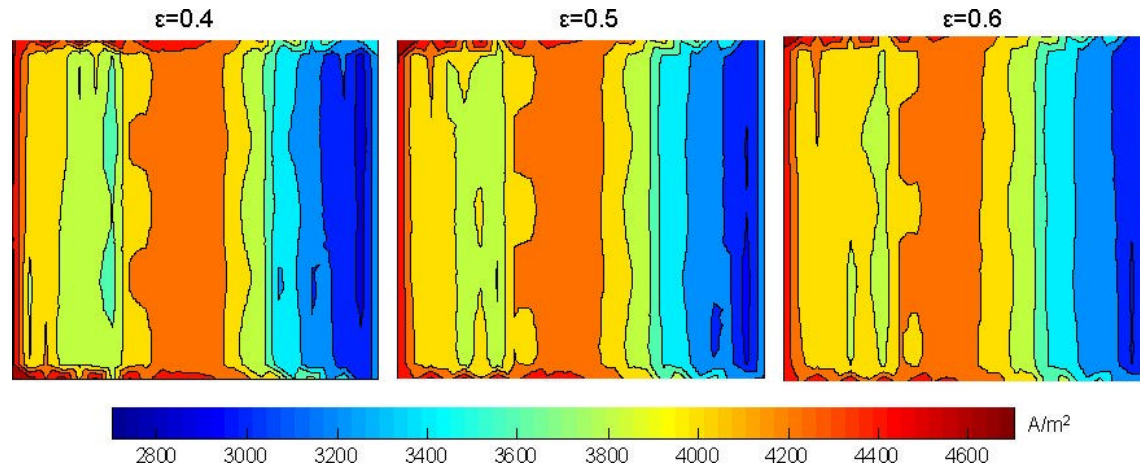

Figure 4-9 : Effect of porosity on local current density (A/m^2) distribution with case-A

This analysis is made with a stack configuration depicted as the case-A in the previous section. In a similar way as the local current density distribution is investigated by changing the porosity, one can change other parameters like permeability, diffusivity, thickness of GDL etc. In a PEM fuel cell there are numerous parameters involved in the physics of the problem, but the parametric analysis has a limitation, that at a time only one parameter can be changed while keeping the rest of the parameters fixed. There is only little information one can conclude from such an analysis because of the interaction associated among different parameters.

4.3   Sensitivity of heat source in a 50-cell solid stack

As mentioned before there is an uncertainty on behalf of the distribution of the reaction entropy between anode and cathode. The aim of this subchapter is to test the sensitivity of this distribution. for this reason as a first step from a single cell towards a whole FC stack a 50 cell solid stack is formed by incorporating the thermal conductivity of the membranes, gas diffusion layers and bipolar-plates. A uniform heat source is employed at the interface of the GDL and the membrane at both anode and cathode side, whereas a heat sink is applied for the coolant, a schematic is shown in Figure 4-10. For convenience a quarter portion is simulated only using a symmetry boundary condition as shown in Figure 4-11.
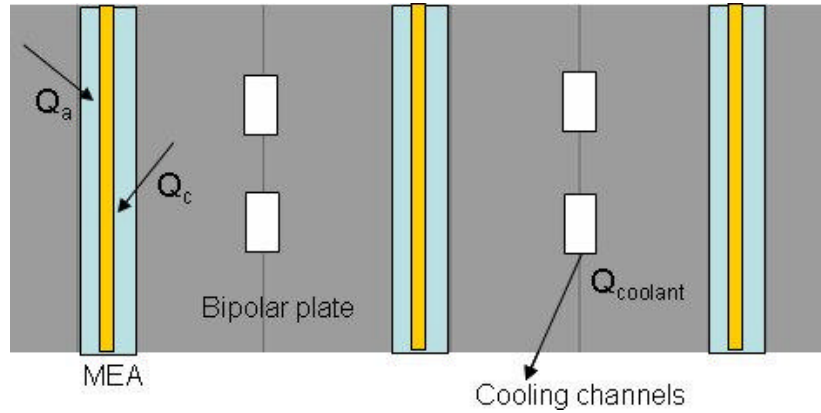

Figure 4-10 : Part of the cross-section of the 50 cell solid stack

The parameters used in this 50-cell solid stack model are shown in Table 4-1. A convective boundary condition is used at the outer walls of the stack. The sensitivity on behalf of the heat source at the electrode is investigated by changing the magnitude of heat source by 100 W/m^2 at both electrodes.

Table 4-1 : Parameters used in 50 cell solid stack

Thermal conductivity of the membrane (W/mK)	0.3
Thermal conductivity of the GDL (W/mK)	1.25
Thermal conductivity of the bipolar plate (W/mK)	15
Heat source (W/m^2)	2000
Heat sink (W/m^2)	1910

The resulting temperature distribution along the length of the stack is shown in Figure 4-12, Figure 4-13 Figure 4-14.
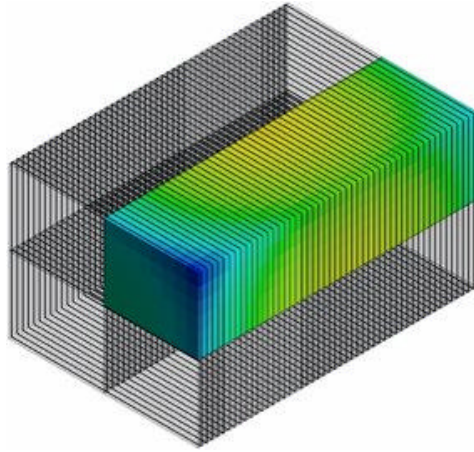
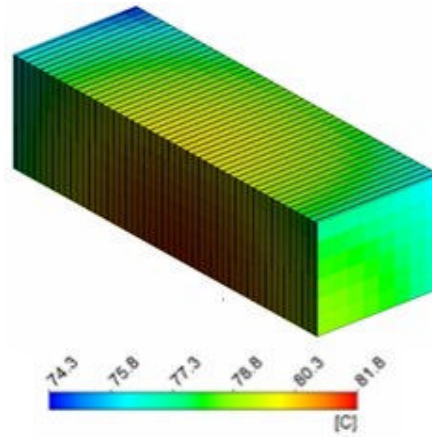**Figure 4-11: Quartet portion of 50 cell solid stack**

Figure 4-12: Temperature distribution of 50 cell stack at Qa=1000 Qc=1000 W/m²
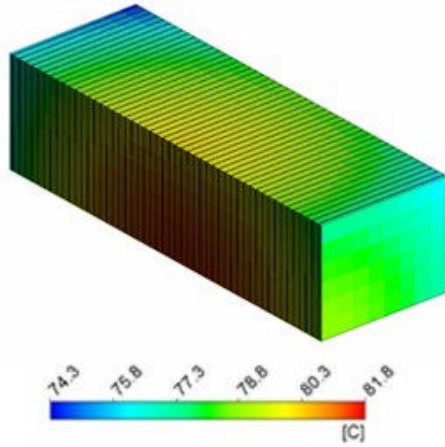
Figure 4-13: Temperature distribution of 50 cell stack at Qa=900 Qc=1100 W/m²
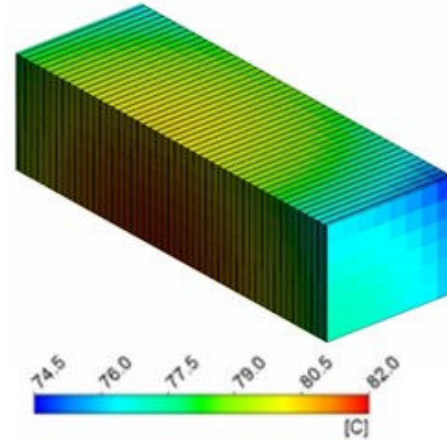
Figure 4-14 : Temperature distribution of 50 cell stack at Qa=1100 Qc=900 W/m²

A comparison of the sensitivity of the heat generation at different electrodes in the above three cases is shown in Figure 4-15, for clarity this graph is drawn by smoothing the fluctuation of temperature across the MEA of the cell. This emphasizes the understanding of heat generation at an individual electrode as important in developing a realistic temperature distribution of the stack.

Figure 4-15 : Temperature distribution in a 50 cell solid stack at three different sets of fluxes at cathode

_____

5   CFD Basics and benchmarking

Computational Fluid Dynamics (CFD) is rapidly growing as a powerful tool in industry and academics for solving problems in wide areas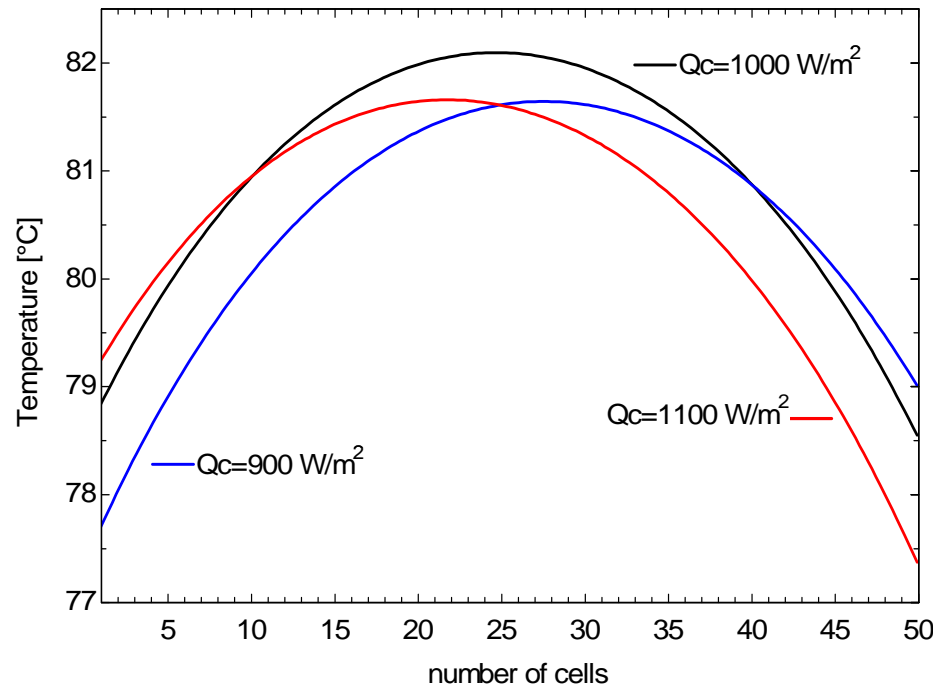 of science and engineering, but still its effectiveness and credibility lies in the correct modeling of the physics concerned and its validation. Because of several limitations the experimental side is not growing with the same pace as the numerical side. This brings more question marks in researcher's mind, so there is a need to improve the credibility of the numerical work. One way is to solve first some benchmark problems, whose results are well known, then work on real problems with more confidence. This chapter introduces briefly the CFD with a user oriented approach and then presented the result of two benchmark cases, one for laminar flow in pipe with heat transfer and other for turbulent flow regime.

5.1   CFD Basics

Computational fluid dynamics (CFD) is a computer-based design and analysis tool used to solve the set of coupled, non-linear, partial differential equations arising from fluid flow, heat transfer and other physical processes over a region of interest (domain) under specified conditions (boundary conditions). Many-fold increase in computational ability has given birth to this new discipline of CFD among the traditional theoretical and experimental studies, which of course complementary to each other in many ways. The symbiotic relationship is shown in Figure 5-1
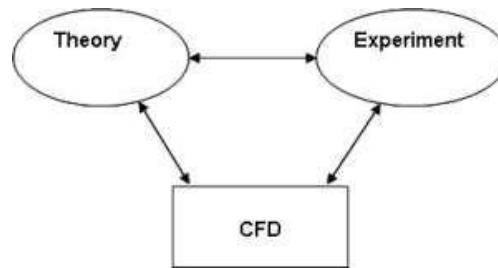

Figure 5-1 : Symbiotic relationship among theory, experiment and CFD

5.2   Stages in CFD

After the conceptualization of the problem, broadly speaking from the user point of view there are five stages in CFD simulation. First is to build the geometry, second is the meshing, third is to apply the physics of the problem, fourth is the numerical solution of the problem, and fifth is the post processing of the numerical result. Every stage has its own tidbits, the following subsections briefly describe these stages.

5.2.1 Building Geometry

Geometry is usually build through primitives (geometrical building blocks) e.g points, lines and surfaces and then using geometrical transformations like translation, reflection, rotation, and scaling to get the required geometry. In commercial CFD softwares there is a flexibility of importing geometries from several different CAD programs. User must be careful in CAD modeling for geometrical entities regarding consistent topology (neighborhood information of geometrical entities), following rules for example given in [20] is useful.

Vertices must be defined on both ends of an edge.

_____

More than two edges are to be run into a vertex.

A face must be bounded by a closed chain of edges.

An edge must be connected to two faces.

A consistent topology is very important in geometry building process because the connectivity in geometry can affect the blocking process in subsequent mesh building, especially for a block structured mesh, and finally would affect the quality of numerical results.

5.2.2 Mesh Generation

The mesh or grid generation is usually the most time consuming step in a CFD simulation, especially in the beginning because of the complexity of meshing algorithms. Meshing is a process of sub-dividing the computational domain into a number of smaller, non-overlapping regions known as cells or control volumes. The reliability and accuracy of the simulation results largely depends upon the mesh type and its quality. Several different meshing algorithms have been developed, their broad classification is depicted in Figure 5-2 [21]. Some CFD solvers have serious limitations for accepting the mesh on the basis of quality, for example the mesh must not have a very high aspect ratio etc.

A structured and unstructured mesh distinguishes how the cells or elements meet. Structured mesh have a regular arrangement of its cells that can be defined by specifying the parameters (number of nodes over an edge, its growth ratio etc) of the arrangement. Each cell is not defined separately, internal nodes are always attached to same number of elements. It requires a geometry to conform to specific characteristics, and regular pattern of polyhedrons formed based on characteristics of the geometry. Typically the structured mesh is easier to compute, but sometimes they have more elements with a bad aspect ratio. Example of the structured mesh is shown in Figure 5-3.

Unstructured meshes have no regular arrangement of its cells; each cell has its own connections to the adjacent cells, so it can be defined separately. Each cell has its own set of vertices with positions determined by the topological shape of the cell and its order. A connection between cells is deduced if cells have common vertices. No specific requirements are needed for a geometry, polyhedrons are placed using particular mesh algorithm (e.g Delaunay triangulation algorithm) so that all the mesh elements conform to the shape of the geometry. An advantage of unstructured mesh is its auto computation and the flexibility to choose finer or coarser mesh elements by choosing the maximum size of the element.
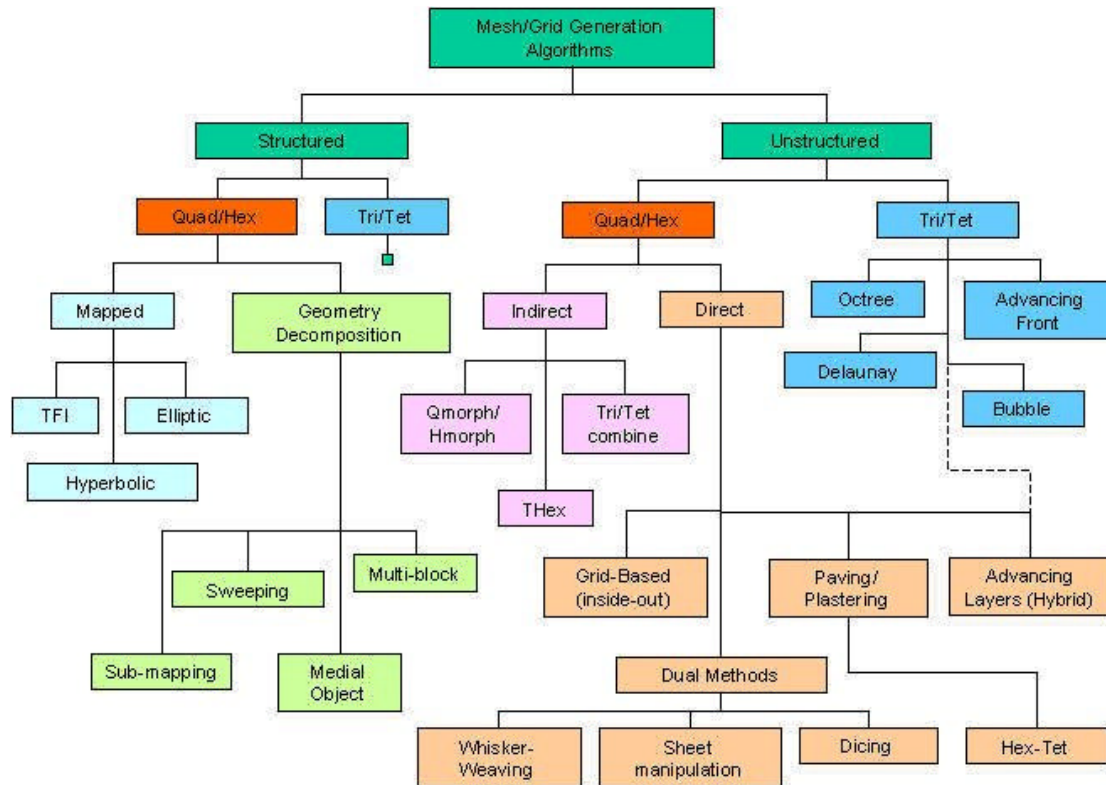
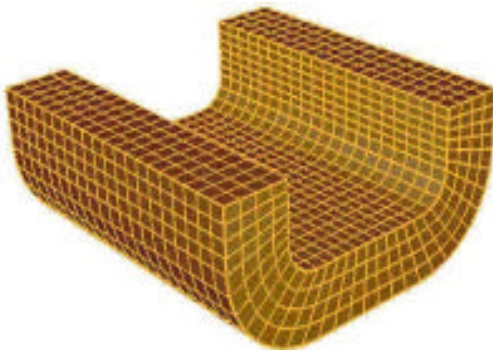**Figure 5-2 : Mesh generation algorithms, image courtesy reference [21]**

Figure 5-3 : Structured mesh, Ref [21]
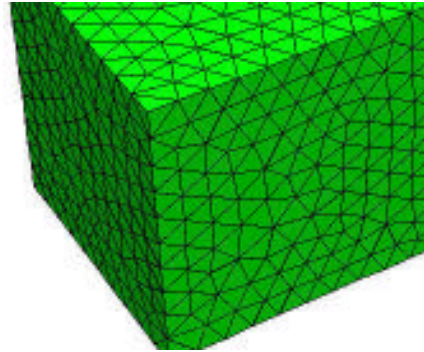
Figure 5-4 : Unstructured mesh

5.2.3 Applying Physics and Boundary conditions

After the pain-staking work of mesh generation, the next step is applying the physics of the problem and the boundary conditions; this is an actual model building process. As a first step domains are defined like fluid, solid or porous domain with appropriate physical models based on the assumptions chosen for the said simulation (steady state/transient, stationary/rotating domain, laminar/turbulent flow, buoyant/non-buoyant, isothermal/heat transfer etc). In case of multi domain, the domain interfaces need to be created as well. The next step is to apply the proper boundary conditions (symmetry, inlet, outlet, wall boundary condition etc). State of the art CFD simulation programs are quite smart and robust when user inadvertently apply the unphysical condition; they always prompt the user to check the physics. CFD is no exception

_____

as for as GIGO (Garbage in Garbage out) principle is concerned. User must be crystal clear about the assumptions and the underlying limitations incorporated in the CFD model, otherwise one can get some colorful pictures, but of no use. Modeling errors are the most critical, because they cannot be reduced systematically unlike some numerical errors. This stage is the heart (device pumping blood to all organs) of the CFD modeling; great care is required in applying the physics to the problem concerned, the model must be close to the reality under given constraints as much as possible in order to get some useful pictures.

5.2.4 Numerical solution

After developing the numerical model the next step is to solve this model, usually this step is a black box for most of the users except specifying the discretization scheme (Upwind, Higher order Resolution etc), convergence criteria, residuals level, precision level etc. Modern day solvers has the capability to visualize the convergence of governing equations as well as the monitoring of the specified variable during the iteration process, this can be very important when some abrupt changes occurs during the simulation. The domain imbalances (like mass balance, energy balance etc) can also be monitored. There are several types of numerical errors exist, like discretization error in space and time (comes while converting differential or integral formulation into algebraic expression), iteration error (implicit formulation require iterative process, which lead to residuals), and round-off error (solver solves the equation with finite number of digits e.g. 8 digits for single precision, and 16 digits for double precision). For a good quality CFD solution, these errors can be minimized systematically by taking higher order discretization schemes, lowering the convergence criteria, double precision etc, but these measures require obviously more computing efforts, so from practical point of view there is always a trade-off between accuracy and cost.

5.2.5 Post processing

This is the stage where user can see the outcome of the simulation. The results can be seen in the form of contours, vector plots, graphs, animations etc for given variable or set of variables. Most of the commercial CFD programs have wide range of post processing capabilities; some are specific to particular applications like, turbo machinery, aerodynamics etc. In the post processing stage first thing one must check is the boundary condition of the simulation, then one can see other relevant variables.

5.3 Concluding remarks for CFD

One must keep in mind that the models are the approximation for real world situation, so there is no perfect model exist, the usefulness of the model lies in the underlying assumptions over which the model is based upon. Great care is required in the interpretation of the CFD results especially when extrapolating the results. As discussed previously the results are very much mesh dependent, therefore the grid independence study is inevitable. Since CFD is developing very fast, the versions of the commercial codes are getting better day by day, enhancing the old functionality and incorporating new methodologies, the user must need to update oneself. Several good introductory books are available in CFD [27], [28],[29] , but real learning lies in doing.

5.4 Benchmarking

Predictions of the friction factor and the heat transfer coefficient are the most central questions which need to be answered inevitably by an engineer involved in the design of a thermo-fluid problem. These parameters are critically important for any effective thermal design. The friction factor is responsible for calculating the required pumping power, whereas the thermal resistance against heat transfer is quantified through the heat transfer coefficient. In a PEM Fuel cell stack the gaseous reactant flow in the channels and the liquid flow in the cooling channels are both wall bounded internal flows, so for benchmarking pipe flow case is chosen. Following are the two benchmark problems investigated and compared with available results for validation of the CFD work. Another part in validation will be the experiment presented in section 6.2.2 of this thesis.

Problem 1: Investigation of heat transfer and pressure drop in a tube for laminar flow with constant heat flux and constant temperature conditions using ANSYSCFX11.0

Liquid or gas flow through pipes or ducts is commonly used in heating and cooling applications, fluid is forced through pump or fan, the amount of heat transfer is directly related with the convection heat transfer coefficient (h) and pressure drop to the friction coefficient (f). Not many industrial pipe flows are laminar, but laminar heating and cooling does occur in an increasing variety of modern equipments and instruments like MEMS, laser coolant lines, and many compact heat exchangers [22].
An axisymmetric pipe of diameter 25 mm and length 3m is chosen, since we are going to investigate the heat transfer and pressure drop in a pipe for a **laminar flow** which means that there is no swirl anticipated in the flow, an axisymmetric 2D mesh would be quite reasonable.
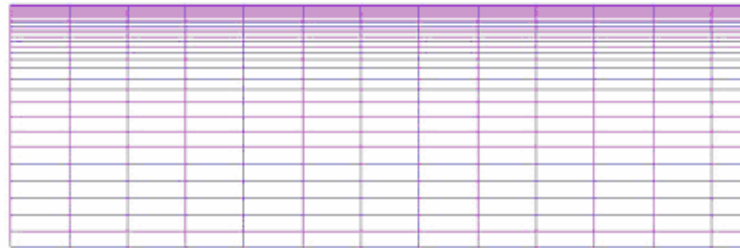

Figure 5-5 : A part of the view for the mesh used in the simulation

Mesh information: Number of Nodes: 62000, Number of Elements (Hexahedra): 29970 Along the radial direction there are 31 nodes distributed exponentially which means more dense close to the wall as compared to the centre, whereas along the length there are 1000 nodes.

Physics and Boundary conditions:

Fluid: Water (constant property liquid)
Inlet: Normal velocity of 0.00714 m/s.
Outlet: Static Pressure 1.01 bar
Wall: Heated wall (constant heat flux /constant temperature), with no slip condition.
Flow: Subsonic and Laminar (Re = 200)
Heat Transfer: Thermal energy model without viscous dissipation

Results: Identical curves have been obtained at constant heat flux of 2000, 4000, 8000 W/m^2. The same is true in case of constant temperature boundary condition at the temperatures of 50,

_____

100, and 150 °C. Figure 5-6 shows that after 2m the Nusselt number approaches the limiting values as proved through analytical results in [23]. Heat transfer coefficient is calculated using equation (5.1).

$$h = \frac{q}{T_w - T_b} \qquad (5.1)$$

where q is the wall heat flux in W/m^2, T_w is the wall temperature and T_b is the bulk temperature defined as

$$T_b = \frac{\iint_A \rho c_p u T dA}{\rho c_p UA} \qquad (5.2)$$

where u is the local velocity and U is the average velocity. Since the properties of the fluid are taken as constant we calculated the bulk temperatures using the mass-flow-average function in CFX at a cross section, which is defined as

$$massFlowAve(T) = \frac{\sum \dot{m}T}{\sum \dot{m}} \qquad (5.3)$$

where $\dot{m}$ is the mass flow rate. In order to calculate the pressure drop along the length of the

$$\Delta P = 4f \frac{L}{D}\left(\frac{1}{2}\rho U^2\right) \qquad (5.4)$$

pipe from equation (5.4), the friction factor is required, which can be evaluated from the relationship of shear stress and friction factor as given by equation (5.5). The value of the wall

$$f = \left(\frac{\tau_w}{\frac{1}{2}\rho U^2}\right) \qquad (5.5)$$

shear stress τ_w can be read from the result of the simulation as shown in Figure 5-6, whose value become constant after 0.3m of the length of the pipe, the value is 2.034×10^{-3} Pa. By substituting the values of wall shear stress and average velocity corresponding to Reynolds number of 200 we get the value for the friction factor $f=8.004 \times 10^{-2}$. This result can be verified from the Hagen-Poiseuille solution for friction factor $f = 16/Re$ i.e 16/200 is 0.08.
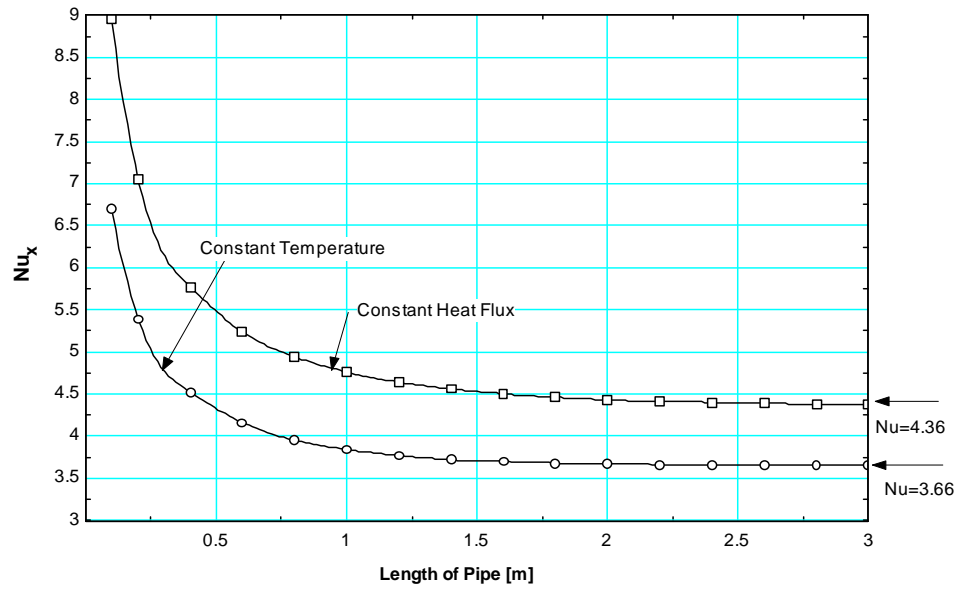
Figure 5-6 : Nux along the length of the pipe for constant Temperature and Flux conditions
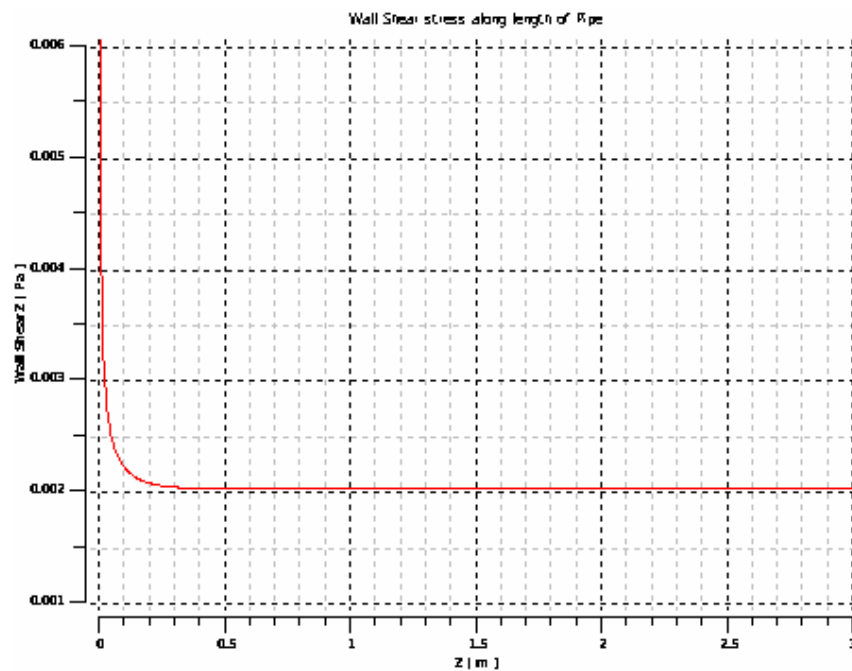
Figure 5-7 : Variation of wall shear stress along the length of the pipe

This shows that the pressure drop predicted by the simulation is quite consistent with the theoretical result. This wall shear stress becomes constant also signifies that the after 0.3 m the flow has become fully hydrodynamically developed which is almost consistent with the approximate formula provided in [24] $L_{h,laminar} \cong 0.05$ Re D.

Grid Independence: No difference in the result has been found after running a simulation over a refined mesh by a factor of over 3.2 having Number of Nodes: 204000 and Number of Elements: 99950

_____

Problem 2: Numerical prediction of the local Nusselt number and friction factor in a circular pipe under fully developed turbulent condition.

An axisymmetric smooth circular pipe of diameter 10 mm and length 450 mm is chosen, this length is good enough for the flow to become fully developed, as we know for turbulent flows, the entrance length (hydrodynamic and thermal) is about 10D [23]. Unlike laminar flows, the numerical prediction of turbulent flows require more efforts, a complete solution of velocity and temperature field considering all length and time scales involved in turbulent flow is a subject of DNS, it requires immense computational efforts even for simple geometries, for practical flows it is not possible to capture all the scales, this has given rise to the area of turbulence modeling, where near wall treatment is made through so called wall functions for both velocity and temperature field. The numerical solution is made by dividing the domain into small control volumes, where conservation equations are solved so that the fluxes are balanced at the surface nodes as shown by black dots in Figure 5-8. The missing fluxes at the wall are supplied through boundary condition as shown in Figure 5-9.
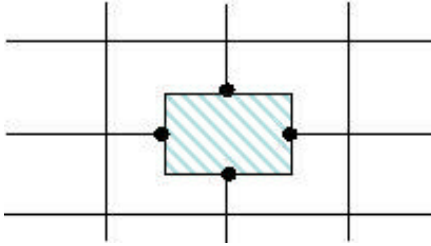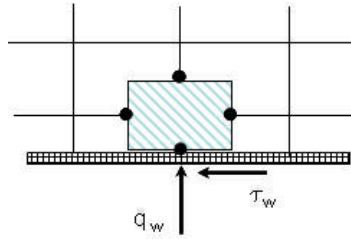

Figure 5-8 : Control volume

Figure 5-9 : Control volume near the wall

Mesh information: The meshing for turbulent flow is not straightforward because of wall function approach used in turbulence models, in this study the y^+ is taken less than 1 for Reynolds Number 4,000 and 10,000, whereas y^+ less than 1.3 is used for Reynolds Number 25,000 and 50,000. A y^+ is a dimensionless parameter like local Reynolds number which determines the relative importance of viscous and turbulent processes. In wall bounded flows the innermost region known as viscous sub-layer, the molecular viscosity plays a dominant role in momentum and heat transfer whereas in the outer layer known as fully turbulent layer, the turbulence plays a major rule. At the wall when $y^+=0$ the viscous contribution is 100%, at $y^+=12$ the viscous contribution drops to 50%, while at $y^+=50$ the viscous contribution is only less than 10%. For more detail interested readers may consult reference [84], a very nice text on turbulence. At the wall, viscosity (υ) and wall shear stress (τ_w) are important parameters. In the definition of y^+ both these parameters are present as shown in equation (5.6).

$$y^+ = \frac{y\sqrt{\tau_w/\rho}}{\upsilon}, \qquad (5.6)$$

where y is the normal distance from the wall. In making a mesh for the turbulent flows one must have to calculate the value of y^+ in priori. The number of nodes needed close to the wall usually grows exponentially as it is visible in Figure 5-10 in order to capture correctly the wall effect.

The new treatment of scalable wall-functions in k-ε based turbulence models and automatic near wall treatment in k-ω based turbulence models allow having arbitrary fine grid near the

wall. In radial direction 30, 37, 51, and 57 nodes are taken in the mesh for Reynolds number 4000, 10000, 25000, and 50000 respectively. A part of the mesh for Reynolds number 4000 is shown in the Figure 5-10.
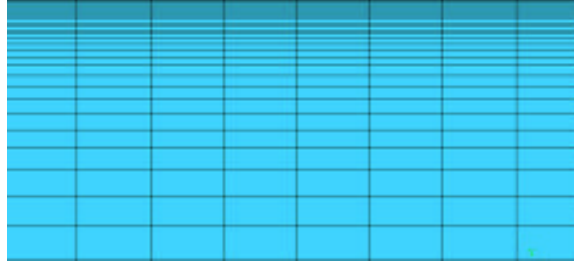

Figure 5-10 : A part of a mesh for Re=4000 showing exponential mesh distribution

Physics and Boundary conditions:

Fluid: Water (constant property liquid)
Inlet: Normal velocity corresponding to Reynolds number.
Outlet: Static Pressure 1.01 bar
Wall: Constant heat flux of 60,000 W/m^2, with no slip condition.
Flow: Subsonic and Turbulent (using k-ε, RNG k-ε and SSG RSM turbulence model)
Heat Transfer: Thermal energy model without viscous dissipation

Results: The results of the simulation are compared with correlations, for fanning friction factor the Karman-Nikuradse relation is used as in equation (5.7) , whereas for Nusselt number the Gnielinksi correlation is used as in equation (5.8).

$$\frac{1}{\sqrt{f}}=1.737\ln(\mathrm{Re}\sqrt{f})-0.396 \tag{5.7}$$

$$\mathrm{Nu}=\frac{(f/2)(\mathrm{Re}-1000)\,\mathrm{Pr}}{1+12.7(\sqrt{f/2}(\mathrm{Pr}^{2/3}-1)} \tag{5.8}$$

The result of the Nusselt number is shown in Figure 5-11, it is based upon the definition given in equation (5.7) and equation (5.8). It shows slight over prediction of Nusselt number at higher Reynolds number compared with Gnielinksi correlation, for this particular problem the second moment closure turbulence model like SSG RSM (solve six Reynolds stresses) do not show any considerable advantage over two equation models like k-ε and RNG k-ε. For fanning friction factor as shown in Figure 5-12 the case is opposite, the turbulence models are under predicting the friction factor compared with Karamn-Nikuradse relation, the prediction get improved at higher Reynolds number. In literature different temperatures like minimum temperature of the domain or near wall temperature are used in place of bulk temperature in the calculation of convective heat transfer coefficients [25] [26]. The Nusselt number calculated on the basis of near wall temperature is also shown in Figure 5-13, which slightly over predicts the Nusselt number in comparison with Gnielinksi correlation.

Figure 5-11 : Comparison of the Nusselt number for different turbulence models with Gnielinski correlation
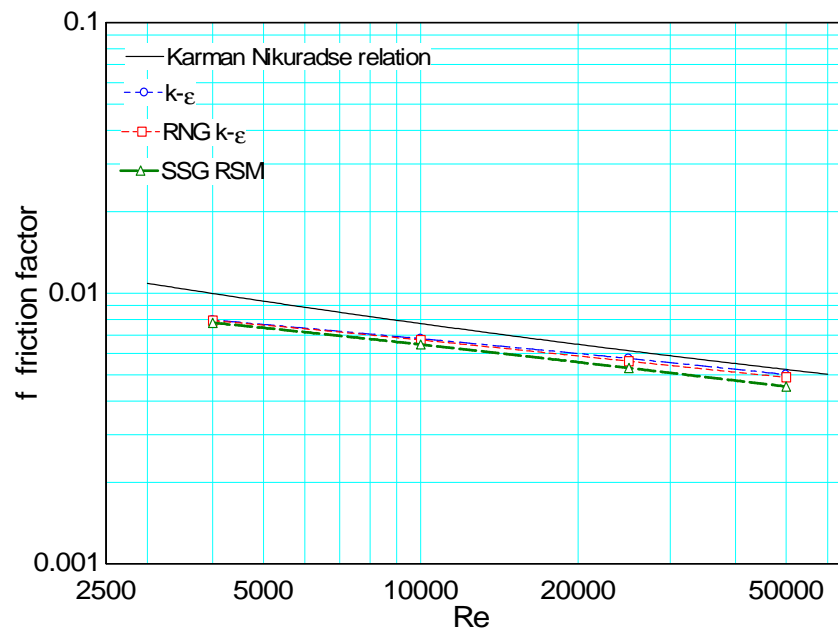
Figure 5-12 : Comparison of fanning friction factor for different turbulence models with the Karman Nikuradse relation.
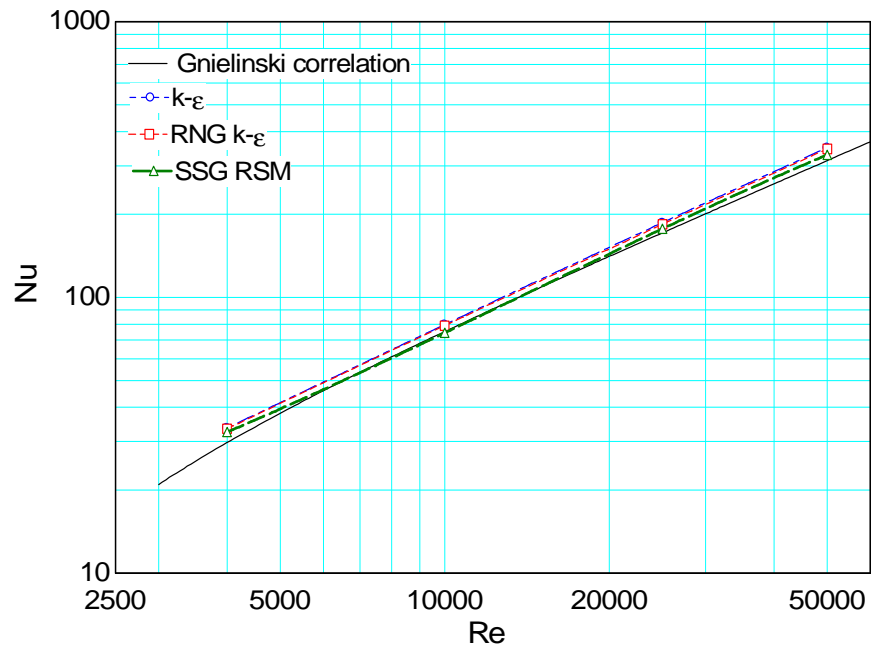
Figure 5-13 : Comparison of Nusselt number for different turbulence models with correlation using near wall temperature instead of bulk temperature

This benchmarking study gives sufficient confidence in the results of the CFX models used for the calculation of temperature fields on bipolar plates. The situation used for benchmarking were very simple ones, as only for those simple geometries analytical solutions are available. Fine and careful meshing is important especially for turbulent flow.

6 PEM fuel cell stack calculations

In the first section of this chapter different liquid channel designs for PEM fuel cell cooling have been analyzed numerically and optimized through the calculation of the total entropy generation in the cooling plate. The heat flux distribution used for these simulations is derived from the detailed analysis of the loss mechanism in chapter 1. The temperature distributions are shown and results of the important parameters are tabulated. In the second section the temperature distribution of a four cell stack is modeled through CFD, the results are validated through experiment by using an in-house developed four cell stack. In the third section the temperature distribution of a commercial size stack of 30 cells is shown with different number of cooling plates used within the stack.

6.1 Flow field optimization of liquid cooling channels

Different flow field designs in three-dimensions are investigated with a conjugate heat transfer condition at steady-state using the commercial CFD code ANSYS CFX11.0. One of the serpentine cooling channel geometries as enclosed in the solid block is shown in Figure 6-1. The heat flux boundary condition is imposed on the front and the back walls of the block, the walls in periphery of the solid block are assumed adiabatic. Water as a coolant is supplied with a given mass flow rate, whereas a static pressure boundary condition is applied at the outlet of the channel.
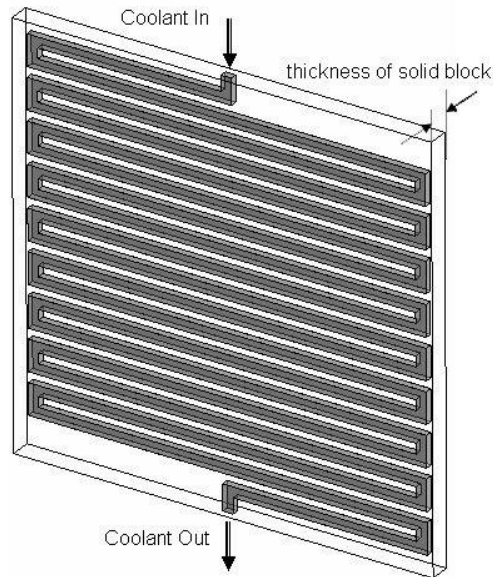
Figure 6-1 : Cooling channel (serpentine type) enclosed in a solid block

Heat transfer and pressure drop are the two important design factors for any heat transfer device. In the design of our cooling channels, since the thickness of the cooling plate is small, the cross-section is made rectangular. The rectangular cross-sections are much easier to create from manufacturing point of view. From the heat transfer point of view, in case of laminar and fully developed flow, higher aspect ratios of the rectangular cross-section gives higher Nusselt number, of course with a penalty of higher friction factor as it is shown in Figure 6-2. Here Nusselt number and friction factor are plotted to the reciprocal of the aspect ratio. The equations in this plot are taken from Shah and London [42].

_____

In this study of different cooling channel designs the criteria for optimization is based on the entropy generation minimization. According to second law of thermodynamics, in all real systems the entropy generation due to inherent irreversibilities is always a positive quantity. So in practice we cannot get rid of the entropy generation, but what we can do is to minimize the rate of entropy generation. Therefore in this study of cooling channel designs, a criterion for optimization used is the minimization of entropy generation. Since the fluid is flowing in the cooling channel and the heat is transferred from the walls of the channel this becomes a convective heat transfer problem. In such problems the local entropy generation is due to two effects, the first being the heat transfer across a finite temperature difference and the second being the fluid friction due to viscosity. Both effects are accounted in the formula for entropy generation as taken from Bejan [43]. Equation (6.1) is derived by considering a differential fluid element as an open thermodynamic system subjected to mass fluxes, energy transfer, and entropy transfer. The entropy generation term is introduced by applying the second law of thermodynamics to the fluid element as an open thermodynamic system. The derivation is given in Appendix-C.
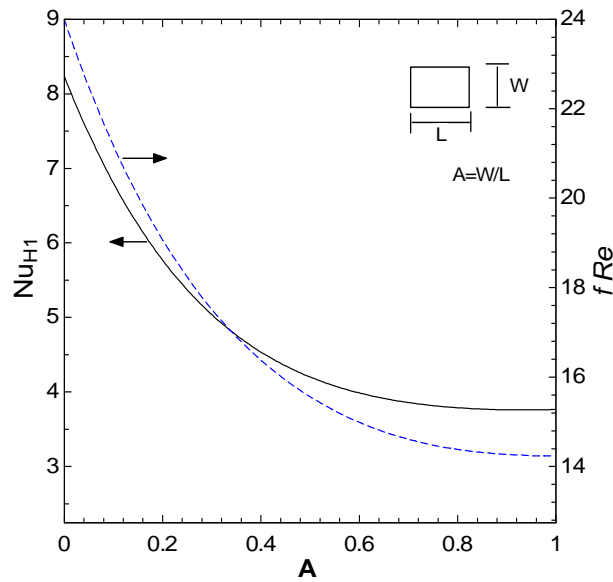
Figure 6-2 : Nusselt number and friction factor plot of rectangular cross-section to the reciprocal of aspect ratio (A) under laminar flow, fully developed and uniform heat flux condition.

In equation (6.1) the rate of entropy generation per unit fluid volume $\dot{S}_{gen}'''$ [W/m^3 K] is positive and finite as long as the temperature and velocity gradients exist. The term with curly bracket accounts for fluid friction whereas the first term is for finite heat transfer. A dimensionless parameter known as Bejan number (Be) is defined as the ratio of entropy generation due to heat transfer compared with total entropy generation. When Be is close to 1, this signify that the heat transfer irreversibility is dominating, conversely when Be is approaching zero it shows that the irreversibility due to fluid friction is dominating.

$$\dot{S}_{gen}^{'''} = \frac{k}{T^2}\left[\left(\frac{\partial T}{\partial x}\right)^2 + \left(\frac{\partial T}{\partial y}\right)^2 + \left(\frac{\partial T}{\partial z}\right)^2\right]$$

$$+ \frac{\mu}{T}\left\{2\left[\left(\frac{\partial u}{\partial x}\right)^2 + \left(\frac{\partial v}{\partial y}\right)^2 + \left(\frac{\partial w}{\partial z}\right)^2\right]\right.$$

$$\left.+ \left(\frac{\partial u}{\partial y} + \frac{\partial v}{\partial x}\right)^2 + \left(\frac{\partial u}{\partial z} + \frac{\partial w}{\partial x}\right)^2 + \left(\frac{\partial v}{\partial z} + \frac{\partial w}{\partial y}\right)^2\right\}$$

(6.1)

In many convective heat transfer problems, the viscous dissipation term in the energy equation is routinely neglected. To verify this assumption one of the runs is made by including the viscous dissipation term in the energy equation and the result is analyzed by visualizing the Be number as shown in Figure 6-3. This figure shows that at the walls of the channel the heat transfer irreversibilites are completely dominant, whereas at the mid-plane of the channel also the heat transfer is dominant except at the corner turns of the channels and some spots in the middle. The volume average Be number in the cooling channel domain is 0.98. This justifies very much the assumption of neglecting the viscous dissipation term in the energy equation.
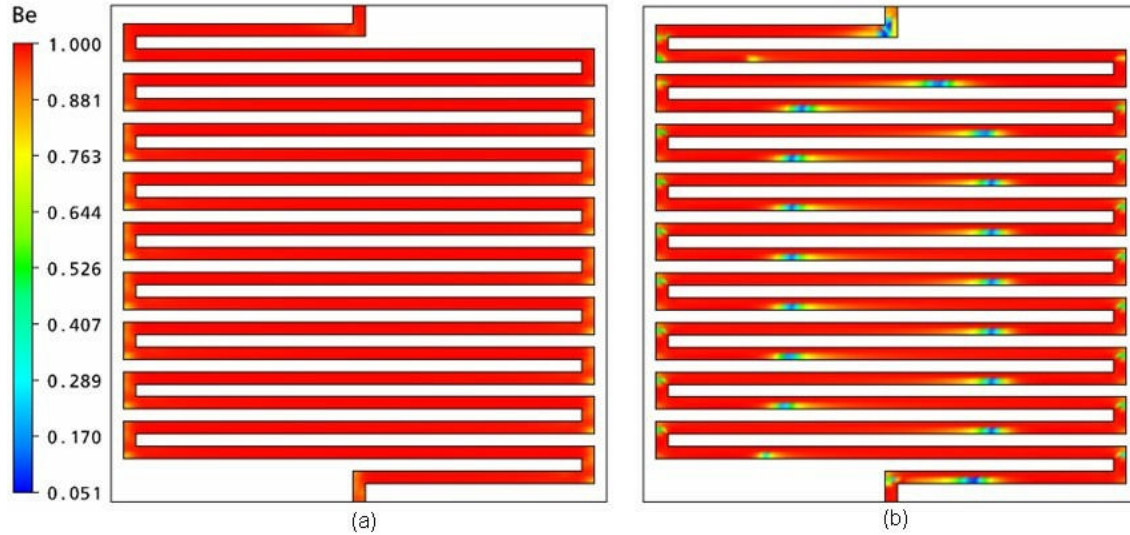
Figure 6-3 : Bejan Number (a) at the walls of the channel (b) at the mid-plane of the channel

The parameters used in this numerical simulation for different cooling channel designs are shown in Table 6-1. The cooling fluid entering into the channel is consistent with the stack configurations shown in Figure 4-1, Figure 4-2, where fluid enters from the middle of the stack manifold. Similar stack configurations are proposed in some of the recent patents [30][31].

_____

Table 6-1 : Parameters used in numerical simulation of cooling channels

parameter	value
Dimensions of solid block (cm)	$(12 \times 12 \times 0.4)$
Cooling channel cross section (mm)	(3×2)
Active area (cm^2)	144
Cooling fluid	water
Solid block thermal conductivity (W/mK)	15
Inlet fluid temperature (ºC)	50
Inlet mass flow rate at Re=500 (g/s)	0.8387
Uniform heat flux (W/m^2)	1200
Pressure (bar)	1

As concluded by Chen et al. [44], the serpentine cooling channels are better than the parallel channel designs, so in this thesis only the serpentine type design are considered, even though the pressure drop is higher in a serpentine channel compared with the parallel designs. The basic problem in the parallel design is the distribution of the cooling fluid, which is highly non-uniform as one can see in Figure 6-4. The distribution of velocity in the parallel design, consequently also the temperature distribution, is very uneven.
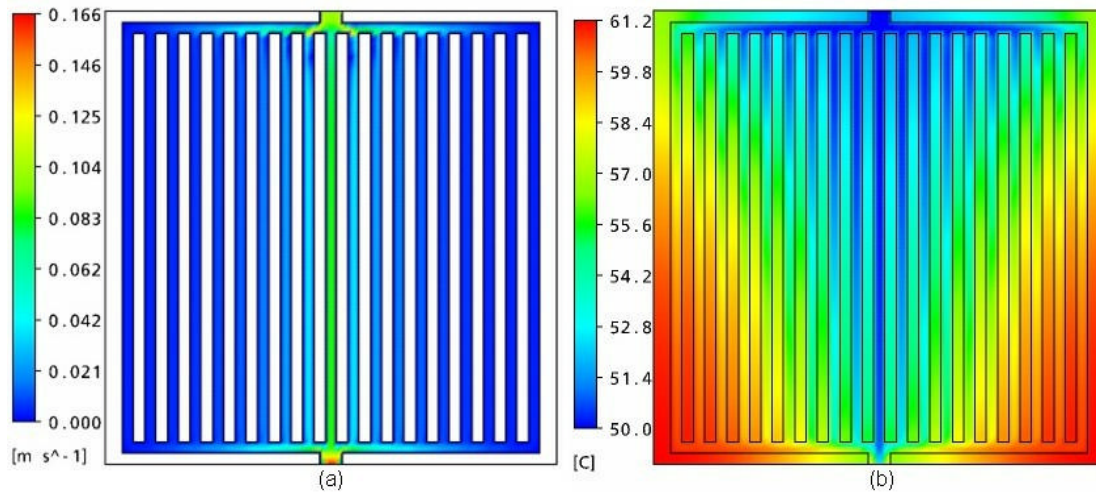
Figure 6-4: Parallel cooling channel (a) the velocity distribution (b) the temperature distribution

Several different serpentine channel designs are investigated numerically, but in the thesis only four design results are shown as examples. The designs are numbered by roman letters. The temperature distribution for these designs is shown in Figure 6-5.
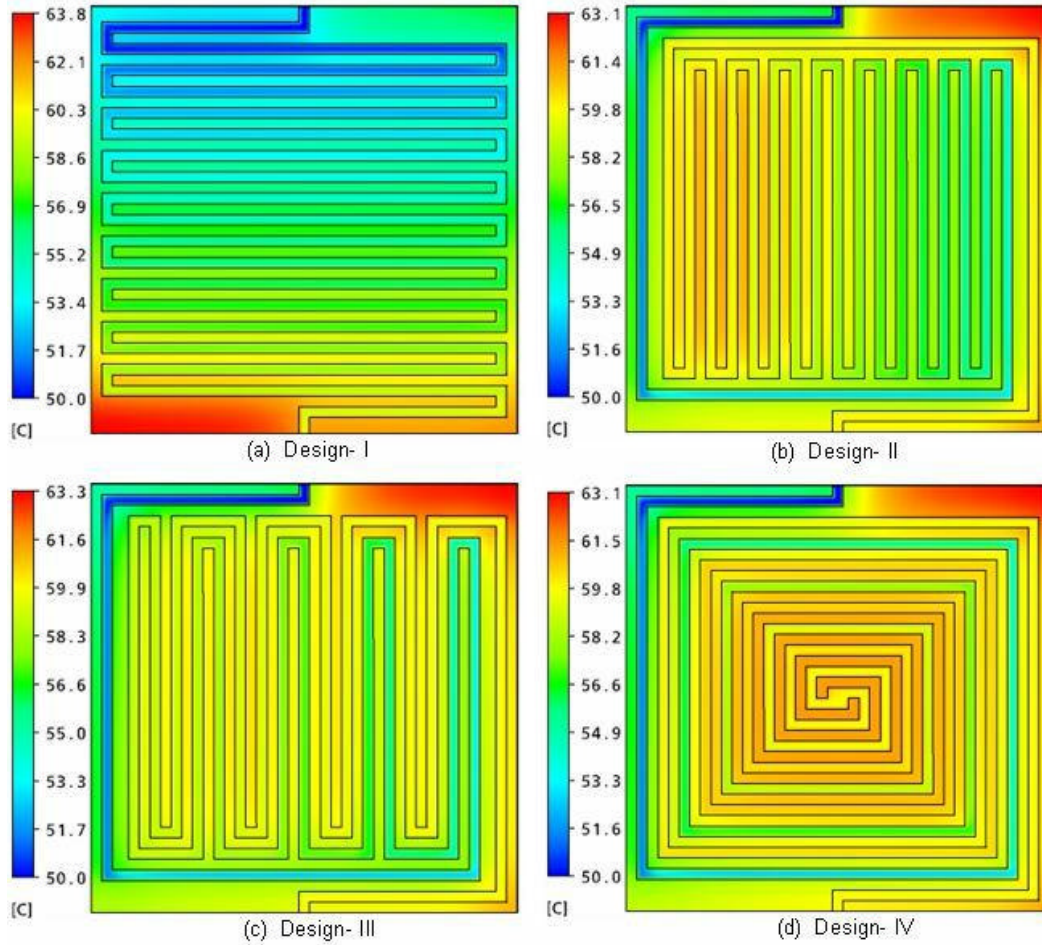
Figure 6-5 : Temperature distribution in 4 different serpentine designs

The kinetics of the electrochemical reaction of a PEM fuel cell is superior at higher temperatures, even though the reversible voltage of the cell is getting smaller at higher temperatures. A clear intention is to run the fuel cell at the maximum possible temperature without hurting the delicate membrane, this necessitate for a proper cooling design. Another important criterion is the uniformity of temperature, for the cooling channel design should also guarantee the uniformity of temperature. In reference [44] an index of uniform temperature (IUT) is introduced as defined by equation (6.2), where V is the volume over which the integral is evaluated.

$$\text{IUT} = \frac{\int\limits_V \left| T\text{-}\bar{T} \right| dV}{\int\limits_V dV}, \text{ where } \bar{T} = \frac{\int\limits_V T dV}{\int\limits_V dV} \tag{6.2}$$

The results of these four designs are given in Table 6-2, on the basis of the total entropy generation. Design-I is the best whereas on the basis of IUT the Design-III is better.

75

Table 6-2 : Results of 4 different cooling channel designs

Results	Design-I	Design-II	Design-III	Design-IV
Total entropy generation (W/m^3 K)	5.768	7.297	7.283	6.217
Be Number (volume average)	0.943	0.887	0.784	0.719
Pressure drop (Pa)	1025	1071	1100	1147
IUT (K)	2.45	1.32	1.20	1.31

The results of the simulation are assumed to be convergent when the normalized RMS residuals for all transport equations are below 1×10^{-5} and all the domain imbalances are below 0.001%. This last criterion makes sure that the mass and energy balances are met in all domains. The governing transport equations are solved using second order advection scheme with double precision. The author's experience is that in heat transfer problems the imbalances are usually met only with double precision even though this heavily increases the computational time. In any numerical CFD simulation the grid independence study is essential. In the analysis of different flow field designs for the cooling plate the grid independence study has been performed, the results are shown in Table 6-3.

Table 6-3 : Grid independence study for cooling channel

	Mesh 1	Mesh 2	Mesh 3	Mesh 4	Mesh 5
No of nodes	25440	52818	86154	121944	162672
T_{max} (K)	341.30	341.04	340.65	340.19	340.20
IUT (K)	3.876	3.386	3.387	3.386	3.386

 The target variables are T_{max}, the maximum temperature reached in both fluid and solid domain, and the index of uniform temperature. The result shows that T_{max} is the same in three significant digits when number of nodes is above 86,000, hence the Mesh 3 is chosen for all the simulations carried out in this study. The type of mesh in all mesh configurations from 1 to 5 is hexahedral. A fully structured mesh is made both for fluid and solid domains, it is observed from this grid independence study that even the coarse mesh predicts good results; this is largely because of the fully structured mesh as well as the simplified physics (laminar flow, stable boundary conditions etc). A portion of the structured hexahedral mesh for serpentine channel is shown in Figure 6-6. If the mesh elements are tetrahedral instead of hexahedral, the grid independence study can become difficult, in some case the results are oscillating.
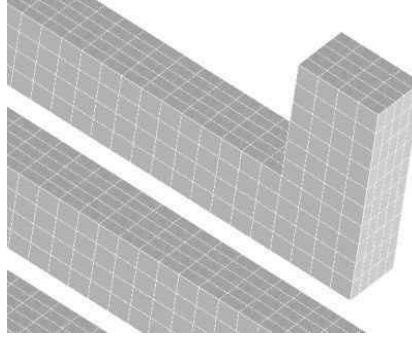
Figure 6-6 : Portion of the hexahedral mesh for cooling channel

6.1.1 Affect of aspect ratio

As discussed in section 6.1 of this thesis and evident from Figure 6-2, higher aspect ratios give higher Nusselt numbers and higher friction factors. This fact is analyzed numerically on a single serpentine channel with different aspect ratios, keeping all other parameters fixed in the simulation. The aspect ratio (AR) is changed in the simulation by keeping the width (the longer dimension) constant and changing the thickness or depth (the shorter dimension) of the cross-section. As per Figure 6-2 L is kept fixed and W is decreased in order to increase the aspect ratio. The results are shown in Table 6-4.

Table 6-4 : Results of the simulation of serpentine cooling channel for different aspect ratios.

Results	AR=1.5	AR=2	AR=3	AR=6
Total entropy generation (W/m^3 K)	3.966	7.098	13.106	29.014
Temperature (volume average- K)	330.1	329.9	329.6	329.3
Pressure drop (kPa)	1.001	2.033	5.911	41.445
IUT (K)	2.478	2.508	2.524	2.631

The temperature distribution is shown in Figure 6-7. As we have already seen in serpentine channel temperature distribution and as it is pointed out in reference [44] as well, there is a stratification of temperature from inlet to outlet in serpentine channel designs. When a cold fluid enters it gradually gains heat and its temperature gets increased as it moves along the channel length, but it is not well mixed as there is laminar flow. If we look at Figure 6-7 very closely we can see that at higher aspect ratios the cooler region from the inlet has stretched a little but at an immense expense of pressure drop and entropy production as can be seen from the results given in Table 6-4. There is only a small drop in the volume average temperature as the aspect ratio increases, but the pressure drop has increased exponentially. This is an important fact especially in the designs of micro channels. When the hydraulic diameter gets below 1mm the pressure drop per unit length shoots up enormously. This has happened in our case when AR=6, the hydraulic diameter was 0.857 mm in that case. These results give designer of the cooling channel a useful insight about the limit of increasing the aspect ratio, as it becomes clear from Table 6-4 that from the entropy production view point the higher aspect ratios don't do better.
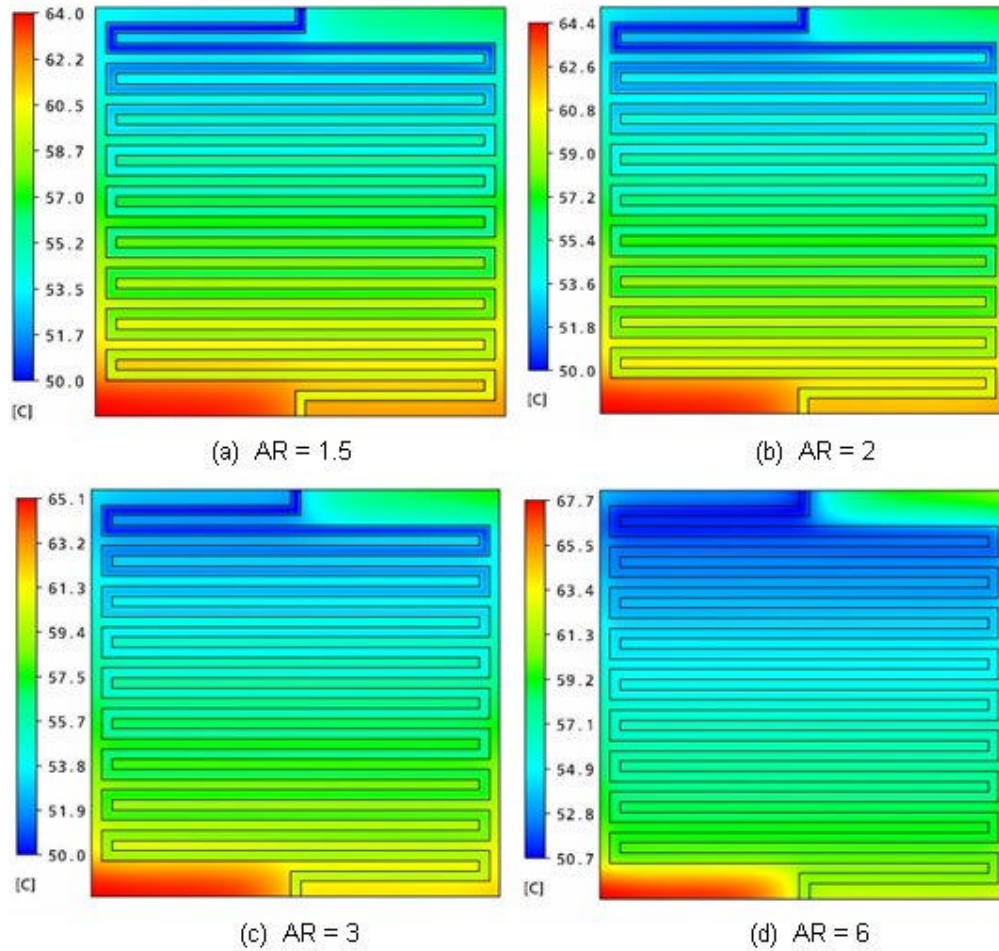
Figure 6-7: Temperature distribution of serpentine channels at different aspect ratio

6.1.2 Multiple channel designs

So far in this study a single channel is used for the cooling plate, but in commercial stacks cooling channels sometimes have multiple channels as shown in Figure 6-8. Depending upon the shape and design of the stack, there is a possibility of having multiple channel streams for the cooling plate. In this study different combination of designs with two channel streams are studied numerically, the parameters used in the simulation are the same as given in Table 6-1. The resulting temperature distribution is shown in Figure 6-9, and the results are tabulated in Table 6-5. In multiple channel design the flow rate of the coolant has been made exactly the same as used in the single channel design. This has been accomplished by allowing the cooling fluid to enter through a header in such a way that the inlet conditions of the single channel should be the same as the two channel design. For simplicity the header is not shown in Figure 6-9. At a first glance on Figure 6-9 it seems that in the two channels design the flow rate has doubled compared with the single channel design, but this is not true, as evident from the temperature range observed in both single channel and multiple channel designs, which is almost the same.
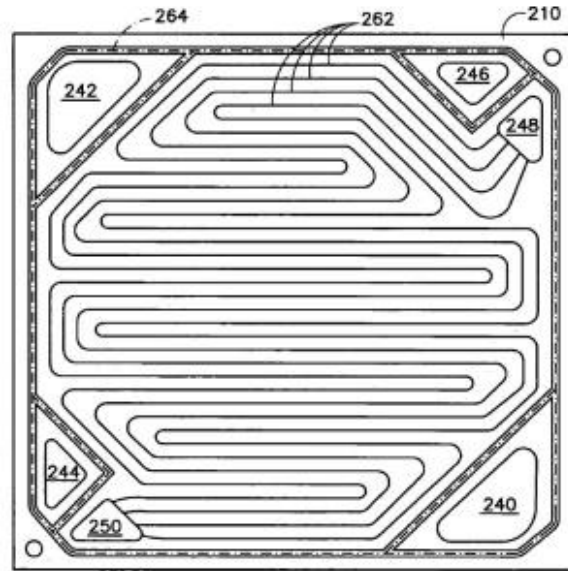
Figure 6-8 : Multiple cooling channel design (Image courtesy [65])

As we already have observed a thermal stratification in single serpentine channels, the same is true with double serpentine channel design as well. The idea behind multiple streams is to maneuver the cooling streams through different routing in such a way that one can set the intended temperature zones. For example in Figure 6-9 with Design-C both cold streams are forced to go into the centre of the cooling plate and let the outer zones relatively at higher temperature. This strategy can be useful in cooling the PEM fuel cell stack in a situation when the middle zones have higher chemical activity and thus consequently higher temperatures. The heat generated in the middle zone is difficult to dissipate compared with the outer zones where heat can be removed via outside (natural or forced) convection and radiation.

For Design-B the temperature distribution is somewhat a mirror image about one diagonal in a way that the left half of the diagonal is cooled well through cooling streams while the other half is not cooled properly having higher temperature zones. For such a situation the positioning of the stack can be made in such a way that the right half of the diagonal (hotter zone) is exposed well to some other cooling source like air-cooling. The distribution of temperature zones is very useful information for stack designers. In automotive applications from designer point of view the space is a big constraint. Only a well engineered design and positioning of the stack with proper cooling arrangement can ensure the optimized operation of the stack.

Another strategy that can be employed with cooling plates having well defined temperature zones is off-setting. For example in a stack of 30 cells having cooling plate after every third cell, the cooling plates are arranged in such a way that the temperature distribution in two adjacent cooling plates will off-set each other. The higher temperature zone of one of the cooling plate will be cancelled by the cooler zone of the next adjacent plate.
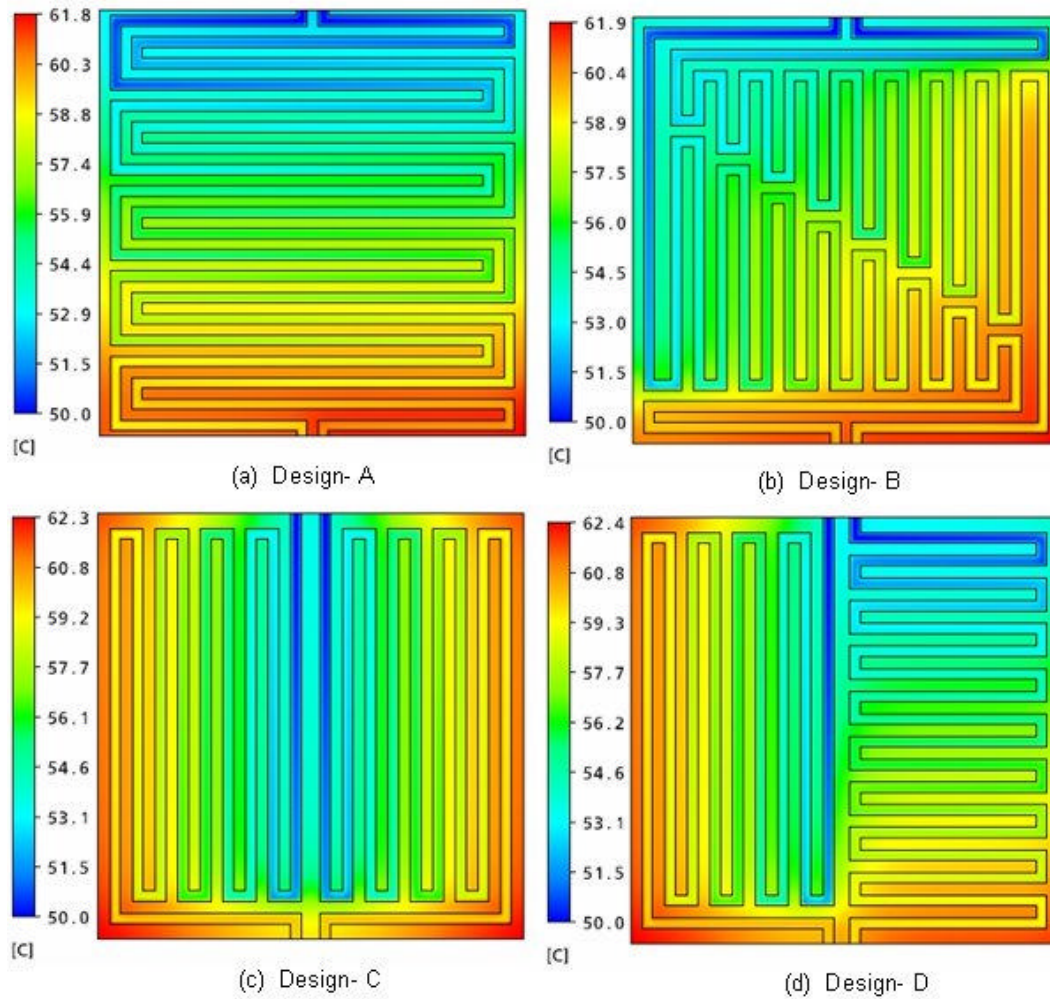
Figure 6-9 : Temperature distribution in 4 different multiple channel designs

Table 6-5: Results of the simulation of multiple cooling channels designs

Results	Design-A	Design-B	Design-C	Design-D
Total entropy generation (W/m^3 K)	4.851	4.390	8.732	6.973
Temperature (volume average- K)	329.8	330.4	330.8	330.5
Pressure drop (Pa)	252.5	253.8	220.6	232.1
IUT (K)	2.478	2.508	2.524	2.631

6.1.3 Transient analysis of a serpentine cooling plate.

PEM fuel cell stacks are intended to run at constant load under given operating condition results in almost a constant temperature of the stack, assuming that the cooling system adequately removing the heat generation. In certain cases when a load of the stack increases in a short interval by a step change, a cooling system must response to cater the heat generation

_____

by increasing the mass flow rate of the cooling fluid. In this study the heat load is increased from 1200 to 1800 W/m^2 by a step change using equation (6.3), where t is time in seconds and q (heat flux) in W/m^2 as shown in Figure 6-10. Similar to equation (6.3) has been proposed in reference [77] for dynamic load change of PEM fuel cell. The temperature response under normal cooling as given in Figure 6-10, shows that as the load increases the temperature also increases. In order to keep the temperature down the flow rate of the cooling fluid has been increased with a time lag of 5 seconds by equation (6.4), the temperature response is shown in Figure 6-10 with a legend named T-extra cooling.

$$
\begin{aligned}
q &= 1200 && \text{when } t \leq 30 \\
&= 1800\left[1 - 4e^{(-t/10)}\right] && \text{when } t > 30
\end{aligned}
\tag{6.3}
$$
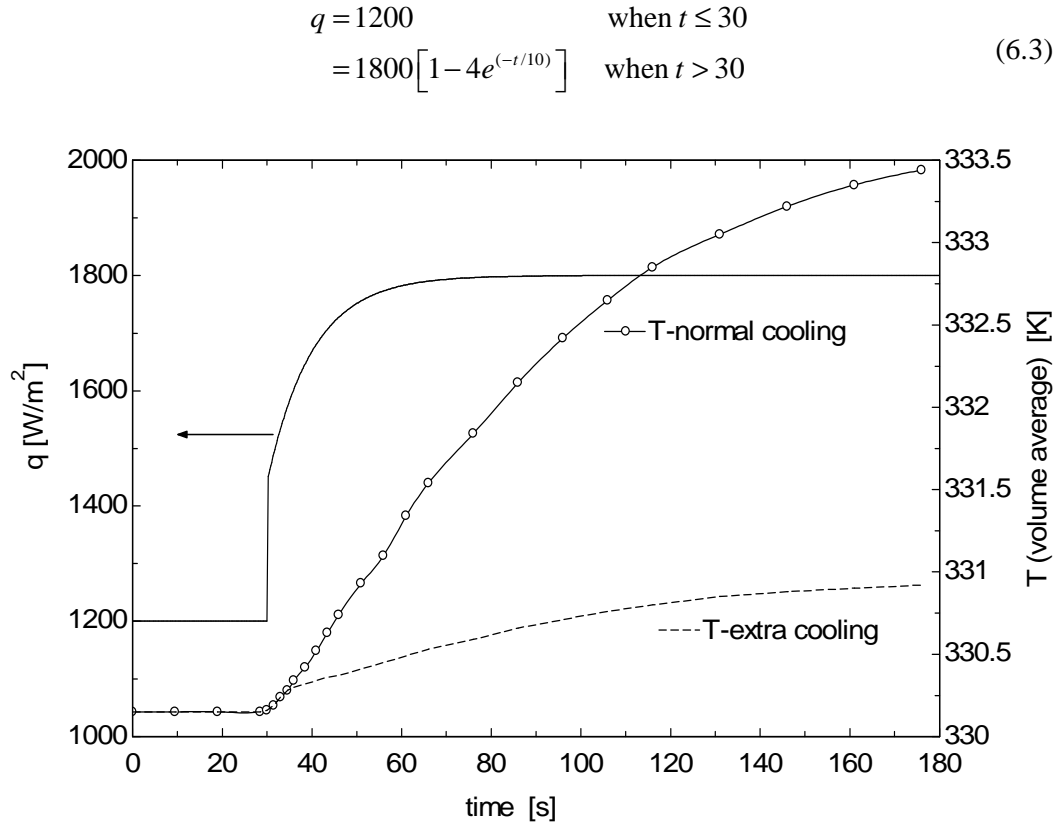
Figure 6-10 : Transient analysis of a cooling plate for a short interval

$$
\begin{aligned}
\dot{m} &= 0.8229 && \text{when } t \leq 35 \\
&= 1.2343\left[1 - 4e^{(-t/10)}\right] && \text{when } t > 35
\end{aligned}
\tag{6.4}
$$

In equation (6.4), $\dot{m}$ is the mass flow rate in g/s. The total time of the transient simulation is 176 s. This transient run is carried out on a single serpentine channel, the Design-I of Figure 6-5. The parameters used in the simulation are same as given in Table 6-1 except the heat flux and the mass flow rate.

6.2 Temperature distribution in 4 cell stack -model and experiment validation

Temperature distribution alone in a PEM fuel cell stack is an important parameter as already explained in section 1.2.1 of this thesis. The temperature distribution of the stack can portray the well-being of the stack during its operation, but its in-situ measurement is not very easy, especially close to the electrode. In this work a four cell stack is developed in-house whose bipolar-plates are made up of steel so that the heat generated in the cell can quickly transferred to the temperature probe, which is installed right in the middle of the thickness of the bipolar-plate to capture the temperature distribution. A CFD model of the 4 cells stack is also developed and the results of the simulation are validated through in-house developed stack.

6.2.1 CFD model of 4 cell stack

A single phase multi-component CFD model is developed. It consists of three different domains, reactants are supplied at anode and cathode gas channels as fluid domains, whereas the gas diffusion layer (GDL) is taken as a porous media by incorporating the Darcy model. The membrane is taken as a solid domain which is impermeable to reactant gases. Catalyst layers are modeled as interfaces between GDL and membrane. This interface is the place where sources and sinks are employed within the continuity, species transport and energy equations. The following assumptions are made in the model:

Reactant gases are ideal gases.

Flow in the gas channel is laminar.

Multi-component mixture and single phase analysis. This means that each component (H_2, O_2, H_2O, N_2) has the same velocity and temperature field.

Steady state analysis.

Activation polarization at anode is neglected.

A computational domain is shown in Figure 6-11. A Z-type of stack configuration is chosen for the analysis.
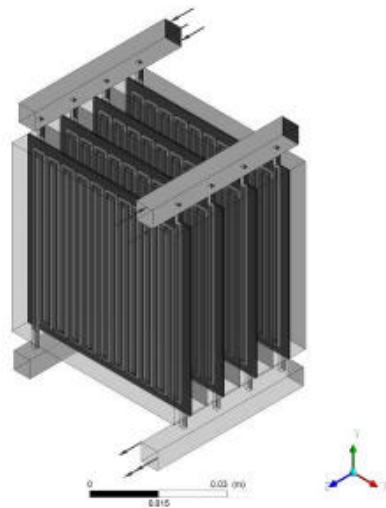

Figure 6-11 : Computational domain of the 4 cell stack

Following conservation balance equations have been used in this work.

For mass conservation:

$$\nabla.(\rho U) = S_c \tag{6.19}$$

For momentum conservation:

$$\nabla.(\rho U \otimes U) = -\nabla p + \nabla.(\mu \nabla U) + S_m \tag{6.20}$$

For species transport:

$$\nabla.(\overline{\rho}_i \overline{U}_j Y_i) = \nabla.(D_{i,eff} \nabla Y_i) + S_i \tag{6.21}$$

In the species transport equation $\overline{\rho}_i$ is the mass-average density of fluid component i in the mixture, $\overline{U}_j$ is the mass-average velocity field, j is representing the x,y,z components of the velocity. $D_{i,eff}$ is the effective diffusivity and Y_i is the mass fraction of component i.

The energy equation reads:

$$\nabla.(\rho U h) = \nabla.(\lambda \nabla T) + S_e \tag{6.22}$$

In the above governing CFD equations S_c, S_m, S_i, S_e are the source terms for continuity, momentum, species transport and energy equations respectively which are explained later. Because of the chemical reaction at the interface of the GDL and membrane the sources for the species transport are employed as follows:

$$S_{H_2} = -\frac{M_{H_2} iA}{2F}, \quad S_{O_2} = -\frac{M_{O_2} iA}{4F}, \quad S_{H_2O} = \frac{M_{H_2O} iA}{2F} \tag{6.23}$$

The negative sign shows the consumption of the species whereas the positive sign is the generation of species. M_i is the molecular mass of the specie i. The porous domain of the GDL is modelled using Darcy law as follows:

$$\nabla p = \frac{\mu}{k_p} U \tag{6.24}$$

where k_p is the permiability, and μ is the dynamic viscosity. The appearance of heat because of the enthalpy of reaction and the dissipation is called the "source term" for the energy equation:

$$S_e = \left(\frac{T(-\Delta S)}{nF} + \eta \right) i \tag{6.25}$$

_____

Here η represent the over-potentials, ΔS is the entropy change for the reaction and n is the number of electron transferred per mole of the reacting species. The electrochemistry of the model is simplified by using the approach of Litster et al. [75]. The local current density is a function of the concentration of the reacting species and the over-potential. For the anode and cathode electrodes it gives:

$$i_a = f(\eta_a, y_{H_2}), \quad i_c = f(\eta_c, y_{O_2})$$

(6.26)

At a given operating current density the activation over-potential is calculated using the Butler Volmer formulation as follows:

$$i = i_0 \left(e^{\frac{\alpha F}{RT}\eta} - e^{\frac{-(1-\alpha)F}{RT}\eta} \right), \quad where \quad i_0 = i_{0ref} a_c L_c \left(\frac{p}{p_{ref}} \right)^{\gamma} e^{\left[\frac{E_c}{RT}\left(1 - \frac{T}{T_{ref}} \right) \right]}$$

(6.27)

The above equation comprises several parameters like the refrence exchange current density i_{0ref}, specific area a_c, catalyst loading L_c, charge transfer coefficient α and activation energy E_c. The numerical values of these parameters can be found in [39]. Multi-component flow assumes that components of the fluid are mixed at the molecular level and that they have a common velocity, pressure and temperature field. Properties of the mixture are based upon the proportion of the components along with their thermodynamic state which are then calculated in a simplified manner as:

$$\phi = \sum_{i=A,B,...}^{N} \phi_i Y_i$$

(6.28)

where A,B,C are components, Y is the mass fraction of the component and ϕ is an arbitrary property. It can be the specific volume, specific heat capacity, viscosity, thermal conductivity etc. For example to calculate the multi-component mixture density using above relation is as follows:

$$\frac{1}{\rho} = \sum_{i=A,B,...}^{N} \frac{Y_i}{\rho_i}$$

(6.29)

here ρ_i is the thermodynamic density of the component.

At the inlets of the stack mass flow rates are given based on the stoichiometry and mass fractions of the reactant components. The mass fraction of water vapor is calculated using the definition of relative humidity. At the outlet the static pressure boundary conditions are employed. The boundary condition at the outer walls of the stack is taken to be convective heat transfer and ambient temperature.

6.2.2 Experimental validation

In order to validate the result of the CFD simulation the experimental setup is made for capturing the temperature distribution in a 4 cell stack along with the polarization curve. The schematic of the setup is shown in Figure 6-12. Pure hydrogen is supplied through a pressurized container and a pressure regulator is used to maintain the required pressure, whereas compressed air is taken from the centralized lab facility. A thermostat is used to get the required temperatures of the reactant streams. Humidification is done by in-house made bubble type humidifiers. The mass flow is measured through mass flow controllers (MFC) of the type based on thermal sensors. The mass flow rate of both reactant streams has maintained at a constant value. Since air is used instead of pure oxygen, the mass flow rate requirement for air is higher than hydrogen. The uncertainty in the measurement of mass flow rate by MFC used in the setup was ±1% of the F.S (Full Scale) range. So for hydrogen it is ±10 sccm (standard cubic centimeter per minute), while for air it is 50 sccm. The temperature and the differential pressure ranges are used within the ranges as recommended by the manufacturer of the MFC. Temperatures are recorded through K-type thermocouples with an accuracy of ±0.5 $^{\circ}$C using a DAQ system including a Lab View program. Both mass flow controllers and thermocouples have been calibrated before usage in the setup. The calibration for all K-type thermocouples used in the setup is made in the laboratory using a Quartz thermometer in the range of 20 to 80 $^{\circ}$C. Heating pads on either side of the endplates are used initially to bring the stack at an operating temperature. The polarization curve is drawn using an electronic load (model EL500) under constant current mode. The sense-on cable in the electronic load is used to nullify the effect of built-in auxiliary voltage of the electronic load, which is on our case is 2.5 V. The inert N_2 gas is used for purging purpose.
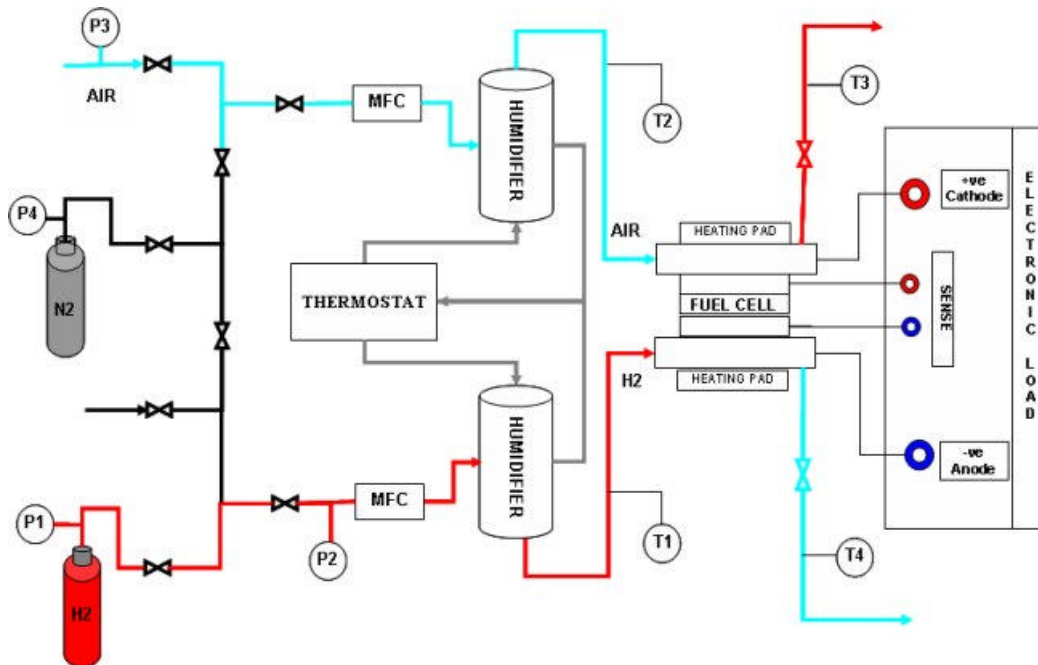

Figure 6-12 : Schematic of experimental setup

The PEM-FC stack is designed and manufactured in-house, thanks to ZMKE (Central Workshop, Helmut-Schmidt-University). A solid model of the Z-type stack is shown in Figure 6-13.
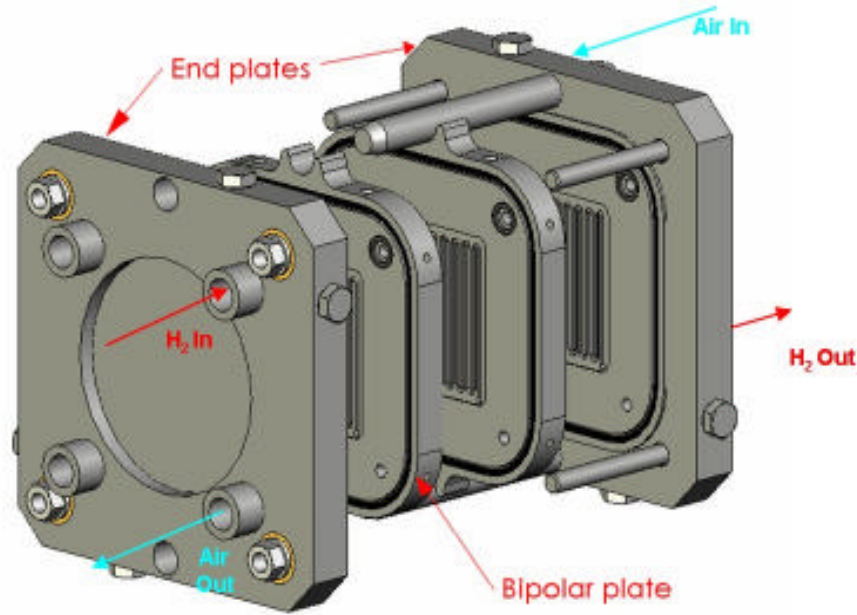
Figure 6-13 : Solid model of the stack

A stack consists of three bipolar plates and two endplates made up of stainless steel (DIN 1013-X6CrNiTi 1810), as shown in Figure 6-14 and Figure 6-15. Five precision drills have been made in each bipolar plate and the end plates for temperature measurements. The purpose of making such a thick bipolar-plate is to accommodate the place for the temperature probe within the bipolar plate thickness. Figure 6-21 shows the positioning of these precision drills in the bipolar-plate. O-rings have been used for sealing. A Nafion-212 membrane with an active area of 25 cm^2 and platinum loading of 0.6 mg/cm^2 at the cathode and 0.3 mg/cm^2 at the anode is used. Carbon paper (S10CC) with micro-layer and 10% hydrophobisation of thickness 0.4 mm is used as a gas diffusion media on either side of the membrane.
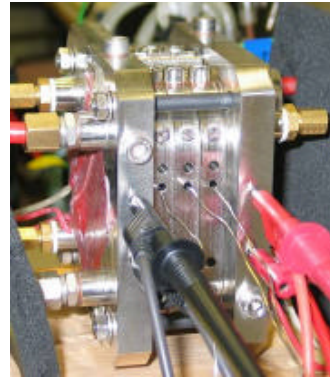

Figure 6-14 : Bipolar plate with serpentine channels   **Figure 6-15 : Four cell PEM-FC stack assembly**

The stack is assembled carefully to take into account the different catalyst loading on cathode and anode side of the membrane as well as maintaining the balanced assembly pressure by tightening the bolts. At higher operating pressure, the unbalanced assembly pressure is crucial

_____

regarding the short circuiting among cells and the leakage of the gas. A polarization curve for the 4 cell stack is shown in Figure 6-16.
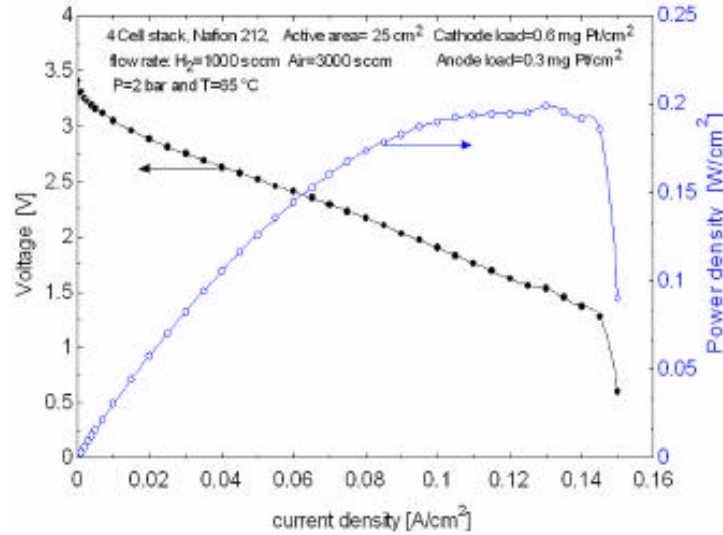

Figure 6-16 : A polarization curve for a four cell stack

The results of the CFD simulation of the four cell stack are shown in Figure 6-17 and Figure 6-18. These results show bigger hot spots at high current densities as well as higher temperatures in the middle of the cell as compared with its ends.
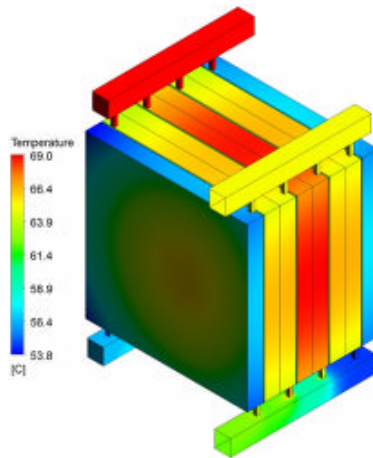
Figure 6-17 : Temperature distribution at a current density of 0.2 A/cm^2
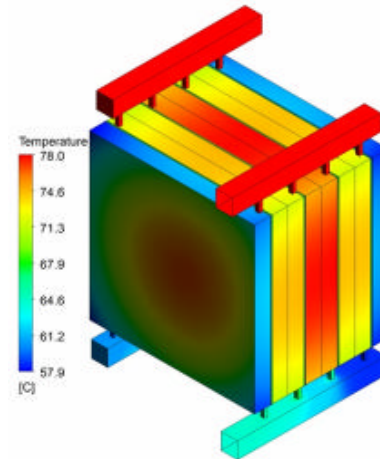
Figure 6-18 : Temperature distribution at a current density of 0.3 A/cm^2

The validation as a result of a comparison between the simulation and the experiment is shown in Figure 6-19. This shows an underestimation of the temperature by simulation as compared with experiment, but the shape of the distribution is alike. This vertical shift of temperature is by virtue of the boundary conditions used in our simulation, which are estimated only. Very recently in reference [36], a temperature distribution for an air-cooled 5 cell stack is reported, the shape of the distribution is very much the same as in our results as shown in Figure 6-20. Higher temperatures in the core of the stack compared with the

_____

perimeter of the stack is might be because of the radiant and convective heat transfer occurs at the perimeter of the stack.
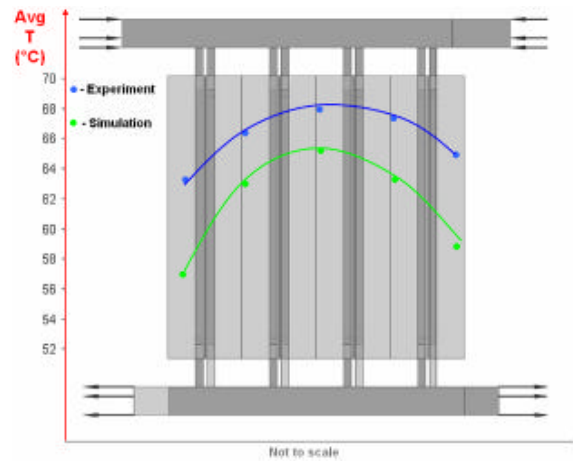
Figure 6-19 : Comparison of average temperature in 4 cell stack.
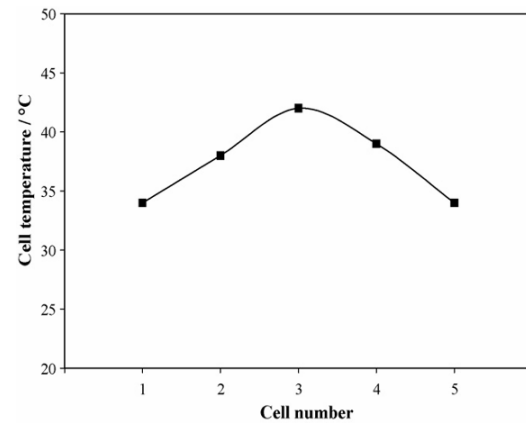
Figure 6-20 : Temperature distribution in the 5-cell stack under a load of 0.2A/cm^2. Ref [36]

As we have seen from the result of the 4 cell stack that there is a temperature distribution across the cells. From our experimental setup we have observed that there is temperature distribution within the cell as well. Figure 6-21 shows the temperature distribution at the cross-section of one of the bipolar plate using 5 thermocouples installed within the active area of 25 cm^2. The average temperature is 66.46°C and the standard deviation is 1.45°C.

Figure 6-21 : Temperature distribution at the cross-section of the bipolar plate.

This result shows that there is a temperature distribution within the small active area of 25 cm^2 even though we have used only a small sample of 5 thermocouples. The positions of

thermocouples are very much evident in Figure 6-21. These thermocouples are inserted approximately in the middle of the bipolar-plate thickness, but up to certain extent from these measurements we can portray the non-uniform distribution exist within the active area of the MEA. In Figure 6-22 the temperature distribution in three bipolar plates are shown at two different load conditions. It is very much clear from the figure that the temperatures have increased at higher load condition.
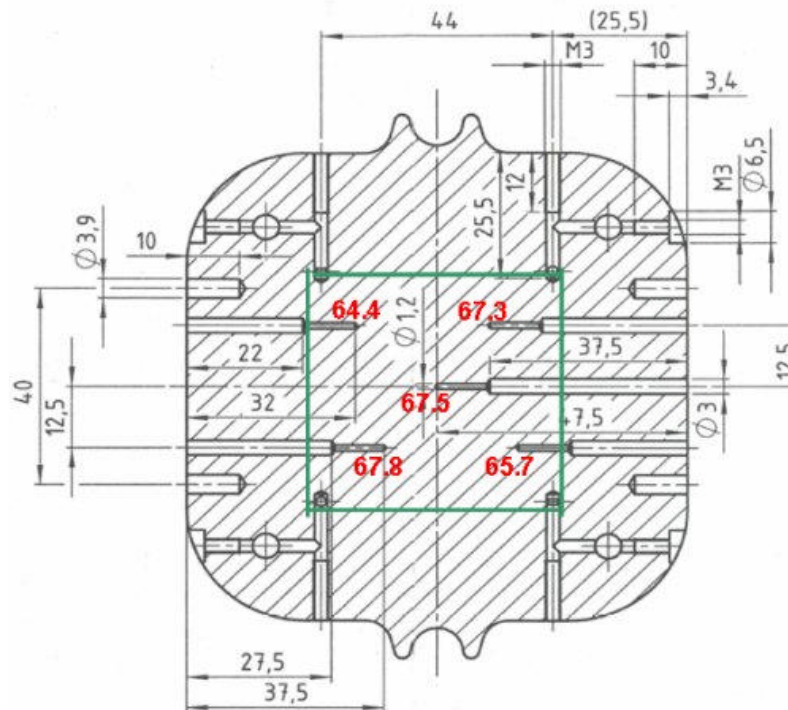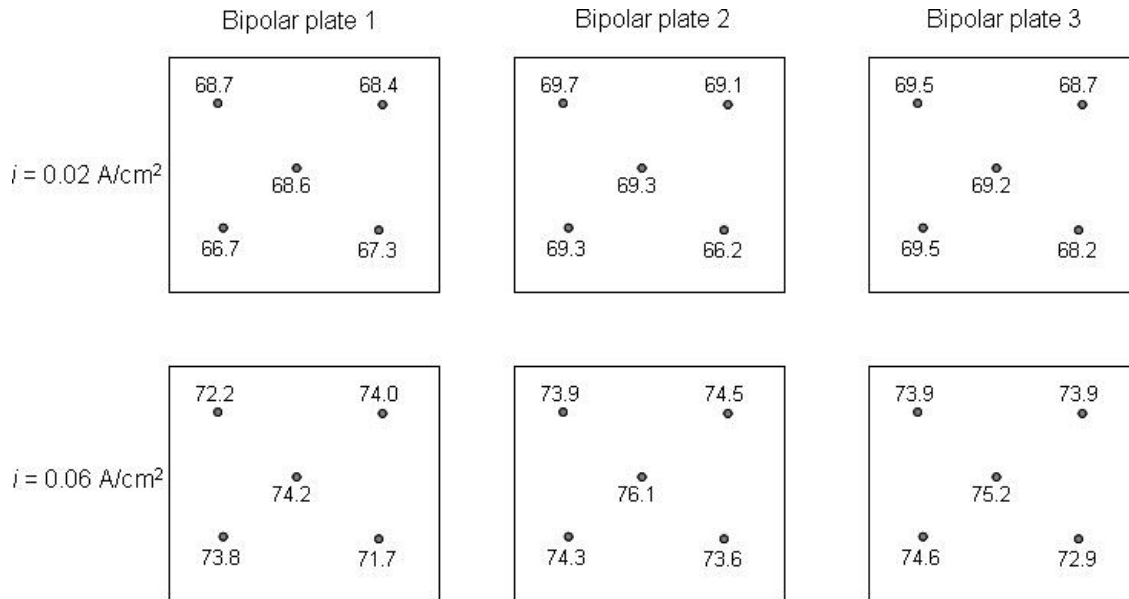

Figure 6-22 : The temperature distribution in three bipolar plates of the 4 cell stack at two load conditions.

In small size stacks cooling is sometimes made by running the small size fan, so the heat is transferred first from the electrodes to the bi-polar plate through conduction and then it is removed by forced convection from the periphery of the stack. The temperature distribution of the stack which is cooled by the fan depends upon several parameters, for example the positioning of the fan can be critical or the speed of the fan has an effect. In our experimental 4 cell stack the temperature distribution is recorded at a given load for two different speeds of the fan named here in Figure 6-23 as Low and High speed. The results indicate that the temperature have dropped when the speed of the fan has increased. In both figures, Figure 6-22 and Figure 6-23 the temperatures at the center of bipolar plates for the middle plate (named Bipolar plate 2) have higher temperatures compared with the adjacent plates at the same position.

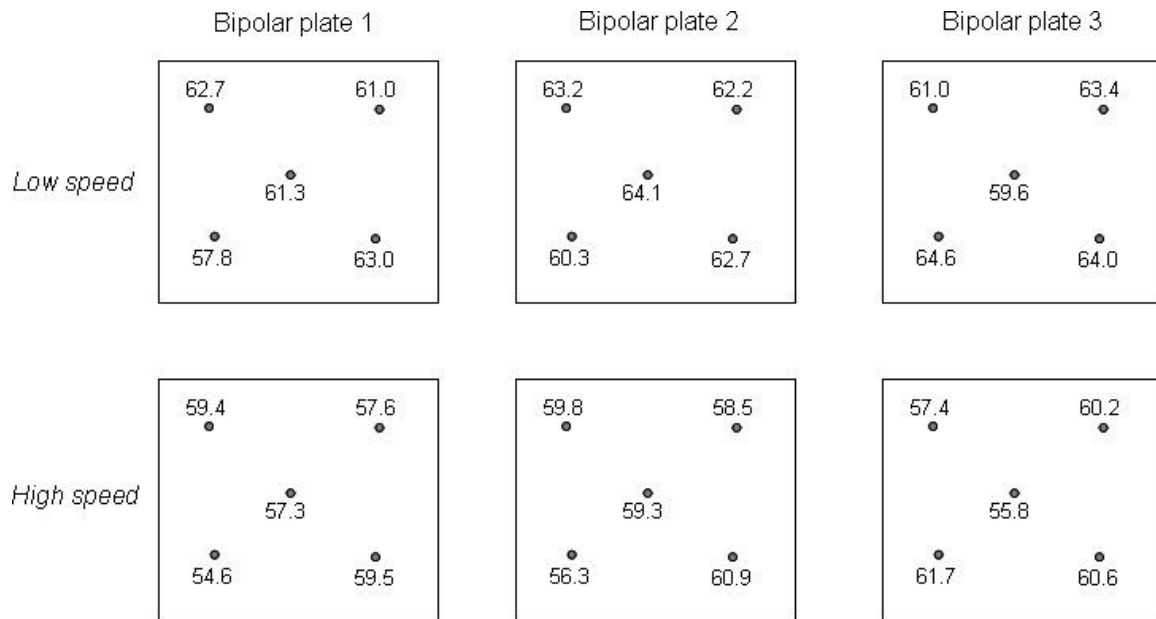**Figure 6-23 : Temperature distribution in three bipolar plates of the 4 cell stack at a given load under low and high speed operation of the cooling fan.**

6.3   Temperature distribution in the stack with different number of cooling plates

Stack cooling can be made by several means depending upon the size of the stack, for small stacks and lower current density operations the reactants streams especially the air supplied at cathode are good enough to carry the heat generated in the stack, for relatively bigger stacks they are cooled by supplying air through forced convection, whereas for large size stacks the cooling has to made through liquid supply.

For liquid cooling stack there is a question that after how many cells the cooling arrangement to me made so that the stack temperature is uniform as much as possible. Figure 6-24 shows schematically three possible arrangements of cooling plates in a fuel cell stack. In the first case the cooling plate is provided after every next cell, whereas in the second and third case the cooling plates are installed after every third and fifth cell respectively.
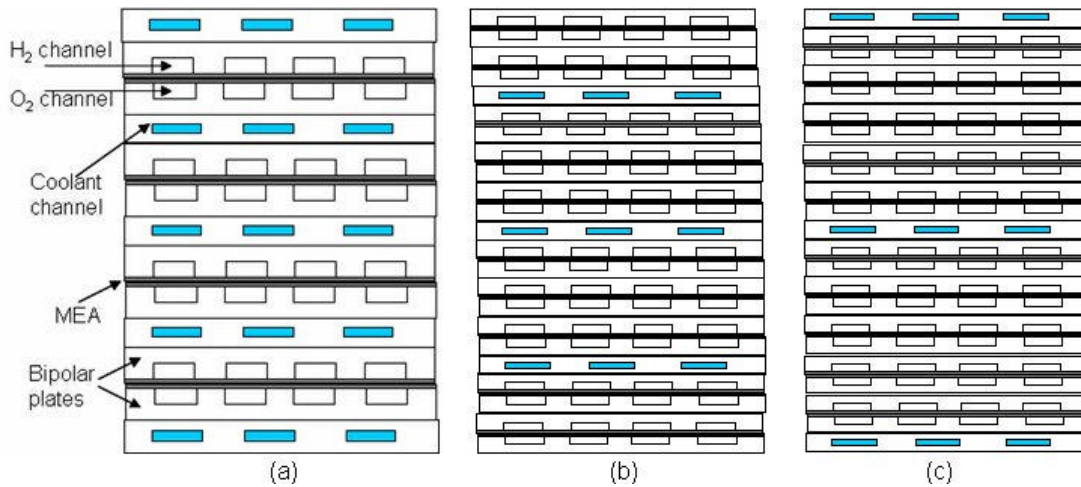
Figure 6-24 : Schematic of a fuel cell stack with cooling plates after (a) every cell (b) every third cell   (c) every fifth cell.

In this study these three cases are analyzed numerically at a steady state condition through CFD, the details of the parameters used in the CFD model are shown in the Table 6-6.

Table 6-6 : Parameters used in the fuel cell stack with different number of cooling blocks

parameter	value
Dimensions of coling block (cm)	$(25 \times 25 \times 0.3)$
Cooling channel cross section (mm)	(10×1.5)
Active area (cm^2)	625
Cooling fluid	water
Bipolar and cooling plate thermal conductivity	15
MEA thermal conductivity (W/mK)	1.7
Inlet fluid temperature (ºC)	50
Uniform heat flux (W/m^2)	1200
Pressure (bar)	1.5
Outer wall and end plate boundary condition	convective

The CFD model comprises one fluid domain and two solid domains so this is conjugate heat transfer problem. Cooling fluid is entered through headers, and the walls of the headers are taken adiabatic which means we are not going to model heat transfer in the headers. The flow rate of the cooling fluid is calculated through energy balance in such a way that the temperature difference from inlet of the cooling fluid to the outlet remains less than 10 ºC. So inherently we are assuming that the heat exchanger for the cooling fluid is good enough to give us the temperature difference of 10 ºC at a given heat load. As pointed out in reference [45] the demand for heat dissipation in the cooling heat exchanger with a PEM fuel cell drive is approximately doubled compared to that of conventional internal combustion engines. The reasons are the low temperature of the PEM fuel cell, low mass flow rate of the cooling fluid, and inability of the exhaust streams to carry away the heat compared with combustion engines. The outer walls of the stack have been given the convective boundary condition. The outer temperature is taken 25 ºC and the outer convective heat transfer coefficient is assumed 12 W/m^{2}K. This convective boundary condition tries to model the space provided in the casing of the stack. All commercial sized stacks are installed under a casing. For the two end plates the same convective boundary condition is used except the value of the convective heat transfer coefficient is assumed a little higher value of 20 W/m^{2}K. These boundary conditions are important parameters for providing the constraint to the energy equation of the model and the resulting temperature distribution. The heat generated through the electrochemical reaction is modeled by giving a uniform heat flux at the interface of the bipolar plate and the MEA (two solid domains) of every cell. A temperature distribution of one of the case (a 33 cell stack with 10 cooling blocks) is shown in Figure 6-25. For clarity only the outer wall temperatures are shown in this figure so that the serpentine cooling channels can be visible.

Figure 6-25 : Temperature distribution in 33 cell stack with serpentine cooling channels after every third cell.

In order to compare the temperature distribution of the stack with different number of cooling blocks a temperature is probed right in the center of the stack along the length as shown in Figure 6-26. This result shows that the temperature difference between the two adjacent cells is low in the case when cooling is provided after every cell compared with the case in which the coolin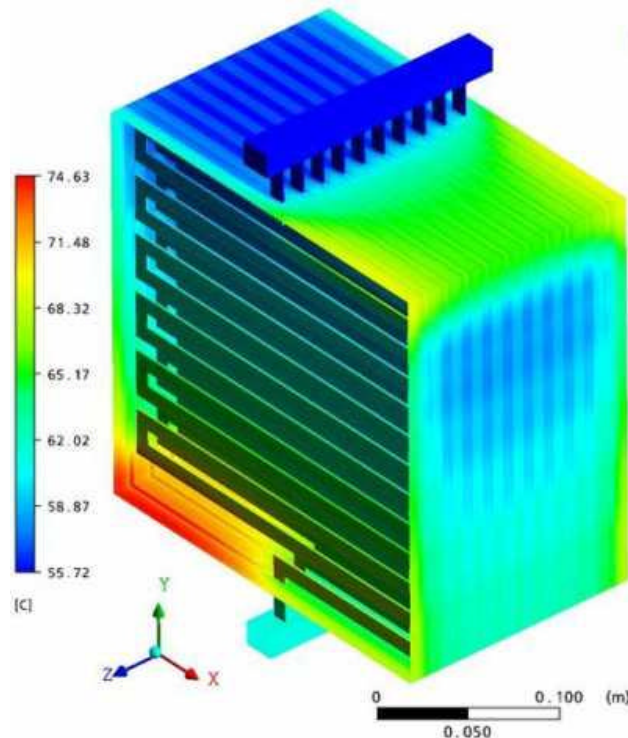g arrangement is made after every third and fifth cell. The slight higher value of convective heat transfer coefficient taken at the end plates is not sufficient to take away the heat from the bunch of cells at the end, so cooling arrangement is needed at the end plates as well.
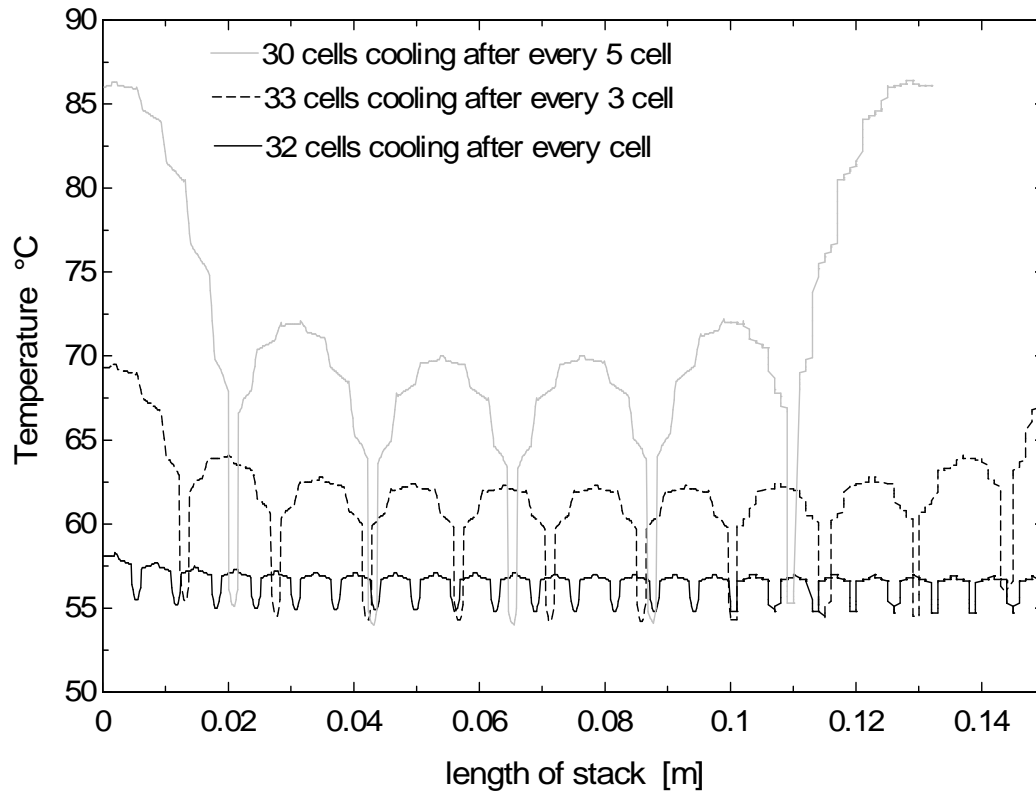
Figure 6-26 : Temperature in the center of the stack along the length for three different cooling arrangements.

The temperature distribution given in Figure 6-26 clearly indicates that the cooling plate after every third cell gives a reasonable temperature difference for the cooling system compared with cooling plates after every fifth cell. A decision for designer surely depends upon what temperature difference the cooling loop can sustain. For smaller heat exchangers in cooling loop it may be appropriate to provide cooling plate for every two cells or after every cell. There is always a tradeoff between the number of cooling plates and available heat exchanger size. Another point in designers mind is the thickness of the cooling plate. Usually in commercial size stacks the thickness of the plate is bit larger than the thickness of a cell. So putting more cooling plates would obviously increase the weight and the size of the stack. Both size and weight are crucial parameters for automotive applications.

_____

7 Summary and Future work

Summary

This thesis is about the cooling strategies for PEM fuel cell stack. PEM fuel produces heat of the same order with electrical power, but because of the low operating temperature the removal of heat is more challenging than internal combustion engines. A strategy adopted in this work is first to analyze the heat sources in a single fuel cell, and derived heat fluxes from single cell has been transferred to a commercial size stack in order to get the temperature distribution. A heat source in fuel cell comprises reversible and irreversible heat sources. Reversible heat source is due to the entropy change of the electro-chemical reaction. Irreversible heat source is due to the activation polarization and internal resistances. Chapter 2 of the thesis covers these heat sources; additionally the theory of irreversible thermodynamics is explained for the PEM fuel cell membrane to show the coupled nature of heat and mass fluxes. Chapter 3 describes a model of a single cell based on the reactant concentration changes at the electrodes resulting in a non-uniform heat flux distribution. Chapter 4 examines the variation of stack configuration and properties on the heat flux distribution. Chapter 5 gives the basics of Computational fluid dynamics (CFD) and solved two benchmark problems of pipe flow with heat transfer for both laminar and turbulent case. In chapter 6 different designs for the cooling channels are analyzed numerically with conjugate heat transfer and optimized through the calculation of total entropy generation in the cooling plate. Both single and multiple cooling channels are considered in the analysis. The second section of this chapter, a four cell stack is developed through CFD and compared the temperature distribution with a four cell stack designed and manufactured in-house. Last in this chapter a distribution of temperature is analyzed numerically in a commercial size 30 cell stack with different number of cooling plates.

In short, this thesis covers the realization of heat sources and sinks in PEM fuel cell stack, the in-house design and development of a 4 cell stack, the CFD model of the 4 cell stack is developed and validated through experiment, sensitivity of different stack-flow configuration is investigated, the different cooling channel flow-field designs are proposed for the liquid cooling and optimization is made through minimization of entropy generation, and the temperature distribution of commercial size stack with different number of cooling plates is shown.

Future work

Following conclusions have been made from this work which can be incorporated in the future work:

- Local heat fluxes arising from reversible heat generation are not yet clear especially due to the uncertainties in the entropy change of the half-cell reaction.

- There is a need to apply realistic boundary conditions especially at the outer surfaces of the stack.

- Boundary conditions used in single channel or cell are not equally good for stack modeling.

_____

- It is difficult to bring about a truly steady state in experiments in-contrast with assumptions in simulation.

- Heat transfer within porous media require conductivities of both solid and fluid (λ_s, λ_f) have to be taken into an account.

- The anisotropic nature of porous media shall be included in future.

- The contact resistances shall be modeled.

- The CFD model can be enhanced for example by incorporating the two-phase flow models.

Appendix

A- Evaluation of electric current in the absence of the transport of heat and water in the membrane.

Consider a situation in which we have to evaluate the electric current density in the absence of heat and water transport.

Substitute $J_q=0$ and assume $E = -\dfrac{d\phi}{dz}$ in equation (2.53) we get A-1

$$L_{q\phi}E = \frac{L_{qq}}{T}\frac{dT}{dz} + L_{qw}\frac{d\mu_{w,T}}{dz} \qquad\qquad \text{A-1}$$

Similarly substitute $J_w=0$ and assume $E = -\dfrac{d\phi}{dz}$ in equation (2.54) we get A-2

$$L_{w\phi}E = \frac{L_{wq}}{T}\frac{dT}{dz} + L_{ww}\frac{d\mu_{w,T}}{dz} \qquad\qquad \text{A-2}$$

By solving A-1 and A-2 such a way that we eliminate the gradient of chemical potential term we get A-3.

$$\frac{1}{T}\frac{dT}{dz} = \frac{L_{qw}L_{w\phi} - L_{ww}L_{q\phi}}{L_{wq}L_{qw} - L_{qq}L_{ww}} E \qquad\qquad \text{A-3}$$

By solving A-1 and A-2 such a way that we eliminate the gradient of temperature term we get A-3.

$$\frac{d\mu_{w,T}}{dz} = \frac{L_{qq}L_{q\phi} - L_{wq}L_{q\phi}}{L_{qq}L_{ww} - L_{wq}L_{qw}} E \qquad\qquad \text{A-4}$$

Now substitute A-3 and A-4 in equation (2.55) and apply the Onsager's relation we get A-5

$$i = \frac{E}{T}\left[L_{\phi\phi} - L_{\phi q}\frac{L_{q\phi}L_{ww} - L_{qw}L_{w\phi}}{L_{qq}L_{ww} - L_{qw}^{\;2}} - L_{\phi w}\frac{L_{qq}L_{w\phi} - L_{wq}L_{q\phi}}{L_{qq}L_{ww} - L_{qw}^{\;2}} \right] \qquad\qquad \text{A-5}$$

_____

B- Phenomenological coefficient for diffusion when temperature gradient and the current are vanishing.

From equation (2.60)

$$J_w = -\frac{l_{wq}}{T^2}\frac{dT}{dz} - \frac{l_{ww}}{T}\frac{d\mu_{w,T}}{dz} + \frac{L_{w\phi}}{L_{\phi\phi}}i$$

B-1

Substitute $dT=0$ and $i=0$ result in equation

$$J_w = -\frac{l_{ww}}{T}\frac{d\mu_{w,T}}{dz}$$

B-2

Now using the definition of chemical potential of water on molar concentration basis $\mu_w = \mu_w{}^0 + RT\ln C_w$ by the help of chain rule $\dfrac{d\mu}{dz} = \dfrac{d\mu}{dC_w}\dfrac{dC_w}{dz}$ we can transform the chemical potential gradient into concentration gradient. Equation B-2 can be written as

$$J_w = -\frac{l_{ww}}{T}\frac{RT}{C_w}\frac{dC_w}{dz}$$

B-3

According to Fick's law of diffusion

$$J_w = -D_w\frac{dC_w}{dz}$$

B-4

By comparing B-3 with B-4 one gets the relation for the phenomenological coefficient of pure diffusion.

$$\frac{l_{ww}}{T} = D_w\frac{C_w}{RT}$$

B-5

_____

C- Local entropy generation rate in convective heat transfer

Consider a differential fluid element of volume ($dxdy \times 1$) subject to mass flux, energy transfer, and entropy transfer at point (x,y) of Cartesian coordinate system as shown in Figure C-1.
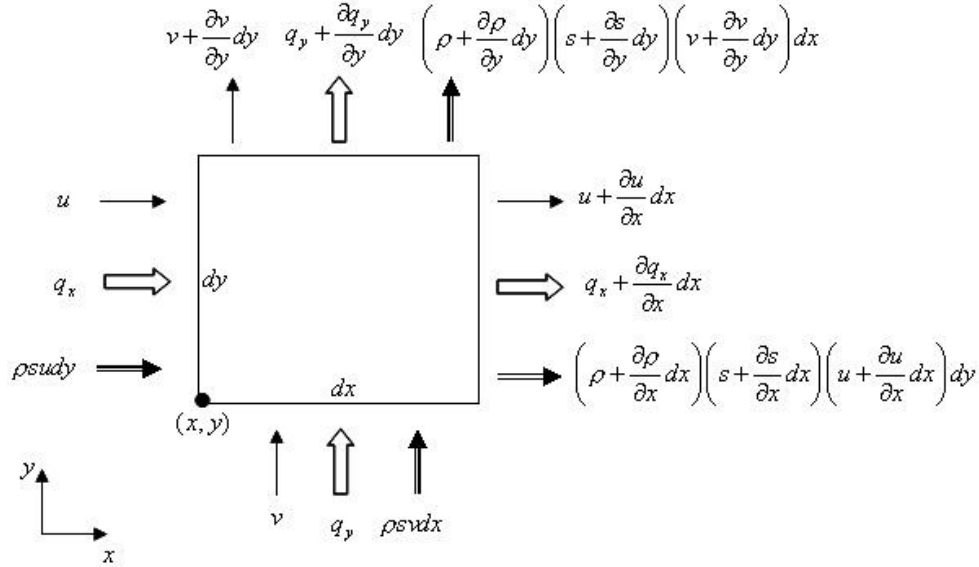
Figure C-0-1: Differential fluid element subject to mass fluxes, heat transfer, and entropy transfer.

According to second law of thermodynamics for an open system, the balance equation for the entropy S, is

$$\frac{\partial S}{\partial t} = \sum_{in} \dot{m}_{in} s_{in} - \sum_{out} \dot{m}_{out} s_{out} + \frac{\dot{Q}}{T} + \dot{S}_{gen} \qquad \text{C-1}$$

Now applying the balance equation for the entropy to the above fluid element we get

$$\frac{\partial(\rho s)}{\partial t} dxdy = \rho sudy + \rho svdx - \left(\rho + \frac{\partial \rho}{\partial x} dx\right)\left(s + \frac{\partial s}{\partial x} dx\right)\left(u + \frac{\partial u}{\partial x} dx\right) dy$$

$$- \left(\rho + \frac{\partial \rho}{\partial y} dy\right)\left(s + \frac{\partial s}{\partial y} dy\right)\left(v + \frac{\partial v}{\partial y} dy\right) dx + \frac{q_x}{T} dy + \frac{q_y}{T} dx$$

$$- \frac{q_x + \frac{\partial q_x}{\partial x} dx}{T + \frac{\partial T}{\partial x} dx} dy - \frac{q_y + \frac{\partial q_y}{\partial y} dy}{T + \frac{\partial T}{\partial y} dy} dx + \dot{S}'''_{gen}(dxdy) \qquad \text{C-2}$$

After simplification and dividing by $dxdy$, the local entropy generation per unit volume $\dot{S}'''_{gen}$ [W/m^{3}K] becomes

_____

$$\dot{S}_{gen}^{m} = \frac{1}{T}\left(\frac{\partial q_x}{\partial x} + \frac{\partial q_y}{\partial y}\right) - \frac{1}{T^2}\left(q_x\frac{\partial T}{\partial x} + q_y\frac{\partial T}{\partial y}\right) + \rho\left(\frac{\partial s}{\partial t} + u\frac{\partial s}{\partial x} + v\frac{\partial s}{\partial y}\right)$$
$$+ s\left[\frac{\partial \rho}{\partial t} + u\frac{\partial \rho}{\partial x} + v\frac{\partial \rho}{\partial y} + \rho\left(\frac{\partial u}{\partial x} + \frac{\partial v}{\partial y}\right)\right] \qquad \text{C-3}$$

The above equation can be written in vector form as

$$\dot{S}_{gen}^{m} = \frac{1}{T}\nabla\cdot\vec{q} - \frac{1}{T^2}\vec{q}\cdot\nabla T + \rho\frac{Ds}{Dt} + s\left[\frac{D\rho}{Dt} + \rho(\nabla\cdot\vec{v})\right] \qquad \text{C-4}$$

where $\vec{v}$ is the velocity vector with component (u,v,w) and D/Dt is the substantial derivative as

$$\frac{D}{Dt} = \frac{\partial}{\partial t} + u\frac{\partial}{\partial x} + v\frac{\partial}{\partial y} + w\frac{\partial}{\partial z} \qquad \text{C-5}$$

According to mass conservation principle

$$\frac{D\rho}{Dt} + \rho(\nabla\cdot\vec{v}) = 0 \qquad \text{C-6}$$

Now by applying the mass conservation, the equation C-4 can be written as

$$\dot{S}_{gen}^{m} = \frac{1}{T}\nabla\cdot\vec{q} - \frac{1}{T^2}\vec{q}\cdot\nabla T + \rho\frac{Ds}{Dt} \qquad \text{C-7}$$

We know the canonical relation $du = Tds - pd\left(\frac{1}{\rho}\right)$, here u is the internal energy, and this can be written as $\rho ds = \frac{\rho}{T}du - \frac{p}{T\rho}d\rho$. Now using the substantial derivative and the simplified canonical relation we can write as

$$\rho\frac{Ds}{Dt} = \frac{\rho}{T}\frac{Du}{Dt} - \frac{p}{\rho T}\frac{D\rho}{Dt} \qquad \text{C-8}$$

According to first law of thermodynamics the rate of change in internal energy (u) per unit volume equal to the net heat transfer by conduction, plus the work transfer rate due to compression, plus the work transfer rate associated with viscous dissipation. Mathematically it can be written as

_____

$$\rho \frac{Du}{Dt} = -\nabla \cdot \vec{q} - p\left(\nabla \cdot \vec{\mathrm{v}}\right) + \mu \, \Phi \qquad\qquad \text{C-9}$$

In equation C-9 it is assumed that the fluid is Newtonian and μ is the viscosity and Φ is the viscous dissipation function defined as

$$
\begin{aligned}
\Phi = 2 & \left[\left(\frac{\partial u}{\partial x}\right)^2 + \left(\frac{\partial v}{\partial y}\right)^2 + \left(\frac{\partial w}{\partial z}\right)^2 \right] \\
& + \left[\left(\frac{\partial u}{\partial y} + \frac{\partial v}{\partial x}\right)^2 + \left(\frac{\partial v}{\partial z} + \frac{\partial w}{\partial y}\right)^2 + \left(\frac{\partial w}{\partial x} + \frac{\partial u}{\partial z}\right)^2 \right] \\
& - \frac{2}{3}\left(\frac{\partial u}{\partial x} + \frac{\partial v}{\partial y} + \frac{\partial w}{\partial z}\right)^2 \quad .
\end{aligned}
\qquad \text{C-10}
$$

The last term in the right hand side of equation C-10 will be zero for incompressible fluid.

By combining equations C-6 C-8, C-9 into C-7 we obtained

$$\dot{S}'''_{gen} = -\frac{1}{T^2}\vec{q} \cdot \nabla T + \frac{\mu}{T}\Phi \qquad\qquad \text{C-11}$$

Now according to Fourier law of heat conduction for an isotropic medium with thermal conductivity k

$$\vec{q} = -k\nabla T \qquad\qquad \text{C-12}$$

the volumetric rate of entropy generation becomes

$$\dot{S}'''_{gen} = \frac{k}{T^2}\left(\nabla T\right)^2 + \frac{\mu}{T}\Phi \qquad\qquad \text{C-13}$$

References

[1]   P. Atkins, *Atkins' physical chemistry*. 8 ed, Oxford: Oxford University Press, 2006.

[2]   B. d. Darwent, *Bond dissociation energies in simple molecules*. Washington: U.S. National Bureau of Standards; U.S. Govt. Print. Off., 1970

[3]   M. W. Chase and et al., *JANAF thermochemical tables*, 3 ed. Washington, D.C: American Chemical Society; American Institute of Physics for the National Bureau of Standards, 1986.

[4]   I. Barin and G. Platzki, *Thermochemical data of pure substances*. Weinheim: VCH, 1995.

[5]   M. J. Lampinen and M. Fomino, "Analysis of Free Energy and Entropy Changes for Half-Cell Reactions," *Journal of The Electrochemical Society*, vol. 140, pp. 3537-3546, 1993.

[6]   J. Ramousse, O. Lottin, S. Didierjean, and D. Maillet, "Heat sources in proton exchange membrane (PEM) fuel cells," *Journal of Power Sources*, vol. 192, pp. 435-441, 2009.

[7]   A. L. Rockwood, "Absolute half-cell entropy," *Physical Review A*, vol. 36, pp. 1525-1526, 1987.

[8]   M. Wöhr, K. Bolwin, W. Schnurnberger, M. Fischer, W. Neubrand, and G. Eigenberger, "Dynamic modelling and simulation of a polymer membrane fuel cell including mass transport limitation," *International Journal of Hydrogen Energy*, vol. 23, pp. 213-218, 1998.

[9]   H. Ju, H. Meng, and C.-Y. Wang, "A single-phase, non-isothermal model for PEM fuel cells," *International Journal of Heat and Mass Transfer*, vol. 48, pp. 1303-1315, 2005.

[10]   T. Watari, H. Wang, K. Kuwahara, K. Tanaka, H. Kita, and K.-i. Okamoto, "Water vapor sorption and   diffusion properties of sulfonated polyimide membranes," *Journal of Membrane Science*, vol. 219, pp. 137-147, 2003.

[11]   P. J. Reucroft, D. Rivin, and N. S. Schneider, "Thermodynamics of Nafion(TM)-vapor interactions. I. Water vapor," *Polymer*, vol. 43, pp. 5157-5161, 2002.

[12]   D. J. Burnett, A. R. Garcia, and F. Thielmann, "Measuring moisture sorption and diffusion kinetics on proton exchange membranes using a gravimetric vapor sorption apparatus," *Journal of Power Sources*, vol. 160, pp. 426-430, 2006.

[13]   P. W. Majsztrik, M. B. Satterfield, A. B. Bocarsly, and J. B. Benziger, "Water sorption, desorption and transport in Nafion membranes," *Journal of Membrane Science*, vol. 301, pp. 93-106, 2007.

[14]   M. M. Mench, *Fuel cell engines*. Hoboken, N.J: John Wiley & Sons, 2008.

[15]   R. W. Balluffi, S. M. Allen, and W. C. Carter, *Kinetics of materials*. Hoboken, NJ: Wiley, 2005.

[16]   L. M. Martyushev and V. D. Seleznev, "Maximum entropy production principle in physics, chemistry and biology," *Physics Reports*, vol. 426, pp. 1-45, 2006.

[17]   J. Zhang, *PEM fuel cell electrocatalysts and catalyst layers: fundamentals and applications*. London: Springer, 2008.

[18]   J. O. M. Bockris, A. K. N. Reddy, M. Gamboa-Aldeco, and I. NetLibrary, "Modern electrochemistry. Volume 2A, Fundamentals of electrodics." New York: Kluwer Academic, 2002.

[19]   R. F. Mann, J. C. Amphlett, B. A. Peppley, and C. P. Thurgood, "Application of Butler-Volmer equations in the modelling of activation polarization for PEM fuel cells," *Journal of Power Sources*, vol. 161, pp. 775-781, 2006.

[20]   L. Horváth and I. J. Rudas, *Modeling and problem solving techniques for engineers*. Boston: Elsevier Academic Press, 2004.

[21]   S. Owen , An Introduction to Mesh Generation Algorithms, Sandia National laboratories 14th International Meshing Roundtable, San Diego, USA, 2005.

[22]   J. H. Lienhard and J. H. Lienhard, *A heat transfer textbook*. 3 ed, Cambridge, MA: Phlogiston Press, 2004.

[23]   A. Bejan, *Convection heat transfer*. Hoboken, N.J: Wiley, 2004.

[24]   Y. Cengel, *Heat transfer: A practical approach*, 2 ed, New York: McGraw-Hill, 2002.

[25]   S. Chintada, K.-H. Ko, and N. K. Anand, "HEAT TRANSFER IN 3-D SERPENTINE CHANNELS WITH RIGHT-ANGLE TURNS," *Numerical Heat Transfer, Part A: Applications: An International Journal of Computation and Methodology*, vol. 36, pp. 781-806, 1999.

[26]   W. Viser, T. Esch, F. Menter, and P. Smirnov, "Heat transfer predictions using advanced two-equation turbulence models," ANSYS, CFX Validation report, Otterfing: Germany, 2007.

[27]   H. K. Versteeg and W. Malalasekera, *An introduction to computational fluid dynamics: the finite volume method*. Harlow, U.K; New York: Pearson Education, 2007.

[28]   J. D. Anderson, *Computational fluid dynamics: the basics with applications*. New York: McGraw-Hill, 1994.

[29]   A. W. Date, *Introduction to computational fluid dynamics*. New York: Cambridge University Press, 2005

[30]   J. H. Lee, "Coolant flow field design for fuel cell stacks," in *U.S Patent 6924052 B2*, Aug. 2, 2005.

[31]   J. A. Rock, "PEM fuel cell with flow-field having a branched midsection," in *U.S Patent 2004/0151971 A1*, Aug. 5, 2004.

[32]   H. K. Atiyeh, K. Karan, B. Peppley, A. Phoenix, E. Halliop, and J. Pharoah, "Experimental investigation of the role of a microporous layer on the water transport and performance of a PEM fuel cell," *Journal of Power Sources*, vol. 170, pp. 111-121, 2007.

[33]   J. J. Hwang, "A complete two-phase model of a porous cathode of a PEM fuel cell," *Journal of Power Sources*, vol. 164, pp. 174-181, 2007.

[34]   G. He, Z. Zhao, P. Ming, A. Abuliti, and C. Yin, "A fractal model for predicting permeability and liquid water relative permeability in the gas diffusion layer (GDL) of PEMFCs," *Journal of Power Sources*, vol. 163, pp. 846-852, 2007.

[35]   S. M. H. Hashmi and S. Kabelac, "Temperature distribution in PEM-FC stacks -experimental and theoretical," presented at International Conference of Hydrogen & Fuel Cells, Vancouver, Canada, 2009.

[36]   J. Wu, S. Galli, I. Lagana, A. Pozio, G. Monteleone, X. Z. Yuan, J. Martin, and H. Wang, "An air-cooled proton exchange membrane fuel cell with combined oxidant and coolant flow," *Journal of Power Sources*, vol. 188, pp. 199-204, 2009.

[37]   T. E. Springer, T. A. Zawodzinski, and S. Gottesfeld, "Polymer Electrolyte Fuel Cell Model," *Journal of The Electrochemical Society*, vol. 138, pp. 2334-2342, 1991.

[38]   S. Um, C.-Y. Wang, and K. S. Chen, "Computational Fluid Dynamics Modeling of Proton Exchange Membrane Fuel Cells," *Journal of The Electrochemical Society*, vol. 147, pp. 4485-4493, 2000

[39]   F. Barbir, *PEM fuel cells : theory and practice*. Amsterdam: Elsevier Academic Press, 2005

[40]   J. T. Hinatsu, M. Mizuhata, and H. Takenaka, "Water Uptake of Perfluorosulfonic Acid Membranes from Liquid Water and Water Vapor," *Journal of The Electrochemical Society*, vol. 141, pp. 1493-1498, 1994.

[41]   P. Choi and R. Datta, "Sorption in Proton-Exchange Membranes," *Journal of The Electrochemical Society*, vol. 150, pp. E601-E607, 2003.

[42]   R. K. Shah and A. L. London, Laminar flow forced convection in ducts: a source book for compact heat exchanger analytical data. New York: Academic Press, 1978.

[43]   A. Bejan, *Entropy generation minimization: the method of thermodynamic optimization of finite-size systems and finite-time processes*, Boca Raton: CRC Press, 1996.

[44]   F. C. Chen, Z. Gao, R. O. Loutfy, and M. Hecht, "Analysis of optimal heat transfer in a PEM fuel cell cooling plate," *Fuel Cells*, vol. 3, pp. 181-188, 2003.

[45]   S. Rogg, M. Höglinger, E. Zwittig, C. Pfender, W. Kaiser, and T. Heckenberger, "Cooling Modules for Vehicles with a Fuel Cell Drive," *Fuel Cells*, vol. 3, pp. 153-158, 2003.

[46]   S. Kjelstrup and D. Bedeaux, *Non-equilibrium thermodynamics of heterogeneous systems*. Hackensack, NJ: World Scientific, 2008.

[47]   M. Siemer, *Lokale Entropieproduktionsraten in der Polymerelektrolyt-Membran-Brennstoffzelle*, Dissertation/PhD-thesis, Helmut-Schmidt-Universität/Universität der Bundeswehr Hamburg, 2007.

[48]   S. K. Ratkje, M. Ottøy, R. Halseid, and M. Strømgård, "Thermoelectric Power relevant for the Solid-Polymer-Electrolyte fuel cell," *Journal of Membrane Science*, vol. 107, pp. 219-228, 1995.

[49]   J. Choi, Y.-H. Kim, Y. Lee, K.-J. Lee, and Y. Kim, "Numerical Analysis on the Performance of cooling plates in a PEFC," *Journal of Mechanical Science and Technology*, vol. 22, pp. 1417-1425, 2008.

[50]   S. H. Yu, S. Sohn, J. H. Nam, and C.-J. Kim, "Numerical study to examine the performance of multi-pass serpentine flow-fields for cooling plates in polymer electrolyte membrane fuel cells," *Journal of Power Sources*, vol. 194, pp. 697-703, 2009.

[51]   C. Xu and T. S. Zhao, "A new flow field design for polymer electrolyte-based fuel cells," *Electrochemistry Communications*, vol. 9, pp. 497-503, 2007.

[52]   J. Zhang, Y. Tang, C. Song, J. Zhang, and H. Wang, "PEM Fuel Cell Open Circuit Voltage (OCV) in the temperature range of 23°C to 120°C," *Journal of Power Sources*, vol. 163, pp. 532-537, 2006.

[53]   C. Song, Y. Tang, J. L. Zhang, J. Zhang, H. Wang, J. Shen, S. McDermid, J. Li, and P. Kozak, "PEM fuel cell reaction kinetics in the temperature range of 23-120°C," *Electrochimica Acta*, vol. 52, pp. 2552-2561, 2007.

[54]   M. Inaba, T. Kinumoto, M. Kiriake, R. Umebayashi, A. Tasaka, and Z. Ogumi, "Gas crossover and membrane degradation in polymer electrolyte fuel cells," *Electrochimica Acta*, vol. 51, pp. 5746-5753, 2006.

[55]   S. A. Vilekar and R. Datta, "The effect of hydrogen crossover on open-circuit voltage in polymer electrolyte membrane fuel cells," *Journal of Power Sources*, vol. 195, pp. 2241-2247, 2010.

[56]   J. Zhang, Z. Xie, J. Zhang, Y. Tang, C. Song, T. Navessin, Z. Shi, D. Song, H. Wang, D. P. Wilkinson, Z.-S. Liu, and S. Holdcroft, "High temperature PEM fuel cells," *Journal of Power Sources*, vol. 160, pp. 872-891, 2006.

[57]   S. Shafiee and E. Topal, "When will fossil fuel reserves be diminished?," *Energy Policy*, vol. 37, pp. 181-189, 2009.

[58]   C.-Y. Wang, "Fundamental Models for Fuel Cell Engineering," *Chemical Reviews*, vol. 104, pp. 4727-4766, 2004.

[59]   A. Z. Weber and J. Newman, "Modeling Transport in Polymer-Electrolyte Fuel Cells," *Chemical Reviews*, vol. 104, pp. 4679-4726, 2004.

[60]   A. BIyIkoglu, "Review of proton exchange membrane fuel cell models," *International Journal of Hydrogen Energy*, vol. 30, pp. 1181-1212, 2005.

[61]   C. Siegel, "Review of computational heat and mass transfer modeling in polymer-electrolyte-membrane (PEM) fuel cells," *Energy*, vol. 33, pp. 1331-1352, 2008.

[62]   P. T. Nguyen, T. Berning, and N. Djilali, "Computational model of a PEM fuel cell with serpentine gas flow channels," *Journal of Power Sources*, vol. 130, pp. 149-157, 2004.

[63]   C. M. Baca, R. Travis, and M. Bang, "Three-dimensional, single-phase, non-isothermal CFD model of a PEM fuel cell," *Journal of Power Sources*, vol. 178, pp. 269-281, 2008.

[64]   M. A. R. Sadiq Al-Baghdadi, "A CFD study of hygro-thermal stresses distribution in PEM fuel cell during regular cell operation," *Renewable Energy*, vol. 34, pp. 674-682, 2009.

[65]   N. T. Dave, J. P. Meyers, and D. A. Niezelski, "PEM fuel cell stack assembly with isolated internal coolant manifold," in *U.S Patent 7067214 B2*. United States, Jun. 27, 2006.

[66]   W. Qian, D. P. Wilkinson, J. Shen, H. Wang, and J. Zhang, "Architecture for portable direct liquid fuel cells," *Journal of Power Sources*, vol. 154, pp. 202-213, 2006.

[67]   R. P. O'Hayre, *Fuel cell fundamentals*, 2 ed. Hoboken, N.J: Wiley, 2009.

[68]   I. S. Hussaini and C.-Y. Wang, "Visualization and quantification of cathode channel flooding in PEM fuel cells," *Journal of Power Sources*, vol. 187, pp. 444-451, 2009.

[69]   A. Bazylak, "Liquid water visualization in PEM fuel cells: A review," *International Journal of Hydrogen Energy*, vol. 34, pp. 3845-3857, 2009.

[70]   A. Z. Weber and J. Newman, "Transport in Polymer-Electrolyte Membranes," *Journal of The Electrochemical Society*, vol. 150, pp. A1008-A1015, 2003.

[71]   I. Nitta, O. Himanen, and M. Mikkola, "Contact resistance between gas diffusion layer and catalyst layer of PEM fuel cell," *Electrochemistry Communications*, vol. 10, pp. 47-51, 2008

[72]   R. Jaggì, "Deviations from Ohm's law in semiconductors," *Journal of Physics and Chemistry of Solids*, vol. 29, pp. 1699-1702, 1968.

[73]   P. F. van den Oosterkamp, "Critical issues in heat transfer for fuel cell systems," *Energy Conversion and Management*, vol. 47, pp. 3552-3561, 2006.

[74]   S. G. Kandlikar and Z. Lu, "Thermal management issues in a PEMFC stack - A brief review of current status," *Applied Thermal Engineering*, vol. 29, pp. 1276-1280, 2009.

[75]   S. Litster, J. G. Pharoah, G. McLean, and N. Djilali, "Computational analysis of heat and mass transfer in a micro-structured PEMFC cathode," *Journal of Power Sources*, vol. 156, pp. 334-344, 2006.

[76]   H. D. Baehr and S. Kabelac, *Thermodynamik Grundlagen und technische Anwendungen*, Berlin: Springer, 2006.

[77]   R. A. Costa and J. R. Camacho, "The dynamic and steady state behavior of a PEM fuel cell as an electric energy source," *Journal of Power Sources*, vol. 161, pp. 1176-1182, 2006.

[78]   R.K. Shah, "Heat Exchangers for Fuel Cell Systems", The 4th International conference on Compact Heat Exchangers and Enhancement Technology for the Process Industries, Crete Island, Greece, 2003.

[79]   C.-Y. Wen and G.-W. Huang, "Application of a thermally conductive pyrolytic graphite sheet to thermal management of a PEM fuel cell," *Journal of Power Sources*, vol. 178, pp. 132-140, 2008.

[80]   C.-Y. Wen, Y.-S. Lin, and C.-H. Lu, "Performance of a proton exchange membrane fuel cell stack with thermally conductive pyrolytic graphite sheets for thermal management," *Journal of Power Sources*, vol. 189, pp. 1100-1105, 2009.

[81]   A. Faghri and Z. Guo, "Challenges and opportunities of thermal management issues related to fuel cell technology and modeling," *International Journal of Heat and Mass Transfer*, vol. 48, pp. 3891-3920, 2005.

[82]   M. Reichler, *Theoretische Untersuchungen zur Kühlleistungssteigerung durch innovative Kühlsysteme für Brennstoffzellen- Elektrofahrzeuge*, Dissertation/PhD-thesis, Universität Stuttgart, 2009.

[83]   D. K. Kondepudi and I. Prigogine, *Modern thermodynamics: from heat engines to dissipative structures*. New York: John Wiley & Sons, 1998

[84]   S. B. Pope, *Turbulent flows*. Cambridge: Cambridge Univ. Press, 2000.

[85]   A. Faghri and Z. Guo, "Integration of Heat Pipe into Fuel Cell Technology," *Heat Transfer Engineering*, vol. 29, pp. 232-238, 2008.

Curriculum Vitae

Syed Mushahid Hussain Hashmi, born 31-10-1972 in Karachi (Pakistan)

Education

2006 – 2010	Doctorate (Dr.-Ing), Helmut-Schmidt-Universität/Universität der Bundeswehr Hamburg
1999 – 2001	M.Sc in Mechanical Engineering (Energy Systems), NED University of Enginnering & Technology, Karachi
1992 – 1996	B.E in Mechanical Engineering, NED University of Engineering & Technology, Karachi
1989 – 1991	Intermediate in Pre-Engineering Government Islamia Science College, Karachi
– 1988	Matriculation in Science, Shah Abdul Latif Secondary School, Karachi

Work Experience

2003 – date	Assistant Professor- Department of Mechanical Engineering, NED University of Enginnering & Technology, Karachi
2002 – 2003	Laboratory Engineer- Department of Mechanical Engineering, NED University of Engineering & Technology, Karachi
1997 – 1999	Quality Assurance Engineer- Trans Mobile Ltd Bin Qasim Karachi, Pakistan

Hamburg, March 2010